Nonlinear optical processes in resonant GaAs-based nanoantennas.

MARIA DEL ROCIO CAMACHO MORALES

PhD

A thesis submitted for the degree of
Doctor of Philosophy

The Australian National University

16 December 2020

Acknowledgements

Several years ago, I arrived to Australia for the first time to pursue my PhD. Looking back at those days, I recognise I have grown a lot professionally and also personally. I have been blessed to be surrounded by people that helped me to cross this path, acquiring the skills I will need for my next journey. To all of them I am truly grateful.

First, I would like to thank my supervisor Dragomir Neshev. I am very grateful to him for his support and trust, from the very beginning when I applied to ANU until the end of my PhD, and even more. He was always positive with the outcomes of my work, encouraging and guiding me to continue moving forward in my research. Also, I would like to thank Mohsen Rahmani for helping and supporting me to complete my PhD projects. I would like to thank him for encouraging me to work hard and achieve things I did not know I was capable of. To Lei Xu, I would like to thank for all the discussions we had and for all the advice received. I always felt free to go and knock at his door to start a discussion and ask him any question. I would like to thank Lei for all his time and patience. To Dragomir, Mohsen and Lei, my sincere gratitude for being part of my supervisory panel.

I would like to thank all former and current members and visitors of the Nonlinear Physics Centre. Thank you for the moments we shared together, from Christmas's parties and evenings at Fellows Bar to discussions during lunch time. To all of those who shared the laboratory with me while I was performing experiments with the lights off, thank you for your patience and understanding. To all the students that joined the student chapter, thank you for your efforts and time to organise events. To Katie and James, the first members of the department I met, thank you for your welcome and more important for helping me in my transition to Australia. Special thanks to Kathy Hicks for helping me to complete all administrative processes and for running smoothly the department.

I would like to thank the Mexican government for their financial support through the scholarship granted by the Consejo Nacional de Ciencia y Tecnologia (CONACyT) and

to the Nonlinear Physics Centre for their supplementary scholarship granted through the Postgraduate Research Scholarship. Also I would like to thank the Centre for Ultrahigh bandwidth Devices for Optical Systems (CUDOS) for their financial support and professional development resources.

I would like to thank Dipankar, Bhavya, Inseok, Naiyin, Bijun and Yoghwan for all the celebrations and dinners we spent together. Thank you for all your wise recommendations of dishes and drinks! for the games we played together and for all those activities we did together to disconnect from our research. To Bruma and Pablo, my compatriot fellows, thank you for keeping me connected with my roots. My biggest gratitude to Rowena for all her support and help through all my PhD, I always counted on her in any circumstance. Thank your for all you encouragement and for continuously listening my struggles, this has always strengthened me.

Last but not least, I would like to thank my parents Jose Antonio y Patricia for their understanding, support through all my education, and everything they have done for me, my gratitude to them is beyond words. To my sisters, Monica and Carolina, thank you for your excitement and support in my research, even when your interests and passions are very different from mine. Thank you family, without you I would not be here. Thank you also for enduring difficult times while I am away and also for sharing with me all your happy moments. Family, you have been always here with me.

List of publications

Peer-Reviewed articles

Articles containing results included in this thesis are in bold.

(1) R. Camacho-Morales, D. Rocco, L. Xu, M. Rahmani, V. F. Gili, A. Komar, N. Dimitrov, L. Stoyanov, M. Lysevych, F. Karouta, A. Dreischuh, H. H.Tan, G. Leo, C. De Angelis, C. Jagadish, A. E. Miroshnichenko, and D. N. Neshev, **"Infrared imaging in nonlinear (110)-GaAs metasurfaces"**, *In preparation*.

(2) L. Xu, G. Saerens, M. Timofeeva, D. A. Smirnova, I. Volkovskaya, M. Lysevych, R. Camacho-Morales, M. Cai, K. Zangeneh Kamali, L. Huang, F. Karouta, H. H. Tan, C. Jagadish, A. E. Miroshnichenko, R. Grange, D. N. Neshev, and M. Rahmani, **"Forward and Backward Switching of Nonlinear Unidirectional Emission from GaAs Nanoantennas"**, *ACS Nano*. vol. 14, no. 2, pp. 1379-1389, 2020.

(3) J. D. Sautter, L. Xu, A.E. Miroshnichenko, M. Lysevych, I. Volkovskaya, D. A. Smirnova, R. Camacho-Morales, K. Zangeneh Kamali, F. Karouta, K. Vora, H. H. Tan, M. Kauranen, I. Staude, C. Jagadish, D. N. Neshev, and M. Rahmani, **"Tailoring Second-Harmonic Emission from (111)-GaAs Nanoantennas"**, *Nano Letters*, vol. 19, no. 6, pp. 3905-3911, 2019.

(4) L. Xu, K. Zangeneh Kamali, L. Huang, M. Rahmani, A. Smirnov, R. Camacho-Morales, Y. Ma, G. Zhang, M. Woolley, D. N. Neshev, A. E. Miroshnichenko, "Dynamic Nonlinear Image Tuning through Magnetic Dipole Quasi-BIC Ultrathin Resonators", *Advanced Science*, vol. 6, no. 15, p. 1802119, 2019.

(5) R. Camacho-Morales, G. Bautista, X. Zang, L. Xu, L. Turquet, A. Miroshnichenko, H. H. Tan, A. Lamprianidis, M. Rahmani, C. Jagadish, D. N. Neshev, and M. Kauranen, **"Resonant harmonic generation in individual AlGaAs nanoantennas probed by cylindrical vector beams"**, *Nanoscale*, vol. 11, pp. 1745-1753, 2019.

(6) L. Xu , M. Rahmani, K. Zangeneh Kamali, A. Lamprianidis, L. Ghirardini, J. Sautter, R. Camacho-Morales, H. Chen, M. Parry, I. Staude, G. Zhang, D. N. Neshev and A. E. Miroshnichenko, "Boosting third-harmonic generation by a mirror-enhanced anapole resonator", *Light: Science & Applications*, vol. 7, no. 44, pp. 1-8, 2018.

(7) E. V. Melik-Gaykazyan, S. Kruk, R. Camacho-Morales, L. Xu, M. Rahmani, K. Zangeneh Kamali, A. Lamprianidis, A. E. Miroshnichenko, A. A. Fedyanin, D. N. Neshev, and Y. S. Kivshar, "Selective Third Harmonic Generation by Structured Light in Mie-Resonant Nanoparticles", *ACS Photonics*, vol. 5, no. 3, pp. 728-733, 2018.

(8) M. Rahmani, L. Xu, A. E. Miroshnichenko, A. Komar, R. Camacho-Morales, H. Chen, Y. Zárate, S. Kruk, G. Zhang, D. N. Neshev and Y. S. Kivshar, "Reversible Thermal Tunning of All-Dielectric Metasurfaces", *Advanced Functional Materials*, vol. 27, no. 31, p. 1700580, 2017.

(9) S. Kruk, R. Camacho-Morales, L. Xu, M. Rahmani, D. A. Smirnova, L. Wang, H. H. Tan, C. Jagadish, D. N. Neshev, and Y. S. Kivshar. **"Nonlinear Optical Magnetism revealed by Second-Harmonic generation in Nanoantennas"**, *Nano Letters*, vol. 17, no. 6, pp. 3914-3918, 2017.

(10) M. Rahmani, A. S. Shorokhov, B. Hopkins, A. E. Miroshnichenko, M. R. Shcherbakov, R. Camacho-Morales, A. A. Fedyanin, D. N. Neshev, and Y. S. Kivshar. "Nonlinear Symmetry Breaking in Symmetric Oligomers", *ACS Photonics*, vol. 4, no. 3, pp. 454-461, 2017.

(11) R. Camacho-Morales, M. Rahmani, S. Kruk, L. Wang, L. Xu, D. A. Smirnova, A. S. Solntsev, A. E. Miroshnichenko, H. H. Tan, F. Karouta, S. Naureen, K. Vora, L. Carletti, C. De Angelis, C. Jagadish, Y. S. Kivshar, and D. N. Neshev, **"Nonlinear Generation of Vector Beams from AlGaAs nanoantennas"**, *Nano Letters*, vol. 16, no. 11, pp. 7191-7197, 2016.

Selected conference presentations and proceedings.

(1) R. Camacho-Morales, D. Rocco, Lei Xu, M. Rahmani, V. F. Gili, A. Komar, N. Dimitrov, L. Stoyanov, M. Lysevych, F. Karouta, A. Dreischuh, H. H. Tan, G. Leo, C. De Angelis, C. Jagadish, A. E. Miroshnichenko, and D. N. Neshev, "Infrared imaging in nonlinear GaAs metasurfaces", SPIE Micro+Nano Materials, Devices and Applications 2019 (Mellbourne, Australia).

(2) R. Camacho-Morales, G. Bautista, X. Zang, L. Xu, L. Turquet, A. E. Miroshnichenko, H. H. Tan, A. Lamprianidis, M. Rahmani, C. Jagadish, D. N. Neshev, and M. Kauranen, "Resonant harmonic generation in AlGaAs nanoantennas using structured light", Advanced Photonics 2018 (Zurich, Switzerland).

(3) R. Camacho-Morales, M. Rahmani, S. Kruk, L. Wang, L. Xu, D. A. Smirnova, A. S. Solntsev, A. E. Miroshnichenko, H. H. Tan, F. Karouta, S. Naureen, K. D. Vora, L. Carletti, C. De Angelis, C. Jagadish, Y. S. Kivshar, and D. N. Neshev, "Directional second harmonic generation from AlGaAs nanoantennas", SPIE Nanoscience + Engineering 2017 (California, United States of America).

(4) R. Camacho-Morales, M. Rahmani, S. Kruk, L. Wang, L. Xu, D. A. Smirnova, A. S. Solntsev, A. E. Miroshnichenko, H. H. Tan, F. Karouta, S. Naureen, K. D. Vora, L. Carletti, C. De Angelis, C. Jagadish, Y. S. Kivshar, and D. N. Neshev, "Highly directional second-harmonic generation from AlGaAs nanoparticles", SPIE Optics + Optoelectronics 2017 (Prague, Czech Republic).

Abstract

This PhD dissertation presents a systematic study in the linear and nonlinear optical properties of all-dielectric systems grounded on GaAs-based nanoantennas. First, I introduce a new nonlinear microscopy technique that determines the crystalline orientation of individual (100)-AlGaAs nanoantennas. The nonlinear microscopy technique, based in a point-scanning nonlinear microscope and structured light incidence, retrieves nonlinear intensity patterns which describe the crystalline orientation of the nanoantennas through the polarisation-dependency of the nonlinear process. The study of the nonlinear intensity maps indicate the transverse electric field components play a main role in the generation of harmonics. Also, the use of this nonlinear microscopy technique proved the generation of resonantly enhanced harmonic processes, driven by the presence of anapole-assisted modes.

Considering the main role of transverse electric field components in the harmonic generation of (100)-AlGaAs nanoantennas, a linearly polarised beam was used to study the properties of second-harmonic generation. A conversion efficiency of the order of 10^{-4} was demonstrated using (100)-AlGaAs nanoantennas, together with the generation of nonlinear nanoscale light sources emitting vector beams. In addition, continuous control in the transition between electric and magnetic second-harmonic generation was demonstrated. In all the studies using (100)-AlGaAs nanoantennas, zero normal second-harmonic generation was observed due to the symmetry of the second order nonlinear tensor.

Normal second-harmonic generation can be attained when the symmetry of the system is reduced. This can be realised by extrinsic changes such as the design of asymmetric nanoantennas or the use of non-normal incidence. Another approach is to perform intrinsic changes such as changing the orientation of the nonlinear tensor through the fabrication of GaAs nanoantennas along different crystalline axis. Using this last approach, normal second-harmonic generation was realised as well as engineered second-harmonic emission from GaAs

nanoantennas. Under the simple case of normal incidence, polarisation-independent conversion efficiencies and normal second-harmonic generation were demonstrated in (111)-GaAs nanoantennas. In addition to normal second-harmonic generation, control over the forward and backward second-harmonic emission was demonstrated in (110)-GaAs nanoantennas, including the case of nonlinear unidirectional emission.

While the previous studies were dedicated to the fundamentals of second-harmonic generation in GaAs-based nanoantennas, in the last part of this thesis I discuss the potential applications of GaAs metasurfaces to perform infrared up-conversion. Attractive nonlinear properties from (110)-GaAs metasurfaces are anticipated, due to the observed capabilities of (110)-GaAs nanoantennas.Enhancement of second-harmonic generation and sum-frequency generation was demonstrated in GaAs metasurfaces, through the excitation of electric and magnetic modes at the incident wavelengths. More interestingly, up-conversion of an invisible infrared image to the visible spectrum was demonstrated using (110)-GaAs metasurfaces, via sum-frequency generation. The sum-frequency generation process, originated in the metasurface, enabled the realisation of visible images which can be resolved in the femtosecond regime and can be detected by a conventional CCD camera.

Contents

List of Figures

CHAPTER 1

Introduction

1.1 Motivation

Antennas are key elements of wireless communication, enabling the manipulation and concentration of electromagnetic fields to realise efficient interfaces between propagating radiation and localised fields. In the radiowave and microwave frequency regime, antennas allowed the development of modern technologies which are employed in satellite communications, cellular phones and televisions. The importance and utility of radio and microwave antennas promoted the translation of this concept into the optical frequency regime, where propagating visible and infrared fields can be redirected and transferred into localised sources. Since antennas have comparable dimensions to their operating wavelength, nanometric structures are required to realise optical antennas also known as nanoantennas. The study of nanoantennas has become a growing field of research, facilitated by the significant advancements in nanofabrication technologies and promoted by their potential application in novel optoelectronic devices, infrared and multi-spectral imaging, near-field optics and sensing, among many others. In nanoantennas, the optical fields are controlled by the excitation of resonances first described by the theory of Mie (*1*).

Beyond the ability to mediate the interaction between localised and propagating fields, nanoatennas have also exhibited nonlinear optical effects due to the strong confinement of the optical fields at their resonant frequencies. The applications of nonlinear optical phenomena vary from light sources to signal processing, optical communications, spectroscopy, and plasma physics, to name a few. By employing the nonlinear optical properties of materials, nanoantennas provide a unique platform to realise many of these applications at the nanometric

scale, since they are capable to generate light at new frequencies and control photon-photon interactions. Much of the focus in the study of nonlinear nanoantennas has centred in the use of plasmonic and dielectric centrosymmetric materials, hindering the observation of second-order nonlinear processes and therefore limiting the conversion efficiency of nonlinear processes. GaAs is a non-centrosymmetric material able to produce second-order nonlinear processes, which in general have higher conversion efficiencies. In this thesis, I present the study and control of new frequencies generated in GaAs-based nanoantennas, using nonlinear processes. Different strategies were explored to control the properties of the new frequencies generated, leading to demonstrate the potential applications of GaAs nanoantennas arrays to perform infrared imaging in a nanoscale platform.

1.2 Thesis outline

This thesis is composed by seven chapters. The first chapter contains the theoretical background and overview of the topic, introducing the concepts relevant to this thesis. Chapter 2 summarizes the optical properties of GaAs and presents the progress in the study of GaAs nanoantennas. Chapter 2 is followed by four chapters containing the main results obtained during my PhD. The seventh and last chapter contains the conclusions of this thesis, together with an outlook of possible realisations.

In Chapter 3, I present my studies in the SHG and THG of individual (100)-AlGaAs nanoantennas by using a cylindrical vector beam excitation. The advantages in the use of scanning cylindrical vector beams to study the crystalline orientation of AlGaAs nanoantennas are demonstrated. Also, the enhancement of the SHG and THG is explained by the excitation of anapole-assisted states driven by cylindrical vector beam excitation. This chapter demonstrates control over the intensity of the nonlinear emissions.

In Chapter 4, I present my studies on the SHG efficiency, polarisation state and radiation pattern of individual (100)-AlGaAs nanoantennas, both in the backward and forward directions. These studies were possible due to the new fabrication platform developed, which allows the transfer of AlGaAs nanoantennas to a transparent substrate. The generation of nonlinear

vector beams by AlGaAs nanoantennas was demonstrated. Additionally, experimental distinction between electric and magnetic second-harmonic modes was demonstrated. This chapter demonstrates control over the polarisation of the nonlinear emission, but limited control in their directionality.

In Chapter 5, I present the SHG intensity and radiation pattern of individual (111)- and (110)-GaAs nanoantennas. The possibility to control the SHG directionality was demonstrated by changing the radius of the nanoantennas and the polarisation angle of the incident beam. A comparison of the SHG from differently orientated GaAs nanoantennas was performed, showing the unique capabilities of (110)-GaAs nanoantennas to control the nonlinear emission at the nanoscale.

The control in the intensity, polarisation and directionality of the nonlinear emission demonstrated in the previous chapters allowed me to explore the possible applications of GaAs naonoantenna arrays, also known as metasurfaces, for infrared imaging. In Chapter 6, resonant (110)-GaAs metasurfaces were designed to enhance the conversion efficiency of a second-order nonlinear process: sum-frequency generation. This nonlinear optical process up-converts the infrared incident beam to the visible spectrum. More interestingly, up-conversion of an invisible infrared image to the visible was demonstrated using the resonant GaAs metasurfaces. The experiments performed show the potential applications of GaAs metasurfaces for night-vision, infrared bioimaging and sensor devices.

1.3 Theoretical background

In this section I will briefly present the theoretical concepts used in the study of optical processes in the medium, with an emphasis in light-matter interactions in small particles. These concepts form the basis of the results presented in this thesis.

1.3.1 Linear optical response of materials

The interaction of an electromagnetic field with matter is fully described by Maxwell's equations

$$\begin{aligned} \nabla \cdot \boldsymbol{E}(\boldsymbol{r},t) &= 4\pi\rho(\boldsymbol{r},t), \\ \nabla \times \boldsymbol{B}(\boldsymbol{r},t) - \frac{1}{c}\frac{\partial \boldsymbol{E}(\boldsymbol{r},t)}{\partial t} &= \frac{4\pi}{c}\boldsymbol{J}(\boldsymbol{r},t), \\ \nabla \times \boldsymbol{E}(\boldsymbol{r},t) + \frac{1}{c}\frac{\partial \boldsymbol{B}(\boldsymbol{r},t)}{\partial t} &= 0, \\ \nabla \cdot \boldsymbol{B}(\boldsymbol{r},t) &= 0. \end{aligned} \tag{1.1}$$

$\boldsymbol{E}$ and $\boldsymbol{B}$ are the electric field and the magnetic induction, respectively; c is the velocity of the light in free space. The electric current density is denoted as $\boldsymbol{J}$ and the electric charge density as ρ. All quantities are spatially, $\boldsymbol{r}$, and temporally, t, dependent as indicated by $(\boldsymbol{r},t)$. The generalized Ampere's equation can be rewritten as:

$$\nabla \times \boldsymbol{B}(\boldsymbol{r},t) = \frac{4\pi}{c}\Big(\boldsymbol{J}(\boldsymbol{r},t) + \boldsymbol{J}_d(\boldsymbol{r},t)\Big), \tag{1.2}$$

where

$$\boldsymbol{J}_d(\boldsymbol{r},t) = \frac{1}{4\pi}\frac{\partial \boldsymbol{E}(\boldsymbol{r},t)}{\partial t} \tag{1.3}$$

is known as the *displacement current* or more correctly, the *displacement current density*. The displacement current is not a "real" current in the conventional sense, since an electric current is defined as the physical movement of a charge. While the displacement current density does not describe charges flowing through some region, it can generate a magnetic field just like a real current does. The change of the electric field rate due to the displacement current produces a changing magnetic field even when there are no charges present and no physical current flows. Through this mechanism, electromagnetic waves may propagate through vacuum, as changing magnetic fields induce electric fields and vice versa changing electric fields induce magnetic fields.

In free-space there are no free charges and currents, so that $\boldsymbol{J} = 0$ and $\rho = 0$. Thus, by combining Equations 1.1 and the well-known vector identity $\nabla\times(\nabla\times\boldsymbol{E}) = \nabla(\nabla\cdot\boldsymbol{E}) - \nabla^2\boldsymbol{E}$),

we obtain the wave propagation equation of the electric field:

$$\nabla^2 \boldsymbol{E} - \frac{1}{c^2}\frac{\partial^2 \boldsymbol{E}}{\partial t^2} = 0. \tag{1.4}$$

A similar procedure can be followed to obtain the corresponding wave equation of the magnetic induction field:

$$\nabla^2 \boldsymbol{B} - \frac{1}{c^2}\frac{\partial^2 \boldsymbol{B}}{\partial t^2} = 0. \tag{1.5}$$

The wave equations of the electric (see Equation 1.4) and magnetic field (see Equation 1.5) describe the propagation of an electromagnetic field in free-space, with a phase velocity $c = (\epsilon_0 \mu_0)^{-1/2}$. The constants ϵ_0 and μ_0 are the permittivity and permeability of the vacuum, respectively. Therefore, Maxwell's equations (see Equations 1.1) describe the electric and induction fields in the space, when all the sources ρ and $\boldsymbol{J}$ are specified. In the presence of matter, an electromagnetic field may lead to electric dipoles, magnetic moments, polarised charges and induced currents. The electric displacement $\boldsymbol{D}$ associated to the electric field $\boldsymbol{E}$, and the magnetic induction $\boldsymbol{B}$ associated with the magnetic field $\boldsymbol{H}$, are introduced in the Maxwell's equations to take into account the modifications of the fields induced by the medium. In the presence of matter, Maxwell's equations are expressed as:

$$\begin{aligned} \nabla \cdot \boldsymbol{D}(\boldsymbol{r}, t) &= 4\pi\rho(\boldsymbol{r}, t), \\ \nabla \times \boldsymbol{H}(\boldsymbol{r}, t) - \frac{1}{c}\frac{\partial \boldsymbol{D}(\boldsymbol{r}.t)}{\partial t} &= \frac{4\pi}{c}\boldsymbol{J}(\boldsymbol{r}, t), \\ \nabla \times \boldsymbol{E}(\boldsymbol{r}, t) + \frac{1}{c}\frac{\partial \boldsymbol{B}(\boldsymbol{r}.t)}{\partial t} &= 0, \\ \nabla \cdot \boldsymbol{B}(\boldsymbol{r}, t) &= 0, \end{aligned} \tag{1.6}$$

where the displacement $\boldsymbol{D}$ and magnetic $\boldsymbol{H}$ fields are defined defined as:

$$\boldsymbol{D} = \boldsymbol{E} + 4\pi\boldsymbol{P}, \tag{1.7}$$

$$\boldsymbol{H} = \boldsymbol{B} - 4\pi\boldsymbol{M}. \tag{1.8}$$

The new fields $\boldsymbol{P}$ and $\boldsymbol{M}$ are the induced polarisation and the magnetisation of the material, respectively. The origin of these new fields will be explained below by observing the new contributions arising from the material; the charge density ρ and the current density $\boldsymbol{J}$. Within the matter, the total charge density $\rho = \rho_{total}$ now consists of two components, free and bound

charge densities:

$$\rho_{total} = \rho_{free} + \rho_{bound}. \tag{1.9}$$

If we consider the propagation of electromagnetic waves through an electrically neutral material, where $\rho_{free} = 0$, the total charge density is non-zero since there is a contribution from the bound charges. When an electric field is applied, the displacement of the material's positive and negative charges induces the polarisation $\boldsymbol{P}$ of the medium. The polarisation $\boldsymbol{P}$ can vary in space, leading to local concentrations of positive or negative charges. The spatially variant polarisation creates a charge density:

$$\rho_{bound} = -\nabla \cdot \boldsymbol{P}. \tag{1.10}$$

Bound electric charges act as the source of additional electric fields within the material.

On the other hand, assuming there is no external current $\boldsymbol{J}_{ext} = 0$, the total current has three contributions that account for the response of a medium, according to:

$$\boldsymbol{J}_{total} = \boldsymbol{J}_{cond} + \boldsymbol{J}_p + \boldsymbol{J}_{bound}. \tag{1.11}$$

Current can arise from free charges in motion such as electrons in a metal. According to Ohm's law this current can be expressed in terms of the conductivity σ of the material:

$$\boldsymbol{J}_{cond} = \sigma \boldsymbol{E}. \tag{1.12}$$

Another contribution to the current density within the matter comes from the time rate of the polarisation. Physically, if the dipoles inside the medium change their strength or orientation as a function of time, an effective current density arises in the medium. The polarisation current density is then given by:

$$\boldsymbol{J}_p = \frac{\partial \boldsymbol{P}}{\partial t}. \tag{1.13}$$

Finally, just as bound electric charges act as the source of additional electric fields within the material, bound currents may act as the source of additional magnetic fields, according to:

$$\boldsymbol{J}_{bound} = c\boldsymbol{\nabla} \times \boldsymbol{M}, \tag{1.14}$$

where $\boldsymbol{J}_{bound}$ is the bound current density and $\boldsymbol{M}$ represents the magnetisation of the material.

The electric field $\boldsymbol{E}$ and the electric displacement $\boldsymbol{D}$ are related to each other by a proportionality constant, called the dielectric constant or permittivity ϵ of the material:

$$\begin{aligned} \boldsymbol{D} &= \boldsymbol{E} + 4\pi\boldsymbol{P}, \\ &= \epsilon\boldsymbol{E}. \end{aligned} \tag{1.15}$$

As shown in the above equation, the permittivity ϵ determines the response of the material to an applied electric field. In an insulator or dielectric material charges do not move freely, but may be slightly displaced from their equilibrium position. The displacement of bound charges against restoring forces in a dielectric material creates internal dipole moments, which give rise to additional lines of electric induction. The sum of the internal dipole moments induced per unit volume is equal to the polarisation density $\boldsymbol{P}$.

Similarly, the magnetic field $\boldsymbol{H}$ and the magnetic induction $\boldsymbol{B}$ are related to each other by a proportionality constant called the permeability μ of the material:

$$\begin{aligned} \boldsymbol{B} &= \boldsymbol{H} + 4\pi\boldsymbol{M}, \\ &= \mu\boldsymbol{H}. \end{aligned} \tag{1.16}$$

The permeability μ determines the response of a material to an applied magnetic field. Equations 1.12, 1.15 and 1.16 are known as the constitutive relations.

In the optical frequency range and in a non-ferromagnetic material, the magnetisation phenomenon is very weak and $\boldsymbol{M}$ is considered equal to zero. On the other hand, electrons respond readily to optical frequency fields; either the permittivity ϵ or the conductivity σ, and occasionally both, have values distinctively different from the vacuum case. In conductors, the otherwise free motion of the unbounded electrons is interrupted by collisions, which randomise the collective motion, converting its energy to heat. This provides an absorption mechanism and small resistance to the motion of the charges due to the high values of σ in conductors materials. Dielectrics, on the other hand, are characterised by a lack of free electrons, very low conductivities and optical transparency. In dielectrics, the bounded electrons can execute forced oscillations upon the excitation of an electromagnetic field, leading to displacement currents rather than conduction currents. The displacement currents may be

also damped by dissipative processes, in which case the displacement polarisation lags behind the driving field in term of its phase.

1.3.2 Nonlinear optical response of materials

Ordinary light consists of uncorrelated contributions from a vast number of independently radiating atomic systems where phase relationships do not persist, thus generating an incoherent light source. Laser radiation, on the other hand, is highly coherent enabling to obtain extremely intense local radiation fields in small volumes by focusing a laser beam onto a small area. The field of nonlinear optics began with the first observation of second-harmonic generation (SHG) by Franken *et al.* in 1961, shortly after the development of the first laser done by Maiman in 1960.

When an electric field is applied to a medium, the electrons of the medium are being polarised by the field. For weak electric fields, the resulting polarisation is proportional to the applied field according to

$$\boldsymbol{P} = \chi^{(1)}\boldsymbol{E}, \tag{1.17}$$

where $\chi^{(1)}$ is the linear electric susceptibility of the material. In a crystalline medium, the linear susceptibility is a tensor that obeys the symmetry properties of the crystal. The linear susceptibility is related to the refractive index of the medium *n* according to $\chi^{(1)} = n^2 - 1$.

With the advent of lasers, stronger electric fields had been made available which excite nonlinear optical effects in materials. In such case and to a good approximation, the polarisation is given by a Taylor series of the total electric field whose coefficients are the nonlinear susceptibilities:

$$\boldsymbol{P} = \chi^{(1)}\boldsymbol{E} + \chi^{(2)}\boldsymbol{EE} + \chi^{(3)}\boldsymbol{EEE} + ... \tag{1.18}$$

The quantities $\chi^{(2)}$ and $\chi^{(3)}$ are known as the second- third-order nonlinear susceptibilities, respectively. For moderate light intensities, the material responds linearly to the applied field, as described earlier in Section 1.3.1. The linear response of the material to the incident light describes several conventional optical effects including refraction, absorption and scattering, where only the first term of the Equation 1.18 is considered. Optical nonlinearities are

manifested by the change in the optical properties of the medium as the intensity of the incident electromagnetic field is increased which induces asymmetric electronic bindings and distortion in the bound electron orbits of the material. In such case, higher-order terms of the polarisation density (see Equation 1.18) related to $\chi^{(2)}$ and $\chi^{(3)}$ are considered in the description of the material response. When these higher-order terms are included, the polarisation $\boldsymbol{P}$ acts as a source of new field components, sums and differences of the incident light frequencies described by optical parametric nonlinear processes. Parametric nonlinear processes, often represented in terms of photon diagrams, conserve the energy and momentum of the incident light. In the case of second order nonlinear processes, new frequencies are generated through processes such as SHG and sum-frequency generation (SFG), as illustrated in the diagram levels of Figure 1.1a. The second order nonlinear susceptibility displays the symmetry of the crystalline medium, in a similarly way as the linear susceptibility does. As a consequence, in centrosymmetric media and under the electric-dipole approximation, second- and all even-order nonlinear susceptibilities become zero due to the inversion symmetry of the media. Under this approximation, centrosymmetric materials can generate new frequencies through third order nonlinearities such as third harmonic generation (THG) and four-wave mixing (FWM), as illustrated in the diagram levels of Figure 1.1b. Outside the electric-dipole approximation, the bulk nonlinear polarisation has other contributions due to the magnetic-dipole, the electric-quadrupole and other interactions observed at the microscopic level. To account for such multipolar effects, the effective light–matter interaction Hamiltonian is presented in the form

$$H_{int} = -\boldsymbol{p} \cdot \boldsymbol{E} - m \cdot \boldsymbol{B} - [\boldsymbol{Q}\nabla] \cdot \boldsymbol{E} - ..., \tag{1.19}$$

where $\boldsymbol{E}$ is a local electric field, $\boldsymbol{p}$ is the electric-dipole moment, $\boldsymbol{m}$ is the magnetic-dipole moment, and $\boldsymbol{Q}$ is the electric-quadrupole moment (*2*).

1.3.3 Scattering of small particles

The study of scattering particles is applicable to a variety of research fields, from chemistry (*3*) and medicine (*4*) to oceanography (*5*) and astronomy (*6*), to name a few. In many of

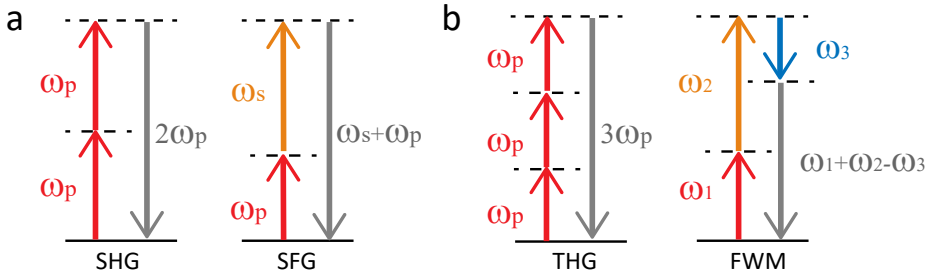

FIGURE 1.1: Photon diagram levels of parametric nonlinear optical processes of (a) second- and (b) third-order. The second-order processes represented here are second-harmonic generation (SHG) and sum-frequency generation (SFG). The third-order processes represented here are third-harmonic generation (THG) and four-wave mixing (FWM). The solid horizontal lines correspond to real states of the material, whereas the dashed lines represent what are known as virtual levels. The coloured arrows correspond to the frequencies of the incident fields, driving the generation of new fields with lower or higher frequencies. The new frequencies generated by second- and third-order nonlinear processes are represented by gray arrows.

these fields, the scattering of the light is the easiest means to detect small particles and an obvious means to further investigate the properties of such particles including its composition, concentration, size, shape and orientation.

A parallel monochromatic beam propagates in vacuum without changing its direction, frequency, intensity and polarisation state. However, interposing a small particle into the beam causes several physical effects like scattering and diffraction. Scattering is the phenomenon in which the incident radiation changes its direction and possibly its frequency after interacting with molecules or particles; the scattering field accounts for the electromagnetic waves reirradiated by the molecule or particle. The scattering is considered elastic when the frequency of the scattering light is unchanged with respect to the incident one and inelastic when the frequency changes in the process. Major forms of elastic light scattering are Rayleigh and Mie scattering. Inelastic scattering includes Brillouin, Raman, inelastic X-ray and Compton scattering. If the intensity of the beam is very high, several nonlinear phenomena can occur as the light interacts with the particles of the medium; these phenomena are described by nonlinear optics as previously discussed in Section 1.3.2.

The processes of elastic scattering can be understood as follows. A beam of light is an oscillating electromagnetic wave, whereas the particle is an aggregation of large number of discrete elementary electric charges. The incident electromagnetic field excites the elementary charges of the particle to oscillate with the same frequency by creating polarisation and conduction currents inside the medium. Thereby, secondary electromagnetic waves are radiated in all directions, the superposition of these secondary waves gives the total elastic scattered field (*7*). Electromagnetic scattering is a complex phenomenon because the secondary waves generated by each oscillating charge can also stimulate the oscillation of all other charges conforming the particle. The reflection and refraction of light constitute a specific case of the elastic scattering. In addition to re-radiating electromagnetic energy, the excited elementary charges may transform part of the incident energy into other forms, *e.g.* thermal energy via absorption. The absorption causes dissipation of energy from the electromagnetic wave into the medium. Both scattering and absorption remove energy from an electromagnetic wave, thus attenuating the beam. This attenuation, more often called extinction, is observed when we look at the light source through the particles, therefore it is the combined effect of scattering and absorption:

Extinction = Scattering + Absorption.

The size of a scattering particle can be represented by a non-dimensional size parameter x:

$$x = kr = \frac{2\pi rn}{\lambda}, \tag{1.20}$$

where k is the propagation constant of the medium, r is the radius of the particle, $2\pi r$ is the circumference of the particle, n is the refractive index of the medium and λ is the wavelength of incident wave. Based on the value of x, three main scattering regimes exist (*8*):

$x \ll 1$: Rayleigh scattering (small particle compared to wavelength of light);
$x \approx 1$: Mie scattering (the size of the particle is comparable to the wavelength of light);
$x \gg 1$: Geometric scattering (particle much larger than the wavelength of light).

The first mathematically rigorous attempts to quantify the scattering behaviour of small particles were derived by Lord Rayleigh for the case of a very small scatterer (electrostatic case). Rayleigh clarified why our sky is blue by studying the atmosphere molecules as scatters

particles. These interactions depend only on material properties, not on particle shape. Almost simultaneously, developments attributed to researches such as Thomson, Love, Lorenz, Debye, and Mie gave birth to a more complete electrodynamic perspective about this problem, always in accordance with Maxwell equations. Gustav Mie explained the colour variation in colloidal solutions of gold nanoparticles in terms of their size distribution. Mie-type resonances depend on both the material properties and the geometry of the particle in question. In the geometric scattering regime, ray tracing techniques are applied to study light scattering by spherical and non-spherical particles. In this thesis, I present the studies on the Mie scattering of nanoscale particles. The Mie theory is explained below.

1.3.3.1 Mie Scattering

The classical electromagnetic multipole expansion is a powerful tool used by Mie to analyse the optical fields scattered by small particles (*1*). The analytical solution of Maxwell's equations provided by Mie, describes the light-matter interaction of a plane wave exciting a homogeneous, isotropic and non-magnetic sphere embedded in a non-absorbing medium, in terms of an infinite series of spherical multipole coefficients. The development of the Mie theory starts from the homogeneous Helmholtz's equations of the electric field $\boldsymbol{E}$ and magnetic field $\boldsymbol{B}$:

$$\nabla^2 \boldsymbol{E} + k^2 \boldsymbol{E} = 0, \tag{1.21}$$

$$\nabla^2 \boldsymbol{H} + k^2 \boldsymbol{H} = 0. \tag{1.22}$$

Given the geometry of the problem, the incident plane wave described by Equations 1.21 and 1.22 is written as an infinite series of vector spherical harmonics. After applying Maxwell's equations to the boundaries of the spherical particle, the scattered and the internal fields of the sphere are obtained in terms of the incident field. The electric and magnetic components of the scattered field contain a set of undetermined complex amplitude coefficients, also called Mie coefficients. By solving the boundary conditions on the surface of the sphere, the Mie coefficients are determined. In the boundary conditions, continuity of all transverse field components is imposed at the interface between the sphere and the surrounding medium. The Mie coefficients contain well-behaved functions that vanish at infinity and converge at the

origin of the sphere. In this way, the scattered field of a single isolated sphere with a radius *r* and relative refractive index *m* can be decomposed into a multipole series term of scattered electric field proportional to (*9*):

$$a_i = \frac{m\Psi_i(mx)\Psi_i'(x) - \Psi_i(x)\Psi_i'(mx)}{m\Psi_i(mx)\xi_i'(x) - \xi_i(x)\Psi_i'(mx)}, \tag{1.23}$$

whereas the scattered magnetic field is proportional to:

$$b_i = \frac{\Psi_i(mx)\Psi_i'(x) - m\Psi_i(x)\Psi_i'(mx)}{\Psi_i(mx)\xi_i'(x) - m\xi_i(x)\Psi_i'(mx)}, \tag{1.24}$$

where m=n_1/n, n_1 and n being the refractive indices of the particle and the surrounding medium, respectively; x is the size parameter as defined earlier in Equation 1.20 and the functions Ψ_i and ξ_i are related to the Riccati-Bessel functions through:

$$\Psi_i(\rho) = \rho j_i(\rho), \tag{1.25}$$

$$\xi_i(\rho) = \rho h_i^{(1)}(\rho), \tag{1.26}$$

where $j_i(\rho)$ is the spherical Bessel function, and $h_i^{(1)}$ is the Hankel function of the first kind. The amplitude coefficients a_i and b_i are respectively related to the electric and magnetic optical response of a sphere, and depend on the size parameter x and the relative refractive index m. Each of these amplitudes has a set of resonant frequencies at which the electromagnetic field of the incident light is enhanced.

The scattering and absorption cross section is a quantity with dimensions of area related to the electromagnetic power scattered or absorbed by a single particle, respectively. Whereas the extinction cross section represents the overall amount of power subtracted from the incident wave, over the amount of power per unit area carried by the incident wave. The cross sections are defined in terms of the Mie coefficients according to:

$$C_{sca} = \frac{2\pi}{k^2}\sum_{i=1}^{\infty}(2i+1)(|a_i|^2 + |b_i|^2), \tag{1.27}$$

$$C_{ext} = \frac{2\pi}{k^2}\sum_{i=1}^{\infty}(2i+1)Re(|a_i|^2 + |b_i|^2), \tag{1.28}$$

$$C_{abs} = C_{ext} - C_{sca}. \tag{1.29}$$

The Mie coefficients can also describe the energy balance between the different mechanisms on a sphere: scattering and absorption. The scattering and absorption efficiencies are relevant to the far-field of a sphere and are expressed as a combination of the Mie coefficients according to:

$$Q_{sca} = \frac{2}{x^2}\sum_{i=1}^{\infty}(2i+1)(|a_i|^2 + |b_i|^2), \tag{1.30}$$

$$Q_{ext} = \frac{2}{x^2}\sum_{i=1}^{\infty}(2i+1)Re(|a_i|^2 + |b_i|^2), \tag{1.31}$$

$$Q_{abs} = Q_{ext} - Q_{sca}. \tag{1.32}$$

In the Mie theory, both metallic and dielectric spherical particles can possess a series of electromagnetic resonances identified by the observation of strongly enhanced scattering efficiencies. The difference between metallic and dielectric particles is the sign of the dielectric permittivity, which is negative for metals ($\epsilon < 0$) and positive for dielectric materials ($\epsilon > 0$). Figure 1.2a shows several peaks of scattering enhancement: the plasmonic resonances produced by metallic particles correspond to the red peaks while the resonances produced by dielectric particles correspond to the blue peaks. The electric dipole (ED) and magnetic dipole (MD) are associated to the coefficients a_1 and b_1, respectively; while the electric quadrupole (EQ) and magnetic quadrupole (MQ) are associated to the coefficients a_2 and b_2, respectively. In metallic spherical particles, the plasmonic resonances are associated to the enhancement of the electric Mie coefficients a_i, while resonances of a spherical dielectric particle exhibit the enhancement of both electric a_i and magnetic b_i coefficients. In metallic particles, the electric resonances are originated by the oscillation of polarisation charges excited by the incident light, which create charge distributions. In dielectric particles, the electric and magnetic resonances originate from the displacement current of bound electrons. The linear oscillation of the displacement currents within dielectrics particles builds their electric resonances. The magnetic resonances require field penetration and phase retardation of the field within the dielectric particle to create a circular current distribution, leading to a magnetic field. The contribution of third-order (a_3 and b_3 octupole modes), and higher-order modes to the total scattering is usually negligible. The field structures of the electric and magnetic resonant modes (Figure 1.2a) are illustrated in Figure 1.2b.

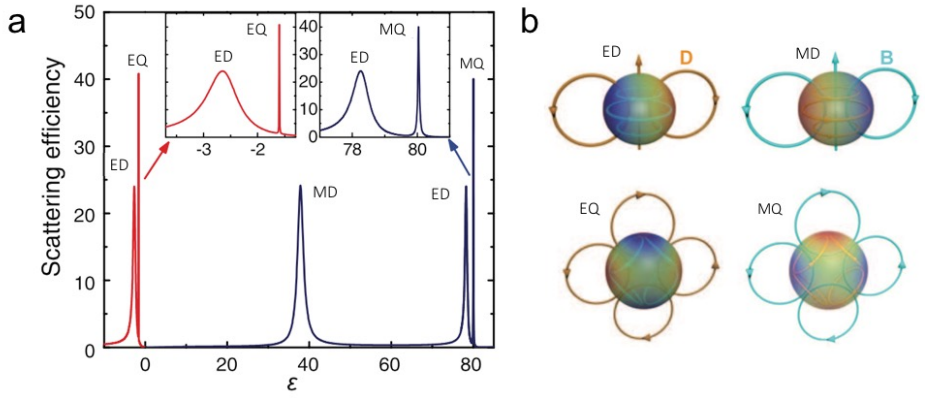

FIGURE 1.2: (a) Scattering efficiency versus dielectric permittivity ϵ for plasmonic ($\epsilon < 0$) and dielectric ($\epsilon > 0$) materials in a lossless particle with $(2\pi r)/\lambda = 0.5$. (b) Illustration of electric and magnetic field structures of different electric and magnetic resonances supported by a spherical particle (*10*).

1.3.3.2 Scattering in the Cartesian multipole expansion

As previously discussed, Mie theory provides an approach to analyse and understand light scattering problems in terms of two elementary families, the magnetic and electric multipoles, obtained from the spherical harmonic expansion. The two sets of Mie scattering coefficients a_i and b_i (see Equations 1.23 and 1.24) are conventionally associated to the magnitude of the electric and magnetic multipoles, respectively. Both coefficients are defined by imposing continuity of the transverse field components across the scatterer's surface. Thus, the scattering coefficients are not related to a particular mode of charge-current distribution, instead they are related to the spatial structure or pattern of the scattered field.

Another approach in the study of scattering properties of radiating sources is to use the current Cartesian multipole expansion. In the Cartesian multipole expansion, scattering is described in terms of charge-current distributions which includes contributions from the electric, magnetic, and toroidal multipoles. While electric multipoles are induced by the separation of oscillating charges and magnetic multipoles are induced by enclosed circulation of electric currents, toroidal multipoles are characterised by poloidal currents which flow on the surface of a torus. Despite the differences in their charge-current distributions, the far-field scattering pattern of toroidal multipoles is indistinguishable from their electric multipole counterparts.

Also, in the near-field the differences between the two multipoles are overlooked due to the boundary conditions applied within the Mie theory, where the radial field components are neglected. As a result, the contribution of toroidal multipoles in the Mie theory is not treated separately. Instead the toroidal multipole contribution is already included in the Mie coefficients, conventionally associated to electric and magnetic multipoles, and cannot be separated without knowledge of the actual charge-current distribution. In the frame of the Cartesian multipole expansion, the family of toroidal moments are immediately recognized, facilitating the description of fundamental scattering processes. The main contributions of the Cartesian multiple expansion are listed below (*11*):

$$\boldsymbol{p} = \frac{1}{iw}\int \boldsymbol{J}_{sca}(\boldsymbol{r})d^3r, \tag{1.33}$$

$$\boldsymbol{m} = \frac{1}{2c}\int \boldsymbol{r}\times\boldsymbol{J}_{sca}(\boldsymbol{r})d^3r, \tag{1.34}$$

$$\boldsymbol{t} = \frac{1}{10c}\int \boldsymbol{r}(\boldsymbol{r}\cdot\boldsymbol{J}_{sca}(\boldsymbol{r})) - 2\boldsymbol{r}^2\boldsymbol{J}_{sca}(\boldsymbol{r})d^3r, \tag{1.35}$$

$$\overline{\boldsymbol{\rho^2}} = \frac{1}{2c}\int r^2(\boldsymbol{r}\times\boldsymbol{J}_{sca}(r))d^3r, \tag{1.36}$$

where $\boldsymbol{J}_{sca}$ is the scattering current density distribution, c is the velocity of the light, $\boldsymbol{p}$ is the Cartesian electric dipole (ED$_{car}$), $\boldsymbol{m}$ is the Cartesian magnetic dipole (MD$_{car}$), $\boldsymbol{t}$ is the toroidal dipole (TD), and $\overline{\boldsymbol{\rho^2}}$ is the mean-square radius (MR).

The TD was first considered by Zel'dovich in 1958 (*12*). This mode is produced by currents flowing on the surface of a torus along its meridians, as observed in Figure 1.3. The oscillating radial components of a current density forming a TD mode are very different from the ones building an ED mode. The TD and ED, however, are characterised by the same far-field scattering pattern, except for a scaling factor of ω^2. In the Mie theory the ED$_{car}$ and the TD are both incorporated in a single amplitude coefficient a_1. When the TD and the ED$_{car}$ interfere with each other, their destructive interference in the far-field creates a non-trivial radiationless charge-current distribution, as illustrated in Figure 1.3. The resulting non-radiating state, also called electric anapole state, was first proposed in 1995 (*13*). The electric anapole state produces a strongly confined near-field, exponentially localised inside the particle. Similarly, the interference of the MR with the Cartesian magnetic dipole mode MD$_{car}$ leads to the

excitation of a magnetic anapole state. The strong confinement provided by the anapole states, opens up new opportunities to enhance light-matter interactions at small scales.

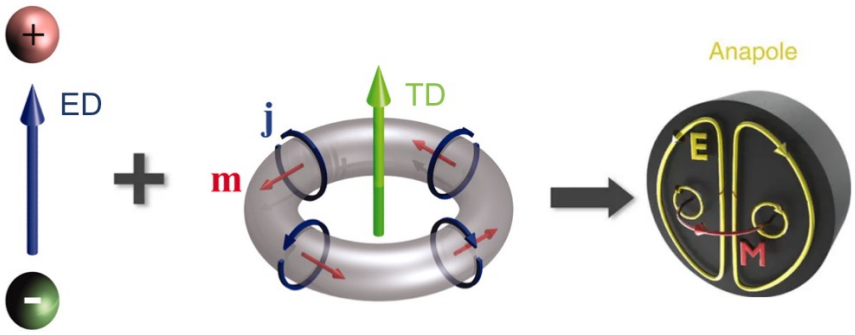

FIGURE 1.3: A pair of charges of opposite signs creates an electric dipole (ED), while currents flowing on a surface of a torus along its meridians (poloidal currents) generate a toroidal dipole (TD) (*14*). Since the radiation patterns of the ED and TD modes are symmetric, they can destructively interfere leading to total scattering cancellation in the far-field with non-zero near-field excitation. The resulting mode is called anapole state (*15*).

1.4 Optical antennas: an overview

Currently, an electromagnetic transmitter or receiver is commonly referred as antenna. Microwave and radiowave antennas have been long applied to modern technologies, ranging from satellite communications to mobile phones and televisions. Demand for antennas operating at higher frequencies led to the development of optical antennas. The characteristic dimensions of antennas, dictated by its operating wavelength, requires nanoscale structures to manipulate electromagnetic fields at the optical frequencies. Optical antennas, also called nanoantennas, had been designed and engineered using resonant nanoparticles. The resonances excited by the incident fields, enable efficient transfer of the electromagnetic energy from localised sources to the far-field and vice versa. Thus, resonant nanoparticles can operate in a similar way as radio and microwave antennas, but at optical frequencies.

1.4.1 Linear nanoantennas

When light interacts with a metallic nanoparticle at its resonant frequency, the incident electric field drives a collective oscillation of the metal's conduction electrons. The oscillation of the surface electrons produces a resonant behaviour also known as *localised surface plasmon resonance* or simply as *plasmonic resonance*, as previously discussed in Section 1.3.3.1. By localising the incident electromagnetic field on the surface of the metallic nanoparticle, the amplitude of the incident field is enhanced in the nanoantennna at length scales much smaller than the incident wavelength. Only recently, these plasmonic resonances have been studied by the scientific community, however plasmonic resonances were long ago used to generate brilliant colours in artwork pieces including stained glasses. An example of such artwork is the Lycurgus Cup, which dates back to the Roman times, where the inclusion of metallic nanoparticles into the glass induces different colours when the light is shone through the Cup as compared to when the light is reflected from the Cup.

Typically, plasmonic nanoantennas are made of gold and silver due to their low absorption which enables efficient scattering at visible and near-infrared wavelengths (*16*, *17*). Several configurations have been explored to modify the radiation or scattering properties of plasmonic nanoantennas. V-antennas have produced asymmetric radiation patterns (*18*), Yagi-Uda antennas have decreased the backward scattering (*19*), while nanoring antennas have fully eliminated this backward scattering (*20*). Applications of plasmonic nanoantennas are diverse. Gold bowties have been used to enhance the fluorescence of single-molecules (*21*), spheres nanoparticle with an ultrathin shell have been used to amplify Raman signals (*22*) and silver nanoparticles have been used to increase solar cell efficiencies by improving light confinement (*23*). Also, due to their biostability and optical properties, plasmonic nanoantennas have been used in the area of medicine to perform *In Vivo* imaging (*24*), drug and gene delivery (*25*), and magnetic resonance imaging (*26*). These applications are based on the capabilities of plasmonic nanoparticles to behave as antennas, amplifying the incoming and scattering field. However, plasmonic resonances originated by nanoparticles can behave as strongly damped oscillators and decay along different channels, mostly dissipated in the form of thermal energy. These inherent losses, constitute the major obstacle in the applications of

plasmonic nanoantennas. Moreover, in symmetric plasmonic nanoantennas only electric resonances can be excited by the incident light, as shown earlier in the case of spherical metallic particles (Section 1.3.3.1). The excitation of magnetic resonances in plasmonic nanoantennas is constrained to the use of complex geometries such as split ring resonators (*27*).

Since 1939, the use of dielectric materials in resonant structures was proposed (*28*), however only recently dielectric materials have been used in resonant nanoantennas as an alternative to plasmonic ones. High-index dielectric nanoparticles are capable of reproducing effects previously demonstrated in plasmonic nanoantennas, but with low dissipation of energy into heat. In addition to the low-losses, dielectric nanoparticles are characterised by the coexistence of electric and magnetic resonances in symmetric geometries such as spheres, as it was discussed in Section 1.3.3.1. At optical frequencies, silicon (Si) has low dissipation and a high refractive index which allows strong confinement of the incident fields. The excitation of magnetic resonances in Si nanoparticles was simultaneously demonstrated in 2012 by Evlyukhin *et al.* (*29*) and Kuznetsov *et al.* (*30*). In their work, Evlyukhin and Kuznetsov demonstrated the tunability of Mie resonances, across the visible spectrum, by changing the size of the Si nanoparticles, as shown in Figure 1.4. The nanoparticles were first studied under a dark-field optical microscope, where strong scattering was observed (see Figures 1.4a-d). Then, the scattering spectra of individual nanoparticles was measured (see bottom panel of Figure 1.4), demonstrating the ability of Si nanoparticles to change their colour due to excitation of particular modes. According to the scattering spectra, the first and strongest resonance corresponds to the MD, which shifts towards the infrared spectrum as the size of the nanoparticles increases. The MD mode is followed by the excitation of an ED and finally a MQ. The scattering spectra of the smallest nanoparticle is characterised by a single peak at blue wavelengths, corresponding to the excitation of a MD mode (see Figure 1.4a). As the size of the nanoparticle increases, the MD shifts towards the green wavelengths and a weak ED excitation appears in the spectrum (see Figure 1.4b). For a nanoparticle with size of 150 nm, green and yellow scatterings are simultaneously observed due to the excitation of an ED and a MD, respectively (see Figure 1.4c). Thus, the scattering of nanoparticles with different sizes (see Figure 1.4d), is strongly dependent of the magnetic and electric resonances excited inside the nanoparticle. The interaction between electric and magnetic resonances influences

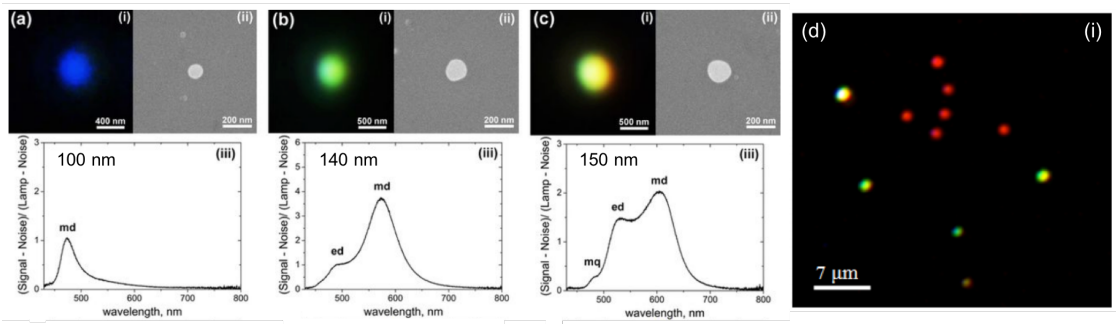

FIGURE 1.4: (a-c) (i) Close-view of dark-field microscope and (ii) SEM images from single silicon nanoparticles. (iii) Experimental dark-field scattering spectra of the corresponding (a-c) nanoparticles (*30*). (d) Dark-field microscope image of similar silicon nanoparticles fabricated by a single laser pulse on a glass receiver substrate (*29*).

the scattering properties of dielectric particles, producing tailored directional scattering in Si Yagi-Uda designs (*31*), nanodisks (*32*) and nanospheres (*33*). Also, the excitation of electric and magnetic resonances has been explored in Germanium (Ge) and Gallium Arsenide (GaAs) nanospheres, where zero backscattering was demonstrated (*34*, *35*). According to the first Kerker condition, zero backscattering is achieved by simultaneously exciting electric and magnetic dipoles to oscillate in phase and with the same magnitude (a_1=b_1).

1.4.2 Nonlinear nanoantennas

The excitation of resonances in nanoantennas is associated with the enhancement of the incident electromagnetic fields. Since nonlinear processes scale with the power of the incident fields, resonant nanoantennas have become an attractive platform to produce nonlinear signals at the nanoscale.

The study of nonlinear optical response in plasmonic nanoantennas using relatively moderate pump powers has been possible through the excitation of plasmonic resonances. Within the electric-dipole approximation of the light-matter interaction, second-order nonlinear processes from centrosymmetric materials are forbidden (see Section 1.3.2). Therefore, different strategies have been proposed to study SHG from plasmonic nanoantennas made of centrosymmetric materials such as gold and silver. For example, SHG in gold split ring-resonators and L-shaped nanoparticles has been associated to the excitation of magnetic resonances at the

fundamental wavelength (*36*). In gold sphere nanoparticles, the observation of SHG has been attributed to higher order multipolar contributions to the nonlinear polarisation, produced by retardation effects of the interacting electromagnetic fields (*37*). Meanwhile, SHG in gold nanoshells has been attributed to the locally broken centrosymmetry at the interfaces of the nanoparticles (*38*). THG also has been studied in plasmonic nanoantennas, where the nonlinear spectral properties of the nanoantennas was dominated by the linear response of the antennas (*39*, *40*). Less commonly studied are the frequency-mixing nonlinear processes such as SFG and FWM, where the incident photons at different frequencies are mixed inside the material to generate nonlinear emissions. Gold nanoparticle pairs also called gold nanodimers, have been employed to study SFG and FWM where the relative strength of the second- and third-order nonlinearities was influenced by the symmetry of the nanodimer (*41*). Another configuration used to study FWM is gold antennas consisting of two nanowires separated by a small gap, the intensity of the FWM was controlled by changing the gap size (*42*). Despite the progress achieved, the nonlinear conversion efficiencies of plasmonic nanoantennas remain limited by their inherent Ohmic losses, small resonant mode volumes and most importantly their low damage thresholds. Distinct strategies have been implemented to increase the nonlinear conversion efficiencies including resonant coupling (*43*, *44*), three dimensional geometries (*45*) and the use of hybrid nanoantennas (*46*). Despite the employment of these approaches, the observed efficiencies have remained low, in the order of 10^{-11} in the case of SHG.

Lossless all-dielectric nanoantennas have been recently used in the generation of nonlinear emissions at optical frequencies. Dielectric materials have large band gaps, from the near infrared to the ultraviolet, allowing to minimise interband transition losses induced by incident fields at optical frequencies. The negligible losses of dielectrics increase the damage threshold of dielectric naoantennas and allow to use higher intensities of the incident fields, thus enabling to obtain high nonlinear conversion efficiencies by the use of strong excitation fields. In addition, the concentration of the fields inside dielectric nanoantennas permits to obtain larger mode volumes, as compared to plasmonics, which can further increase the nonlinear conversion efficiencies. Along with the low losses and high refractive index, Si possess a

strong third-order nonlinearity, making of this dielectric material a prominent choice in the study of THG from nanoantennas.

Si nanodisks placed on silica were first employed to probe the generation of a third-order nonlinear emission at frequency 3ω, when illuminated from its back side by a laser beam with frequency ω (see left of Figure 1.5a). In the right of Figure 1.5a, the Si sample is irradiated with an invisible infrared beam indicated by the red arrow, the blue point observed corresponds to the THG scattering of the nanodisks, bright enough to be observed by naked eye (*47*). In Figure 1.5b, the measured transmission spectrum of the Si nanodisk array (see inset), given by the gray area, indicates a resonant behaviour of the Si nanodisks centred at 1.24 μm and mainly driven by a MD. The THG intensity, shown by the purple dots, was enhanced within the spectral band of the resonance. The harmonic emission showed two orders of intensity enhancement, as compared to unstructured bulk silicon. Similar results were observed in optically isolated Si nanodisks, where the enhanced THG was driven by the excitation of a MD (*48*). The interplay of both electric and magnetic resonances in the enhancement of THG was studied in the so called oligomers, structures that consist of several symmetrically positioned nanoparticles (*49*). Pronounced reshaping of the THG spectra was demonstrated due to interference of the nonlinearly generated waves and augmented by an interplay between the ED and MD resonances. The reshaping of the THG was controlled by the mutual position of the three nanodisks in the Si trimer. The possibility to tailor the THG efficiency and directionality from single and trimer Si naonoparticles has been also investigated, using simple geometries such as spheres and disks (*50*). The generation of visible frequencies in Si nanodisks has been also investigated through the nonlinear process of FWM (*51*).

On the other hand, Ge nanoparticles have been also employed in the study of THG, due to its highest refractive index among standard dielectrics and high third-order nonlinearity in the near-infrared region. In Ge nanodisks, THG has been observed at optical frequencies, enhanced at the vicinity of the anapole state (*52*). The nonlinear conversion efficiency at the vicinity of the fundamental anapole state outperformed the one corresponding to ED excitation by about an order of magnitude, and surpassed the conversion efficiency from an

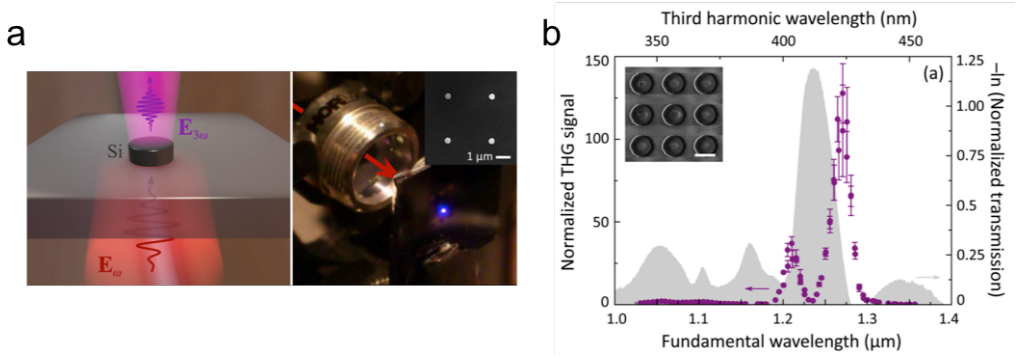

FIGURE 1.5: (a) Schematic of THG from individual silicon nanodisk on a silica (SiO_2) layer (left). Photographic image of silicon sample illuminated by an invisible infrared beam (indicated by the red arrow), the blue dot represents the scattered THG (right). (b) Negative logarithm of the normalised transmission spectrum from the array, given by the gray area, indicating a resonance centred at 1.24 μm. The THG spectrum of the sample, shown in purple dots, is strongly enhanced within the spectral band of the resonance. The inset shows an SEM image of the sample with a scale bar of 500 nm length (*47*).

unstructured Ge thin film by a factor of ten thousand. The excitation of higher-order anapole states further improved the electric field confinement within Ge nanodisks, leading to even higher THG conversion efficiencies, as compared to the excitation of the fundamental anapole state (*53*). In Ge nanodisks, studies of FWM have reported lower conversion efficiencies as compared to THG (*54*).

1.5 From optical antennas to optical metasurfaces

Metasurface are planar arrays of densely packed nanoantennas designed to modify different characteristics of the incident light including its phase, polarisation and amplitude profile. Metasurfaces capture the incident light and couple their electric and magnetic components to demonstrate effective response of the electric (permittivity) and magnetic (permeability) fields (see Equations 1.15 and 1.16) not usually found in nature. While the properties of natural materials depend on the arrangement of their atoms, the optical behaviour of metasurfaces relies in the arrangement of their nanoantennas and their collective response. In other words, the optical response of metasurfaces is governed by the scattering of individual nanoantenna and the near-field coupling between neighbour nanoantennas. The continuous progress in

fabrication technologies, such as photolithography and electron-beam lithography, together with the progressive trend to miniaturise optical devices have motivated intensive research in the field of metasurfaces.

1.5.1 Linear metasurfaces

Plasmonic metasurfaces have shown their ability to engineer the properties of light, proving potential to replace bulky optical components such as lenses, mirrors, prisms, polarisers and other elements with diverse utilities. Through the individual nanoantennas comprising plasmonic metasurfaces, the phase shift required to manipulate optical wavefronts can be achieved. Space-variant plasmonic metasurfaces offer extensive freedom to manipulate wavefronts demonstrating planar metalenses at visible (*55*), near-infrared (*56*, *57*) and telecommunication wavelengths (*58*). In the past, Fresnel zone plates consisting of transparent and opaque alternating rings were used to obtain lensing effects, through diffraction processes. Recently, plasmonic metasurfaces have been used to obtain diffractive Fresnel zone plate lenses (*58*), which can be designed to operate at several wavelengths (*59*, *60*). By merging two independent zone plate lenses in the same metasurface to correct for chromatic aberrations, achromatic lenses at a pair of visible wavelengths have been demonstrated (*59*). Likewise, imprinting phase masks into propagating Gaussian beams have been employed to obtain non conventional beams like Hermite–Gaussian beams, two-dimensional Airy beams, Bessel beams (*61*), and vortex beams (*62*) with different orbital angular momentum (*63*, *64*). Another functionality of plasmonic metasurfaces is the control over the polarisation state of the incident beam. A linearly polarised light in resonance with the cavity mode has been converted into a circular or elliptical polarisation (*65*). Phase change materials have been used in dynamic metasurfaces to modulate the linear polarisation state of visible light (*66*). The detuning of the metasurfaces resonances has been used to design half-wave plates (*67*) and quarter-wave plates (*68*). Also, metasurface have been incorporated in photodetectors to measure the polarisation state of the incident beam (*69*). Although plasmonic metasurfaces have shown many applications, their ohmic losses at visible and near-infrared frequencies degrade their performance. From the fabrication standpoint, the incompatibility of standard plasmonic

materials, such as gold and silver, with CMOS technology further limits the employment of plasmonic metasurfaces.

In the past few years, the search for highly efficient planar optical devices led to the introduction of all-dielectric metasurfaces. Negligible resistive losses are expected in all-dielectric metasurfaces when light of sub-band gap energies excites dielectric nanoparticles. In addition to minimal losses, the presence of both electric and magnetic resonances in the same frequency range enables full 2π phase control in a single dielectric structure (*70*, *71*), whereas in single plasmonic metasurfaces 2π phase control is only achieved with cross-polarised light. Similar to plasmonic metasurfaces, phase control in dielectric metasurfaces is attained by tuning the scattering of the nanoantennas composing the metasurface. Thus, by varying the dimensions of their nanoantennas, phase control and wavefront engineering can be performed in dielectric metasurfaces. Dielectric metasurfaces with different functionalities have been demonstrated in Si metasurfaces. For example, achromatic lenses with triple wavelength operation have been demonstrated (*72*). Also, Si metasurfaces have been designed to obtain other functionalities such as linear polarisation convertors (*73*), beam deflectors (*74*, *75*) and vortex beams generators (*73*, *75*, *76*).

1.5.2 Nonlinear metasurfaces

The near-field enhancement of metallic and dielectric resonant nanoantennas have been utilised to enhance nonlinear parametric processes, such as harmonic generation and frequency mixing (see Section 1.4.2). Thus, resonant nanoantennas are ideal components of planar metasurfaces, enhancing the emission of nonlinear optical waves. In bulk nonlinear crystals, efficient nonlinear conversion relies in the phase-matching condition to build up the nonlinear emission along the crystal length, typically in the order of hundred wavelengths. While in metasufaces, the light-matter interaction happens within the subwavelength thickness of their nanoparticles, where the phase-matching condition becomes irrelevant for efficient nonlinear conversion.

Studies in the generation of nonlinear processes using metasurfaces were first performed employing plasmonic materials. Efficient SHG demands breaking the symmetry of the system (see Section 1.3.2), and in plasmonic metasurfaces this is achieved by breaking the symmetry of their nanoparticles. To this effect, plasmonic metasurfaces composed of non-centrosymmetric nanoparticles such as L-shaped (*77*, *78*), U-shaped (*79*), G-shaped (*80*), V-shaped (*81*) and split ring resonators (*82*) have been explored. SHG from plasmonic metasurfaces excited at telecommunication wavelengths have been analysed, observing stronger SHG at the MD resonances, as compared with purely ED resonances (*79*). Substantial SHG enhancement has been observed in plasmonic metasurfaces when the density of nanoparticles in the array is reduced, such enhancement was attributed to spectral narrowing of the plasmon resonances through favorable interparticle interactions (*81*). Enhanced SHG has been reported in multiresonant plasmonic metasurfaces, designed to simultaneously support surface lattice resonances at the fundamental and second harmonic frequencies (*78*). Nonlinear metasurfaces have been applied for nonlinear beam shaping of second-harmonic beams, demonstrating the generation of Airy and vortex beams at the nonlinear frequency (*83*). Another application is the encoding of images where the image is readout through the SHG, while it is hidden under fundamental wave illumination (*84*). Most works in nonlinear plasmonic metasurfaces have focused in the study of SHG, however, direct (*85*–*87*) and cascaded THG (*86*) have also been reported. In the work of Sartorello *et al.*, additionally to the observation of SHG and THG, SFG and FWM were observed when the temporal overlap between the fundamental and control pulses was achieved (*87*).

While the strong near field enhancement observed in plasmonic metasurfaces is important for efficient nonlinear processes, higher conversion efficiencies have been reported in dielectric metasurfaces stemming from their volume resonant modes and higher damage thresholds. The study of nonlinear harmonic generation was first performed in Si metasurfaces. A metasurface consisting of a periodic lattice of coupled rectangular Si bar and Si disk (see left of Figure 1.6a) was designed to study THG (*88*). The rectangular bar supports an ED resonance that is directly excited by an incident electric field along the x-axis, while the disk supports a MD excited through near-field interaction with the ED mode from the bar nanoparticles. The collective oscillation of the nanoparticles suppress radiative losses whereas

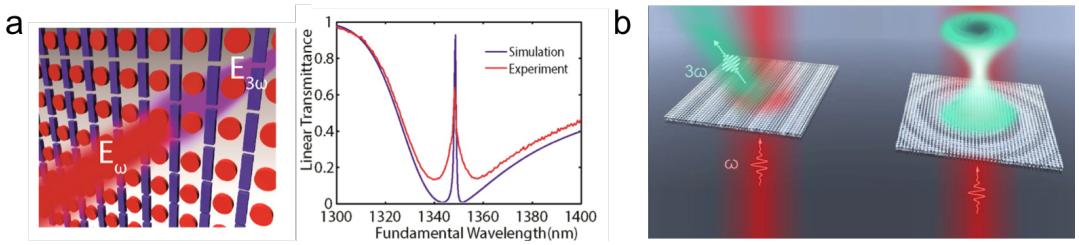

FIGURE 1.6: (a) Schematic of three photon up-conversion by a Fano-resonant silicon metasurface (left), and sharp resonance observed experimentally and in the simulation of metasurface transmittance spectra (right) (*88*). (b) Concept images of functional nonlinear metasurfaces. Left image represent a nonlinear beam deflector while right image represents a nonlinear vortex beam generator. The metasurfaces are assembled from a set of different silicon nanopillars, which generates third harmonic emissions of different phases (*91*).

the interference between the ED and MD modes induces a Fano-resonant system. As plotted in the right of Figure 1.6a, the measured and calculated transmittance acquired by normal incidence is characterised by a sharp resonance centred at 1348 nm. When the Si metasurface was excited around this sharp resonance, enhanced THG was observed. A similar approach has been reported in a Si metasurface composed of spindle-shape resonant nanoparticles, where enhanced THG was observed through the excitation of a sharp resonance (*89*). Amorphous Si metasurfaces have been designed to support broadband resonances with small angle-sensitivity of the fundamental excitation beam, thus enabling the use of tighter focal spots to study THG enhancement and perform high-resolution imaging studies (*90*). Wavefront control of THG fields has been studied in Si metasurfaces made of different sets of elliptical nanoparticles, by accumulating different phases in the THG full cover of the 2π range was achieved (*91*). The resonant-phase accumulation occurred in the regime where both electric and magnetic Mie multipoles were excited simultaneously and with comparable amplitudes. The nonlinear generation of simultaneous Mie multipoles allowed the authors to achieve high forward-to-backward THG ratio, thus demonstrating nonlinear beam deflectors and nonlinear vortex beams from a Gaussian excitation beam (see Figure 1.6b). Another application of Si metasurfaces is holographic multiplexing, realised by encoding the phase information into the THG of a single Si nanoparticle (*92*).

In addition to THG studies, Si metasurfaces have been employed to investigate second-order nonlinear processes such as SHG and SFG (*93*, *94*). The study of SHG was possible using a similar approach as nonlinear plasmonic metasurfaces, metasurfaces were made of asymmetric amorphous-Si nanoparticles (*93*). Another approach to study second-order nonlinear processes is the integration of Si metasurfaces with 2D materials having strong second-order nonlinearity. The integration of a 2D material together with the excitation of a sharp resonances allowed to observe SHG and SFG using continuous wave excitation (*94*).

CHAPTER 2

GaAs and AlGaAs compounds

In the period between 1940 and 1950, semiconductor physics was characterised by a strong emphasis in Ge and Si. The climax of this development was the invention of the transistor. In contrast, the study of semiconductor compounds was delayed for a long time due to the technological difficulties to fabricate them and the lack of characterisation techniques to study their physical properties. In addition, the theoretical model developed for elements linked by covalent bonds, like Si and Ge, could not be extended to compounds with more ionic bonds where the electrons are transferred from one atom to another, forming ions of opposite charge.

In 1952 Welker published the first paper on the semiconductor properties of III-V compounds, predicting new important characteristics of these semiconductors including their high electron mobility (*95*). A decade of intensive research followed this seminal work, at the end of which the model of the physical properties of III-V semiconductor compounds had been developed. Since then, the emphasis in the research of these semiconductors has been mainly shifted to its fabrication technology and possible applications (*96*).

2.1 Optical properties and crystalline orientation of GaAs

GaAs is a binary III-V compound semiconductor, a combination of the element gallium (Ga) and the element arsenic (As) from column III and V of the periodic table of elements, respectively. The primitive-cell of a GaAs zinc blende structure is shown in Figure 2.1. The zinc blende structure is based on the cubic space group $\bar{4}3m$ in which the lattice atoms are tetrahedrally bounded in the same arrangement as diamond-type semiconductors such as Si and Ge, with the difference that GaAs contains two different atoms in its crystalline structure.

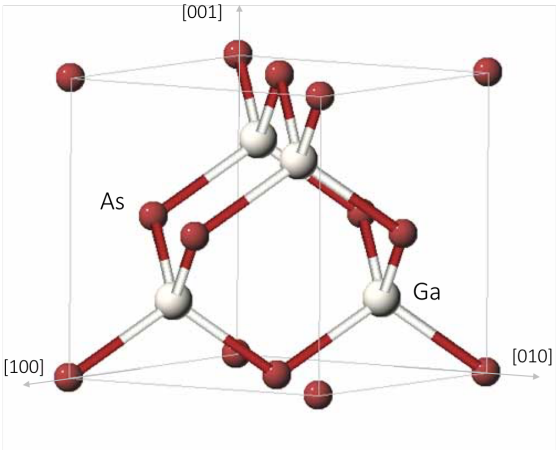

FIGURE 2.1: Primitive cell of GaAs zinc blende crystal lattice, with the three main directions of the crystal: [100], [010] and [001].

The zinc blende structure can be visualised as two interpenetrating face-centred cubic lattices, intersecting each other at one-quarter the distance along a body-diagonal. One of the lattices contains only Ga atoms and the other one contains only As atoms, the dissimilar atoms removes the inversion symmetry of the otherwise crystalline structure. In the tetrahedral bonding of GaAs, each Ga atom is bonded to four As atoms in a tetrahedron, and vice versa each As atom is bonded to four Ga atoms.

Among the group of III–V compound semiconductors, GaAs and its various $Al_xGa_{1-x}As$ alloys are the most widely reported in the literature. Like several other III-V semiconductors, GaAs has a direct band gap which makes it suitable for the development of optical sources. Other useful properties of GaAs include its controllable band gap by alloying, high refractive index and optical absorption. The fundamental band gap of GaAs is 1.42 eV which determines the lowest energy for interband transitions, where optical absorption is induced. As shown in Figure 2.2a, the absorption coefficient of GaAs is zero in the photon energy range of 0.6 to 1.42 eV, indicating GaAs is transparent material below its band gap. On the other hand, GaAs has an isotropic refractive index, due its cubic crystal structure, which increases as the photon energy increases in the range of 0.6 eV to 3.0 eV (see Figure 2.2b). At 3.0 eV the refractive index reaches its maximum value of 5.0 and afterwards it starts to decrease.

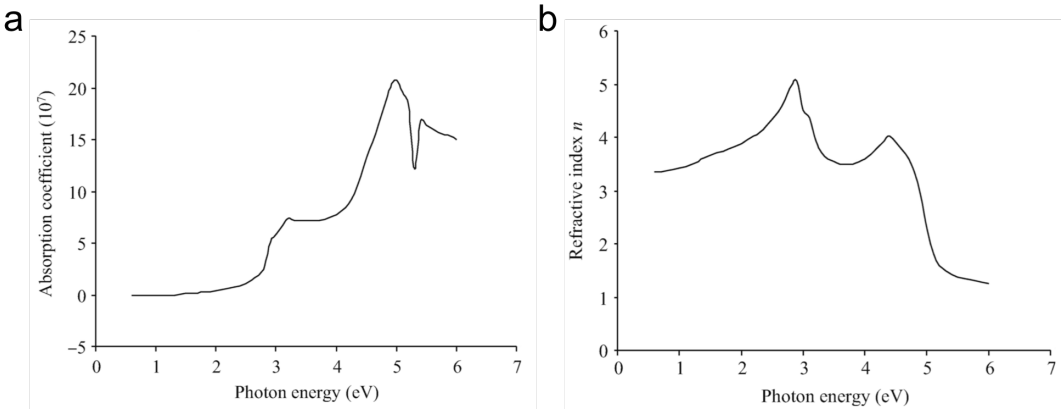

FIGURE 2.2: (a) Absorption coefficient and (b) refractive index of GaAs, as a function of the photon energy (*97*).

The band gap energy of the GaAs alloys has been obtained by Aspens *et al.* using a least-square polynomial fit (*98*),

$$E_0(x) = 1.424 + 1.594x + x(1-x)(0.127 - 1.310x). \tag{2.1}$$

According to this fitting the band gap of the $Al_xGa_{1-x}As$ alloys varies approximately from 1.42 to 2.17 eV, depending of the Al composition. The control on the band gap allows to shift the transparency region of the AlGaAs alloys from the near-infrared to visible wavelengths, *i.e.* from 870 to 570 nm. It is also known that the refractive index of a semiconductor material depends of its band gap. In the case of the AlGaAs alloys the refractive index decreases as the band gap increases (*98*, *99*).

The zinc blende structure is the simplest structure lacking of a symmetry centre, the lack of this symmetry gives the material a polarity. GaAs have two types of (111) surfaces, one that terminates with only Ga atoms and the other that terminates with only As atoms. The two types of surfaces have different physical and chemical properties explained by the different polarities of GaAs in the <111> direction. The atomic arrangement and electron density map of GaAs, given by its crystalline structure, also affects the cleave properties of the crystal. Cleave in GaAs crystals occurs along its (100), (110) and (111) surface planes. The atomic arrangement of these three surface planes and the polarity of GaAs along its <111> direction is discussed below.

Assuming the crystal of a zinc blende lattice compound remains unchanged right up to the upper surface, then three major crystalline surfaces of a zinc blende III-V compound can be pictured as follows.

- The (100)-surfaces of an $A^{III}B^{V}$ compound are formed by cubically arranged A or B atoms. Every atom in the (100)-surface is bound by two of its sp^3-bonds to atoms of the layer lying just below, as visualised by the blue atom of Figure 2.3a. The other two bonds of the atom are free, also called dangling bonds. In this case, the structure is independent of whether the topmost layer is formed by A or B atoms.
- The (110)-surfaces contain equal numbers of A atoms and B atoms. Every A or B atom on this surface has one bond with the next lower-lying layer, two bonds extending in the same surface plane to the two next-nearest neighbors, and the fourth bond is dangling (see blue atom of Figure 2.3b).
- For (111)-surfaces, two cases must be distinguished. In each case, the topmost atomic plane contains only A atoms or only B atoms (A and B surfaces). Either these can be connected by three bonds with three atoms of the next lower-lying and one dangling bond remaining, or they are bound by only one bond and have three dangling bonds (see *e.g.* blue atom in Figure 2.3c). The two cases alternate as the (111)-surface is built up layer by layer. The layers formed from A atoms and B atoms do not follow each other with equal separations. Rather, the layers connected by three bonds per atom have a smaller separation than the ones connected by only one bond per atom. Consequently, the [111]-direction and the opposite $[\bar{1}\bar{1}\bar{1}]$-direction are not equivalent; the two directions can be distinguished from one another, which means that the [111]-axis is a *polar axis* in the zinc-blende structure. This is a consequence of the absence of centre of inversion (*96*). In consequence, unlike (100) and (110) non-polar substrates, (111)-GaAs substrates are polar substrates that are either terminated with Ga or As atoms labeled as (111)A or (111)B, respectively.

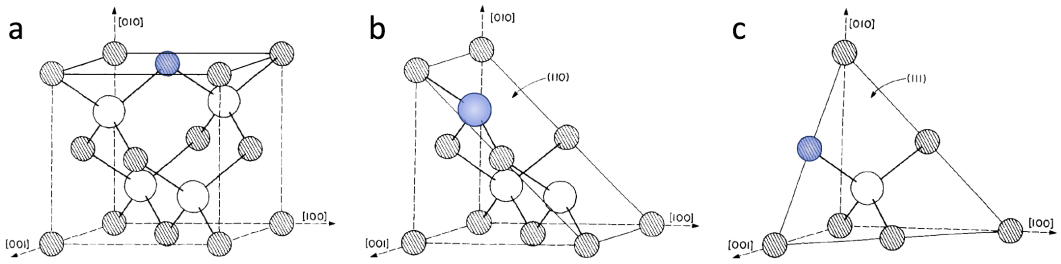

FIGURE 2.3: GaAs unit cube truncated by (a) the (100), (b) the (110) and (c) the (111) plane. In every case, the atom in blue is laying on the corresponding truncated plane (*100*).

2.2 Nonlinear optical properties of GaAs

Nonlinear optics in semiconductor materials has been rapidly developed due to their large resonant nonlinearities, control of recombination time, compatibility with other optoelectronic devices and well-developed fabrication technologies. In particular, III–V semiconductor materials have been widely used to obtain laser emission spectra (*101*, *102*).

Coherent nonlinear optical processes are produced in semiconductor materials when excited in their transparency region *i.e.* below their band gap, where the semiconductor material can be considered as a dielectric. When a semiconductor is excited below its band gap by an optical field, only virtual populations are induced inside the material which last as long as the optical field is applied. The characteristic response time of these nonlinear processes is the time required for the electron cloud to be distorted in response to an applied optical field, thus these nonlinearities are extremely fast. The nonlinear effects induced in this case are often referred as *nonresonant* processes in the sense that the optical field excitation does not coincide with any of the absorption resonances of the material. Therefore, nonresonant nonlinearities are dominated by bound-electronic states, in which case the energy of the incident optical field is not deposited in the material. The nonlinearities treated throughout this thesis are nonresonant.

The nonlinear polarisation of materials can be described by the relation

$$P_i^{NL} = \sum_{j,k} \chi_{ijk}^{(2)} E_j E_k + \sum_{j,k,l} \chi_{ijkl}^{(3)} E_j E_k E_l + ..., \tag{2.2}$$

as previously discussed in Section 1.3.2 (see Equation1.18). Here, the second- and third-order nonlinear susceptibilities are written using the subindices *i,j,k,l* to denote their tensor nature and to treat the components of the electric field vector; $\chi^{(2)}$ is a third-rank tensor while $\chi^{(3)}$ is a fourth-rank tensor.

The number of non-zero elements describing the nonlinear susceptibility of materials depends upon the symmetry of the system. Due to its zinc blende structure, the second-order susceptibility of the GaAs compound contains only three non-vanishing and off-diagonal elements $\chi^{(2)}_{zxy}$=$\chi^{(2)}_{xzy}$=$\chi^{(2)}_{xyz}$, resulting in a highly anisotropic second-order nonlinear emission. The subindices *x*, *y* and *z* refer to the principal axes of the GaAs crystal: [100], [010] and [001] as shown in Figure 2.1. Following Kleinman symmetry and contracted notation, the second-order susceptibility tensor of the GaAs can be written as:

$$\chi^{(2)}_{ZB} = 2d_{ZB} = 2\begin{pmatrix} 0 & 0 & 0 & d_{14} & 0 & 0 \\ 0 & 0 & 0 & 0 & d_{25} & 0 \\ 0 & 0 & 0 & 0 & 0 & d_{36} \end{pmatrix}, \tag{2.3}$$

where d_{14}=d_{25}=d_{36}= 370 pm/V for GaAs (*103*). Thus, according to Equation 2.2, the nonlinear polarisation leading to second-harmonic generation can be described as

$$\begin{pmatrix} P_x(2\omega) \\ P_y(2\omega) \\ P_z(2\omega) \end{pmatrix} = 2\epsilon_0 \begin{pmatrix} 0 & 0 & 0 & d_{36} & 0 & 0 \\ 0 & 0 & 0 & 0 & d_{36} & 0 \\ 0 & 0 & 0 & 0 & 0 & d_{36} \end{pmatrix} \begin{pmatrix} E_x(\omega)E_x(\omega) \\ E_y(\omega)E_y(\omega) \\ E_z(\omega)E_z(\omega) \\ 2E_y(\omega)E_z(\omega) \\ 2E_x(\omega)E_z(\omega) \\ 2E_x(\omega)E_y(\omega) \end{pmatrix}. \tag{2.4}$$

According to the above expression, we can calculate the SHG in GaAs nanoantennas. In (100)-GaAs nanoantennas, the principal axes of the crystal are aligned to the laboratory coordinate system. In this case, the induced second-harmonic currents can be directly obtained by substituting the nonlinear polarisation (Equation 2.4) in the expression of the polarisation current density earlier discussed in Section 1.3.1 (see Equation 1.13). However, in the case of (110)- and (111)-GaAs nanoantennas the principal axes of the crystal are no longer aligned

to the laboratory coordinate system. Therefore, a transformation is required to know the direction of the optical field in the frame of the crystallographic system. To transform the incident optical electric field $\vec{\boldsymbol{E}}$ (E_x,E_y,E_z) from the laboratory coordinate system *(x, y, z)* to the principal axes of the crystal *(x', y', z')*, a transformation matrix denoted by $\boldsymbol{T}$ is used as follows

$$\begin{pmatrix} E_{x'} \\ E_{y'} \\ E_{z'} \end{pmatrix} = \boldsymbol{T} \begin{pmatrix} E_x \\ E_y \\ E_z \end{pmatrix}. \tag{2.5}$$

The matrix $\boldsymbol{T}$ is expressed by the multiplication of three matrices with the Euler angles α, β, and γ, according to $\boldsymbol{T}$=$R(\alpha,\mathbf{e}_z)R(\beta,\mathbf{e}_y)R(\gamma,\mathbf{e}_x)$. The corresponding transformation matrix for (110)-GaAs based nanoantennas is (*104*)

$$\mathbf{T} = \begin{pmatrix} cos\alpha & sin\alpha & 0 \\ -sin\alpha/\sqrt{2} & cos\alpha/\sqrt{2} & 1/\sqrt{2} \\ sin\alpha/\sqrt{2} & -cos\alpha/\sqrt{2} & 1/\sqrt{2} \end{pmatrix}.$$

In the case of (111)-GaAs based nanoantennas the corresponding transformation matrix is (*105*)

$$\mathbf{T} = \begin{pmatrix} cos\gamma & cos\beta sin\gamma & sin\beta sin\gamma \\ -sin\gamma & cos\beta cos\gamma & cos\beta cos\gamma \\ 0 & -sin\gamma & cos\beta \end{pmatrix}.$$

Once the incident electric field is obtained in the crystalline coordinate system, the components of the electric field are applied to the nonlinear polarisation (Equation 2.2), obtaining a similar expression as the one shown in Equation 2.4. Subsequently the induced nonlinear currents are obtained in the crystalline coordinate system, according to Equation 1.13. Finally, the nonlinear currents are transformed back to the laboratory coordinate system according to

$$\begin{pmatrix} J_x \\ J_y \\ J_z \end{pmatrix} = \boldsymbol{T}^{-1} \begin{pmatrix} J_{x'} \\ J_{y'} \\ J_{z'} \end{pmatrix}. \tag{2.6}$$

The third-order nonlinear behaviour of GaAs is related to its third-order optical susceptibility tensor. Due to its cubic, zinc blende symmetry, GaAs have just four independent, non-zero tensor elements $\chi^{(3)}_{xxxx}$, $\chi^{(3)}_{xyxy}$, $\chi^{(3)}_{xyyx}$ and $\chi^{(3)}_{xxyy}$. In the case of a degenerate processes (with a single incident frequency) such as THG, intrinsic permutation symmetry dictates $\chi^{(3)}_{xyxy}$=$\chi^{(3)}_{xyyx}$ and in this case the four elements are reduced to only three.

2.3 Progress in nonlinear GaAs nanoantennas and GaAs metasurfaces

Despite the progress achieved in enhancing third-order nonlinear effects in Si and Ge nanoantennas, bulk second-order nonlinearities remained unexplored in these materials due to their centrosymmetric crystalline structure. The employment of materials with bulk second-order nonlinear susceptibilities would intrinsically increase the conversion efficiency due to their lower-order nonlinearity (see Section 1.3.2). Nanoantennas made of III–V semiconductors such as GaAs are good candidates for the study of second-order nonlinear effects since they posses high-refractive index and relatively large second-order susceptibilities.

AlGaAs nanoantennas were studied theoretically for the first time by Luca *et al.* In their work, Luca *et al.* designed AlGaAs nanoantennas to exhibit a magnetic dipole resonant behaviour at near-infrared wavelengths, as illustrated in Figure 2.4a. The bulk second-order nonlinear effects associated to the magnetic dipole resonance were analysed predicting SHG conversion efficiencies exceeding 10^{-3}, when a pump intensity of 1 GW/cm^2 is used (*106*). The prediction of this high conversion efficiency has lead to a great interest of this semiconductor material for optical antennas. The SHG radiation pattern of AlGaAs nanoantennas has been calculated under different polarisation states and incident angles of the pump beam (*107*). Normal SHG was obtained by tuning the incident angle of the pump beam, as shown in Figure 2.4b.

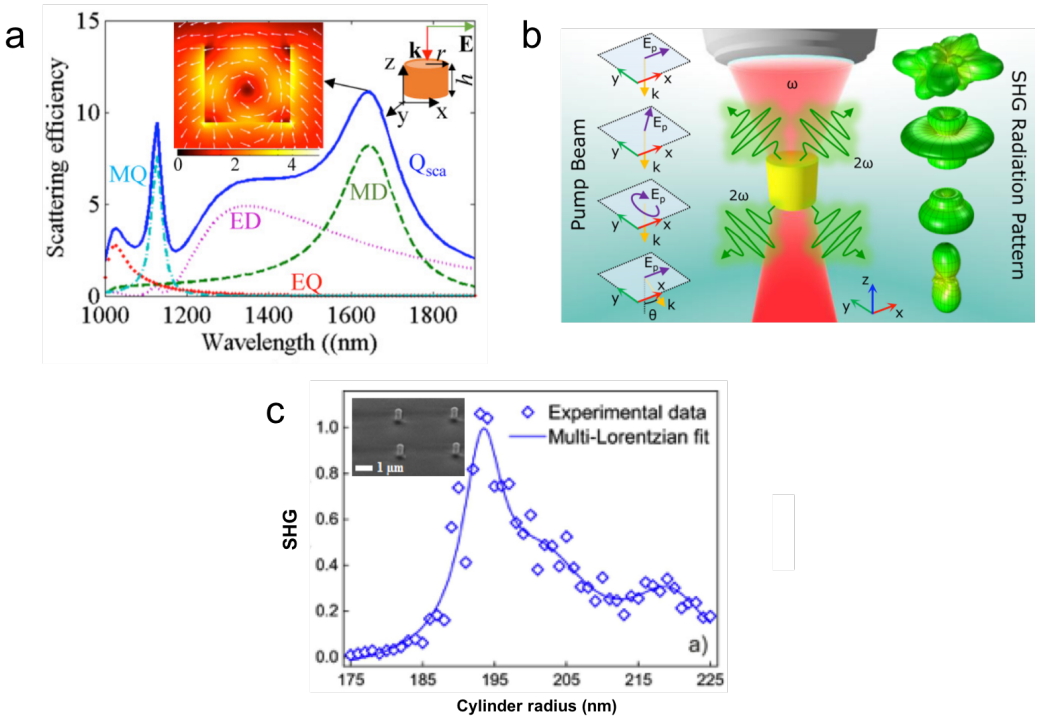

FIGURE 2.4: (a) Decomposition of the total scattering efficiency (Q_{sca}) of an AlGaAs cylinder with a radius of 225 nm and height of 440 nm, as a function of the incident wavelength. The decomposition shows four main contributions to the Q_{sca}: magnetic dipole (MD), electric dipole (ED), magnetic quadrupole (MQ), and electric quadrupole (EQ). The electric field distribution at the MD resonance is shown in the inset, where the arrows represent the electric field in the *xz* plane (*106*). (b) Conceptual representation of SHG radiation pattern engineering. A red pump beam with a frequency ω in the near-infrared is focused by a microscope objective on the cylindrical nanoantenna. The second-harmonic process generates green light of frequency 2ω which is emitted in different directions (see radiation patterns in the right side), according to the polarisation state E_p and angle of incidence (see *k*) of the pump beam (*107*). (c) Measured SHG intensity as a function of the cylindrical nanoantenna radius. The experimental points were fitted to a multi-Gaussian function featuring three distinct peaks. A SEM image of the fabricated AlGaAs nanoantennas is shown in the inset (*108*).

Experimentally, a SHG conversion efficiency exceeding 10^{-5} has been demonstrated in optimised AlGaAs nanoantennas (see Figure 2.4c), driven by the excitation of a magnetic dipole resonance centred at 1550 nm (*108*). Also, polarisation-resolved measurements in AlGaAs nanoantennas have shown control over the SHG through the excitation of nonlinear multipolar modes (*109*).

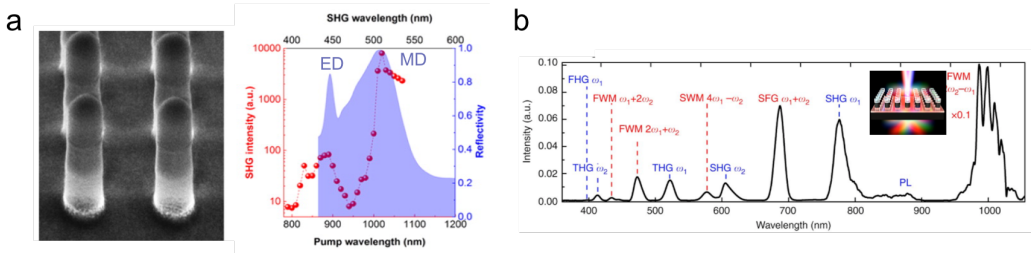

FIGURE 2.5: (a) At the left, a 75° side view SEM image of fabricated GaAs metasurface. At the right, measurements of SHG intensity (using logarithm scale) showing higher enhancement of the harmonic when excited at the magnetic resonance, as compared to the electric resonance excitation. The measured reflectivity of the metasurface is shown in the blue background (*110*). (b) Nonlinear spectrum exhibiting eleven peaks generated from seven different nonlinear processes, when two optical beams at λ_2 1.24 μm and λ_1 1.57 μm simultaneously excite a GaAs metasurface. The nonlinear processes requiring only one excitation beam such as harmonic generation and photoluminescence are indicated by blue labels. The nonlinear processes involving both excitation beams are indicated by red labels. In the inset, an optical metamixer consisting of an square array of GaAs resonators is shown to be excited by two infrared beams, generating a variety of new frequencies (*114*).

Also the study of SHG has been performed in GaAs metasurfaces. Strong SHG has been reported by Liu *et al.* in GaAs based metasurfaces driven by the field enhancement of the fundamental field at the magentic dipole resonance, as shown in Figure 2.5a (*110*). The SHG polarisation-dependence and spatial emission properties have been studied in GaAs (*111*) and AlGaAs metasurfaces (*112*). GaAs-based metasurfaces have been designed, using broken symmetry, to produce a sharp resonance at the fundamental beam and enhance the SHG (*113*). An optical frequency mixer has been demonstrated in a GaAs-based metasurface where eleven new frequencies were generated, spanning from the ultraviolet to near-infrared, as shown in Figure 2.5b. The new frequencies were originated from even and odd order nonlinearities of the metasurface (*114*).

2.4 Fabrication of GaAs-based nanoantennas: our approach

In general, there are two approaches for the fabrication of III-V nanostructures: top-down and bottom-up. The top-down approach is based on the etching or milling of a bulk material to shape nanostructures using nanofabrication tools such as focused ion beam milling and electron-beam lithography. While, the bottom-up approach relies on self-assembly schemes to growth nanostructures from smaller building blocks. In this thesis, the top-down approach was used to fabricate size-controlled GaAs-based nanoantennas.

First, III-V semiconductor planar layers were grown using metal-organic chemical vapour deposition (MOCVD). MOCVD is an epitaxial growth technique which relies on metal organics mixed in a gaseous form to obtain high quality crystalline films. The substrate wafer acts as a seed crystal providing the growth direction of the semiconductor crystal. A 20 nm layer of AlAs was grown on a (100)-cut GaAs wafer, followed by a 300 nm layer of $Al_{0.2}Ga_{0.8}As$. The planar growth was terminated with a 15 nm thick GaAs layer to prevent the oxidation of the AlGaAs layer when it is exposed to atmosphere, while the first AlAs layer is used as a lift-off buffer layer. The formation of defects or undesired structures can be avoided in the interface between the different semiconductor layers, grown on the top of each other, thanks to the perfect lattice match among all $Al_xGa_{1-x}As$ alloys, for any value of x. The identical crystal parameters of GaAs and AlAs results in the perfect lattice match among all among all AlGaAs alloys. A SiO_2 layer was deposited on the top of the GaAs layer (see Figure 2.6a) via plasma-enhanced chemical vapor deposition (PECVD). Conventional electron beam lithography procedure was used to obtain a resist patterning on the underlying SiO_2 layer. The electron beam pattern was transferred to the SiO_2 layer via an inductively coupled plasma (ICP) machine, creating a hard mask. Subsequently, the remaining resist was removed by wet etching. The SiO_2 hard mask was then transferred to the three underlaying semiconductor layers by an additional ICP step, as illustrated in Figure 2.6b. The SiO_2 hard mask and the AlAs layer were removed with buffered hydrofluoric (HF) wet etch, as shown in Figure Figure 2.6c. To decrease surface adhesion of the GaAs substrate, the sample was

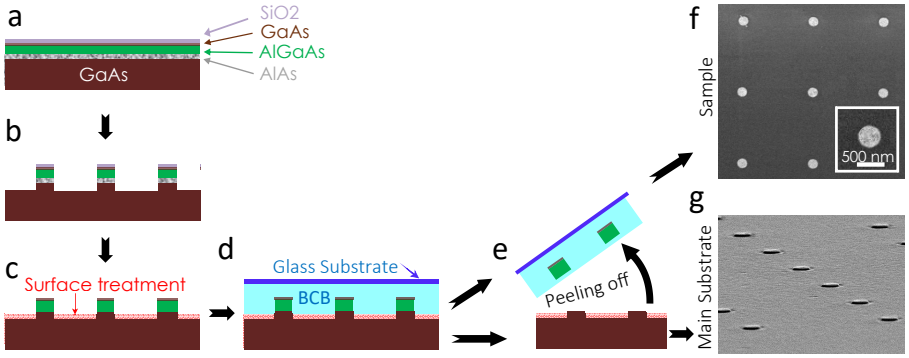

FIGURE 2.6: Fabrication procedure of AlGaAs nanoantennas in a transparent media. (a) Deposition of AlAs, AlGaAs and GaAs layers on a [100] GaAs wafer using MOCVD, followed by a SiO_2 layer deposited via PECVD (b) Formation of SiO_2 mask via electron-beam lithography followed by the fabrication of patterned AlGaAs nanodisks via sequential etching. (c) Development of a nonadhesive surface using a Cl_2 treatment. The SiO_2 mask and the AlAs buffer layer were removed by HF acid. (d) Coating of a BCB layer followed by curing and bonding it to a thin glass substrate. (e) Peeling off the AlGaAs nanodisks embedded in the BCB layer. Scanning electron micrograph images: (f) top view of the sample and (g) side view of the remaining GaAs wafer after peeling.

treated with chlorine gas in an ICP machine. Next, a 4 μm layer of benzocyclobutene (BCB) was spin coated onto the sample, followed by its curing and bonding to a thin glass substrate, as illustrated in Figure 2.6d. Finally, the glass substrate with the AlGaAs disks embedded in the BCB layer was peeled off from the main GaAs wafer, as illustrated in Figure 2.6e. The glass substrate was easily peeled off from the GaAs substrate due to the surface treatment previously performed (see Figure 2.6c) which significantly reduced the adhesion of the BCB layer to the GaAs substrate. Electron microscopy images of the AlGaAs nanodisk embedded in BCB and the stubs remaining in the original substrate can be observed in Figures 2.6f and g, respectively.

The final sample consists of (100)-AlGaAs crystalline nanodisks on a glass substrate, partially embedded in a transparent BCB polymer layer which has a refractive index equivalent to the one from the glass. By placing the AlGaAs nanodisk in a low-index substrate, high optical contrast between the nanodisk and the substrate is obtained enhancing the confinement of the incident field. Additionally, the transparent substrate allowed the study of the forward and backward scattering of the nanodisks. The nanodisks have a constant height $h = 300$ nm

and different diameters d ranging from 340 to 690 nm. A distance of 5 μm between each nanodisk was chosen to avoid lattice effects in the nonlinear experiments, *i.e.*, the separation among neighbor disks is large enough compared to the spot size of the focused beam (see *e.g.* Figure 3.5 where the spot size is $\approx$1.0 μm). The nanodisks have a zinc blende crystal structure with a crystalline orientation as shown in Figure 3.1.

A similar fabrication procedure was used to obtain (110)- and (111)-GaAs nanodisks where the main difference in the fabrication procedure consists in the use of (110)- and (111)-cut GaAs wafers, more details can be found in Section 5.2. As discussed earlier in Section 2.3 different approaches have been implemented to manipulate the SHG properties of GaAs-based nanoantennas including the use of different polarisation states of the pump beam and geometrically designed nanoantennas. However, the change of the crystalline orientation has not been yet explored by any other research group. In our work, (111)- and (110)-GaAs nanoantennas were used to manipulate the properties of the second-order nonlinear emission, as it will be discussed in chapter 5.

Broadly speaking, in the works previously discussed (see Section 2.3) the GaAs nanoantennas are fabricated using EBL, sequential etching and selective wet oxidation. The wet oxidation is performed to provide a low-refractive-index native oxide layer between the nanoantennas and the GaAs substrate, thus enabling the confinement of the electromagnetic field inside the nanoantennas through the different refractive indices of the oxide layer and nanoantenna. These fabrication procedures prevents the measurement of the forward nonlinear emission, which is absorbed by the GaAs substrate. Compared to these procedures, our novel approach enables to measure the forward and backward nonlinear emissions simultaneously, due to the transparent environment and substrate. In the following chapter, I present the studies performed in the nonlinear emission of (100)-AlGaAs nanoantennas, these nanoantennas were fabricated using the procedure explained in this Section.

CHAPTER 3

Resonant harmonic generation in (100)-AlGaAs nanoantennas probed by CVBs

---

3.1 Introduction

Nonlinear harmonic generation in semiconductor nanostructures depends on the properties of the excitation beam and its coupling to the nanostructure. For example, a polarisation-dependent behaviour has been observed in the SHG from semiconductor nanostructures. This behaviour can be explained by the coupling of different polarisation states of the fundamental beam to the second-order susceptibility tensor of the material. Recently, the polarisation-dependent behaviour of SHG has been used to determine the crystallographic structure and crystalline orientation of nanostructures made of non-centrosymetric materials (*115–119*). Radially-polarised (RP) and azimuthally-polarised (AP) cylindrical vector beams (CVBs) possess a spatially variant polarisation state, making them suitable to study the polarisation dependence of nonlinear signals generated by semiconductor nanostructures. The use of CVB to study nanostructures present some other advantages including selective excitation of resonant modes (*120*), highly position-sensitive transverse scattering (*121*) and enhancement of nonlinear conversion efficiencies (*122*). In this chapter, we investigate SHG and THG of individual AlGaAs nanoantennas excited by CVBs, using a far-field mapping technique (*123*). The nonlinear scanning maps describe the polarisation-dependence of SHG and THG and determine the crystalline orientation of AlGaAs nanoantennas. In addition to the polarisation-dependence studies, we demonstrate enhanced second- and third-harmonic emission of AlGaAs nanoantennas driven by the excitation of anapole-assisted modes.

3.2 Methods

Before we present the nonlinear scanning maps of individual AlGaAs nanoantennas, we describe the optical system used to measure them as well as describe the mathematical method used to simulate the corresponding maps -the method of moments.

3.2.1 Optical system

The AlGaAs nanoantennas were excited by a linearly polarised (LP) femtosecond laser beam at an excitation wavelength of 1060 nm, a pulse width of 140 fs and a repetition rate of 80 MHz. At the output of the laser cavity, a telescopic system and a pinhole was used to clean the beam. The telescopic system was built by two lenses, with focal lengths $f_{1,2}$ = 50 mm, separated by 10 cm. A pinhole with a diameter of 75 μm was carefully placed at the focal length of the first lens to clean the beam. After the telescopic system, a half-wave plate (HWP) was used to rotate the linear polarisation state of the fundamental beam, and a beam expander to completely fill the numerical aperture (NA) of the microscope objective. An infinity-corrected microscope objective ($50\times$ magnification and NA of 0.8) tightly focused the beam to a spot size of $\approx$1.0 μm onto the AlGaAs nanoantennas. A three-axis motorised translation stage was used to position the AlGaAs nanoantennas precisely within the focal plane of the objective lens. The same microscope objective collected the fundamental beam reflected by the sample, as well as the backward SHG of the nanoantennas. The sample was moved along the *xy* plane collecting the optical signals pixel-by-pixel in a scanning mode, *i.e.* as a function of the sample position with respect to the focused fundamental beam. The step size of the scanning mode was set to 150 nm. The backward SHG was spectrally separated from the reflected fundamental beam by an appropriate dichroic beamsplitter and bandpass filters. A cooled photomultiplier tube was used to detect the SHG pixel-by-pixel, to eventually obtain a SHG scanning map of the AlGaAs nanoantennas. A schematic of the optical system described above is shown in Figure 3.1. To locate the microscopic area of interest, a bright-field imaging arm was used. In all the measurements, an input laser power of 1 mW and a pixel dwell time of 50 ms were used.

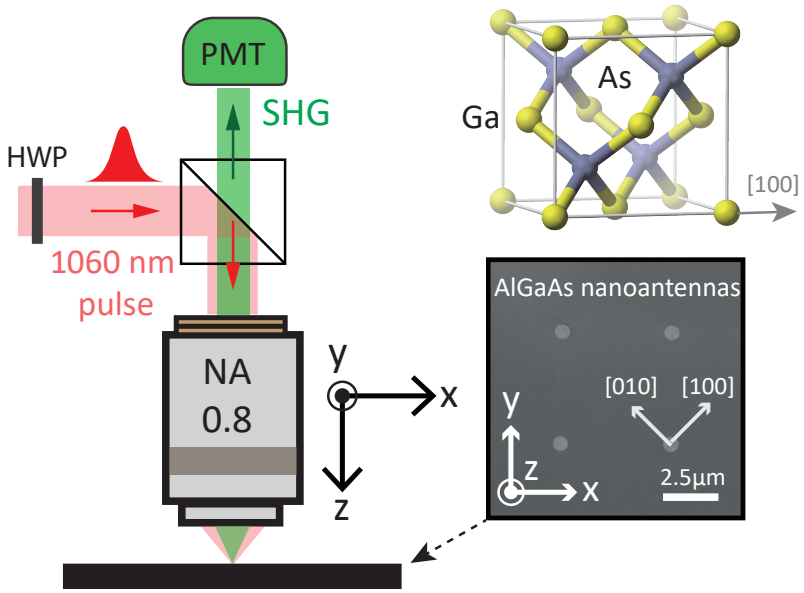

FIGURE 3.1: Schematic of the nonlinear microscopy experiment. The polarisation of a linearly polarised (LP) gaussian beam is controlled by a half-wave plate (HWP). Then, the LP excitation beam is focused on the AlGaAs nanoantennas by a microscope objective with a numerical aperture (NA) of 0.8. The reflected LP beam and the SHG are collected with the same microscope objective. The reflected fundamental beam is separated from the SHG by a dichroic beamsplitter and bandpass filters. A photomultiplier tube (PMT) detects the SHG. In the right, a scanning electron microscopy image of AlGaAs nanoantennas with a diameter of 585 nm is shown, together with its crystalline orientation.

3.2.2 Method of Moments

The method of moments (MoM) is the mathematical procedure used to reduce a functional equation to a matrix equation in order to solve linear field problems. A problem is deterministic if its solution is unique. In such a case, the problem is considered solved when it has been reduced to a suitable matrix equation, since the solution is given by matrix inversion. The method of moments gives a general procedure for treating field problems, but the details of the solution vary widely depending of the particular problem to solve (*124*).

In order to numerically solve electromagnetic problems via the MoM, the differential form of Maxwell's equations is converted into surface integral equation (SIE) form, therefore this method is a surface-base method. To convert Maxwell's equations into the matrix form, the

equations are cross-examined via the MoM with testing functions. The testing functions can be the same as the basis functions chosen in the SIE formulation (*125*), when the Galerkin's method is used. In the SIE formulation, the equivalent surface currents are approximately expanded into a sum of weighted basis functions, such as the Rao–Wilton–Glisson (RWG) functions. The RWG functions describe the particle surface by a triangle mesh and use a first order representation of the electric and magnetic tangential field components on the surfaces. To study nonlinear optical scattering processes, the original nonlinear problem is generally treated under the undepleted approximation and linearised into several problems such that each of them can be solved using the MoM as described above.

In this chapter the MoM was used to solve linear and weakly nonlinear scattering problems by numerical computation adopting the Galerkin's method. The particle size is of the order of the incident wavelength, the material is described by a piece-wise constant complex permittivity and the bulk nonlinearities were the only ones considered.

3.3 Scanning maps with linearly polarised (LP) beams

Although the present chapter is dedicated to the study of nonlinear scanning maps using CVBs, first we present the nonlinear scanning maps of individual AlGaAs nanoantennas obtained by using LP excitation beams. This will allow us to compare the nonlinear microscopy technique proposed using CVBs to the conventional method using LP beams.

Four similar-sized AlGaAs disk nanoantennas with a diameter (d) of 327 nm, were studied using the nonlinear microscopy system described in Section 3.2.1. The SHG scanning maps obtained using a LP excitation at two polarisation angles, 0° and -45° with respect to the laboratory coordinate system, are shown in Figure 3.2. The scanning maps revealed a spot-like intensity distribution that correspond to the locations of the nanoantennas and a sharp contrast between the nanoantennas and the substrate SHG that suggests the nanoantennas are the main source of SHG. Another important feature observed in Figure 3.2 is the different SHG intensities generated by the two different polarisation angles of the fundamental beam. A higher SHG intensity is observed when the nanoantennas are illuminated by a 0° beam,

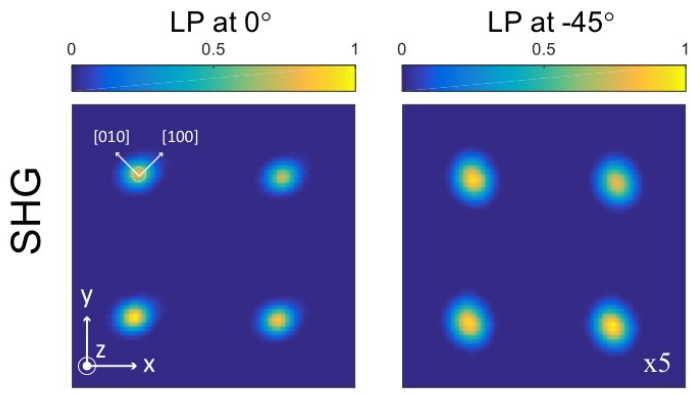

FIGURE 3.2: Experimental SHG far-field scanning maps from AlGaAs nanoantennas with a diameter of 327 nm, excited by a linearly polarised (LP) beam at 0° (*i.e.*, along the *x*-axis) and a LP beam at -45° (*i.e.*, along (010) crystal axis). The relative SHG scanning maps were plotted with respect to the maximum SHG intensity obtained by the excitation of a LP beam at 0°. The image size is 9.6 μm $\times$ 9.6 μm.

as compared to the -45° illumination. These variations in the SHG intensity indicate the nonlinear process is polarisation-dependent.

SHG scanning map simulations were employed to reproduce the SHG from AlGaAs nanoantennas. The simulations were performed using the MoM (*122*, *126*), where a single AlGaAs disk is embedded in a homogeneous medium (with a refractive index n = 1.44) and the nonlinearities of the disk are dominated by the bulk response of the material. Figure 3.3 shows the calculated SHG scanning maps from single AlGaAs disks nanoantennas of different diameters: 330, 430 and 530 nm, excited by LP beams at 0° and -45°. The calculated SHG scanning maps shown on the left side of Figure 3.3 (see d = 330 nm) agree with the corresponding measured maps shown in Figure 3.2, both exhibiting a spot-like SHG intensity distribution, and a high contrast between the SHG from the nanoantenna and the substrate. Also, the calculated scanning maps reproduce the higher SHG intensity when the nanoantenna (d = 330 nm) is excited by a LP beam at 0°, as compared to a LP excitation at -45°. The same trend was observed in AlGaAs nanoantennas with diameters of 430 and 530 nm, where the SHG is higher for a LP excitation at 0°, as compared to -45° (see Figure 3.3). In the calculations, the ratio between the SHG intensity generated by a LP beam at 0° and -45° becomes larger as the

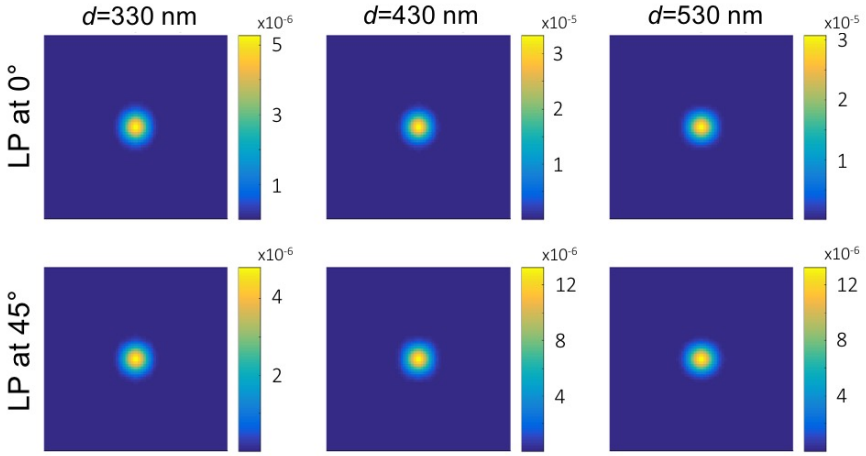

FIGURE 3.3: Calculated far-field SHG scanning maps from single AlGaAs disk nanoantennas of different diameters: 330, 430 and 530 nm, excited by linearly polarised beams (LP) at two polarisation angles. The calculations were performed using the method of moments (MoM). Each image was normalised to the incident beam amplitude and their maximum intensity values (a.u.) are shown here.

diameter of the AlGaAs nanoantennas is increased. The variations of SHG intensity with the incident polarisation angle indicate the nonlinear process is polarisation-dependent.

3.4 Cylindrical Vector Beams (CVBs)

Conventionally, the polarisation dependency of nonlinear harmonic processes is studied by rotating the polarisation angle of a LP Gaussian beam across the substrate-plane. In this thesis, we employ CVBs to study the polarisation-dependence of nonlinear emissions generated by AlGaAs nanoantennas.

The CVBs are vector solutions of Maxwell's equations that obey axial symmetry in both amplitude and phase. Specific cases of CVBs are the beams with cylindrically symmetric radial or azimuthal polarisation distribution. The RP and AP CVBs can be expressed as a superposition of orthogonallly polarised Hermite-Gausssian modes:

$$\boldsymbol{E}_r = HG_{10}\vec{e}_x + HG_{01}\vec{e}_y, \tag{3.1}$$

$$\boldsymbol{E}_{\phi} = HG_{01}\vec{e}_x + HG_{10}\vec{e}_y, \tag{3.2}$$

where $\boldsymbol{E}_r$ and $\boldsymbol{E}_{\phi}$ represent the RP and AP electric fields, respectively; $\vec{e}_x$ and $\vec{e}_y$ are the unit transverse cartesian vectors. The radial and azimuthal polarisation distribution of the CVBs is illustrated in Figure 3.4 are indicated by green arrows.

When focused, the spatially variant polarisation state of the RP and AP CVBs exhibit unique three dimensional focal field components. In the case of a RP CVB, the field components are expressed as:

$$\begin{aligned}
\boldsymbol{E}(\rho,\phi,z) &= \frac{ikf^2}{2\omega_0}\sqrt{\frac{n_1}{n_2}}E_0 e^{-ikf}\begin{bmatrix} i(I_{11}-I_{12})cos\phi \\ i(I_{11}-I_{12})sin\phi \\ -4(I_{10}) \end{bmatrix}, \\
\boldsymbol{H}(\rho,\phi,z) &= \frac{ikf^2}{2\omega_0 Z_{\mu\epsilon}}\sqrt{\frac{n_1}{n_2}}E_0 e^{-ikf}\begin{bmatrix} -i(I_{11}+3I_{12})sin\phi \\ i(I_{11}+3I_{12})cos\phi \\ 0 \end{bmatrix}.
\end{aligned} \tag{3.3}$$

For an AP CVB, the focal field components are:

$$\begin{aligned}
\boldsymbol{E}(\rho,\phi,z) &= \frac{ikf^2}{2\omega_0}\sqrt{\frac{n_1}{n_2}}E_0 e^{-ikf}\begin{bmatrix} i(I_{11}+3I_{12})sin\phi \\ -i(I_{11}+3I_{12})cos\phi \\ 0 \end{bmatrix}, \\
\boldsymbol{H}(\rho,\phi,z) &= \frac{ikf^2}{2\omega_0 Z_{\mu\epsilon}}\sqrt{\frac{n_1}{n_2}}E_0 e^{-ikf}\begin{bmatrix} i(I_{11}-I_{12})cos\phi \\ i(I_{11}-I_{12})sin\phi \\ -4(I_{10}) \end{bmatrix}.
\end{aligned} \tag{3.4}$$

The I_{nm} integrals appearing in Equations 3.3 and 3.4 (*127*) are dependent on the apodization and Bessel functions of different orders; the entire expression of these integrals can be found in Appendix A. Due to the polarisation distribution of these beams, a RP CVB exhibits a strong longitudinal electric field (see Equation 3.3), while the AP CVB exhibits no longitudinal electric field (see Equation 3.4). However, both CVBs maintain their transversal electric field distribution. The transversal and longitudinal components of focused RP and AP CVBs can

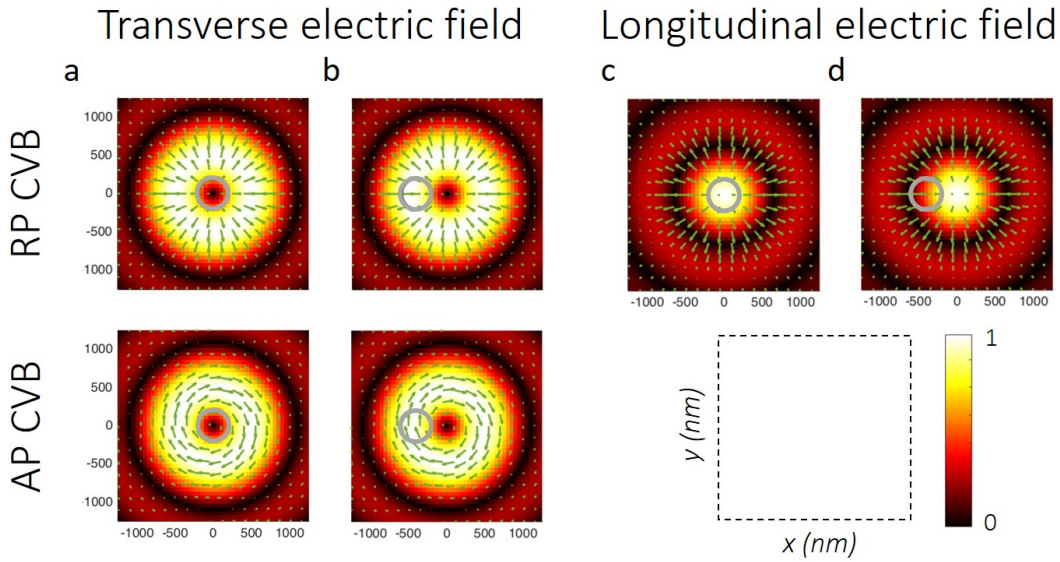

FIGURE 3.4: Calculated intensities of transverse and longitudinal electric components of a tightly focused RP and AP CVB. The green arrows indicate the transverse electric field components. (a,c) At the centre of the CVBs the transverse electric field components are null (see gray circles). (b, d) At an offset position (see *e.g.* gray circles at 500 nm from the centre), a local linear polarisation state is observed. In all the simulations, a beam with λ=1060 nm and propagating in air was focused by an objective lens with a NA of 0.8. In the calculations, nanometers units were considered and separated normalisation was performed, as depicted by the dotted square.

be observed in Figure 3.4, where a NA of 0.8 and a wavelength of 1060 nm was considered, in accordance to the experimental conditions.

A commercial polarisation converter (ARCoptix, S.A.) and a spatial filter were used to generate RP and AP CVBs from the LP femtosecond laser, details of the optical system can be found in Section 3.2.1. The intensity distribution of both CVBs was measured before focusing the beam on the sample, using a linear polariser and a beam camera. The polariser was rotated at three different angles and the expected cylindrical-symmetric polarisation patterns (radial and azimuthal) were verified, as shown in Figure 3.5. The non-uniform intensity distribution observed in both CVBs was attributed to a slight misalignment of the input beam with the CVB mode converter.

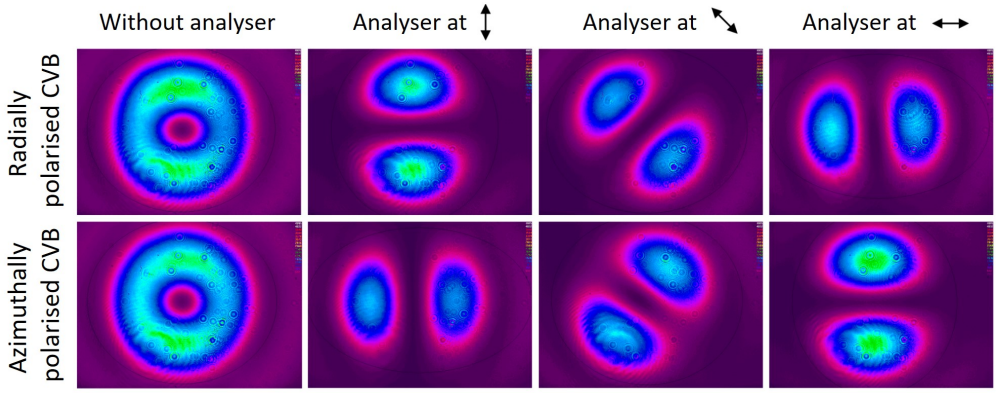

FIGURE 3.5: Transversal intensity distribution (a.u.) of the generated RP and AP CVBs, measured without and with a linear polariser (analyser) at different orientations. The images were acquired using a beam camera placed just before the microscope objective.

3.5 Scanning maps with CVBs

In this section, we present the results obtained from SHG and THG scanning maps of AlGaAs nanoantennas using CVB excitation. In general, second- and third-harmonic processes of the same material have different polarisation-dependence behaviours. These differences will be clearly observed from a single scan measurement when using CVB excitation. The nonlinear microscopy system described in Section 3.2.1 was used to perform the measurements. However, in this case the excitation beam is a CVB and an additional photomultiplier tube (PMT) was added to the microscopy system to implement simultaneous SHG and THG measurements, as shown in Figure 3.6. Details of the generated CVBs can be found in Section 3.4.

SHG and THG scanning maps were simultaneously acquired from the same AlGaAs nanoantennas, using RP and AP CVBs excitation. The experimental SHG and THG far-field scanning maps from AlGaAs nanoantennas with d=585 nm are shown in Figure 3.7a. As previously observed when using LP excitation, a high contrast between the nonlinear emissions from the nanoantennas and the substrate was observed in the scanning maps of Figure 3.7a, indicating the nanoantennas are the main sources of SHG and THG. The SHG scanning maps show a similar intensity distribution for both excitation beams: a four-lobe symmetric intensity

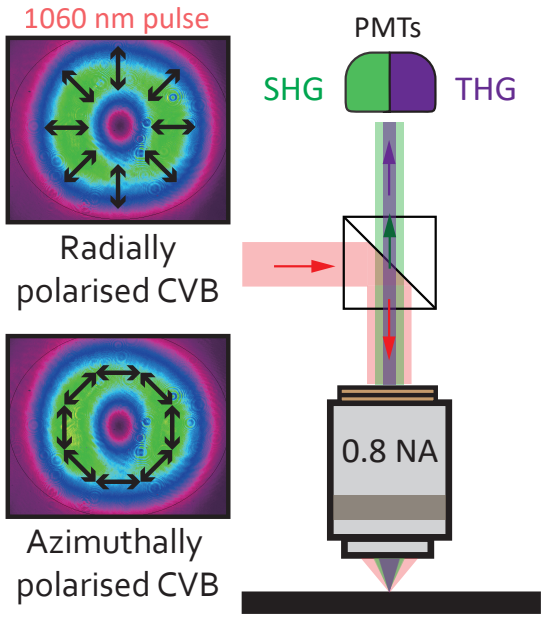

FIGURE 3.6: Schematic of the nonlinear microscopy experiment. The intensity profiles of the CVBs are shown in the left, together with their polarisation state indicated by black arrows. The fundamental CVB is focused on the AlGaAs nanoantennas by a microscope objective with a numerical aperture (NA) of 0.8. The reflected CVB and the nonlinear scattered emissions are collected with the same microscope objective. The fundamental beam is separated from the SHG and THG by a dichroic beamsplitter and bandpass filters. The photomultiplier tubes (PMTs) detect the SHG and THG.

pattern, indicating an anisotropic polarisation-dependent process from the AlGaAs nanoantennas. Likewise, the THG maps show similar intensity distribution for both excitation beams: a spatially symmetric doughnut-shaped intensity pattern, suggesting an isotropic and polarisation-independent process.

The THG intensity variations observed around the doughnut-shaped intensity pattern can be explained by several factors. First, the non-homogeneous intensity (I) of the fundamental beam (see Figure 3.5) scaled to the cube (I^3) for a third-harmonic process. Such non-homogeneity can become more pronounced in the case of the RP CVB, due to the π-phase plate used in the polarisation converter. Second, the difficulties to achieve a perfect alignment of the CVBs with the nanoantennas. In the SHG and THG scanning maps, the dark spot observed at the centre of the four-lobe and doughnut-shaped intensity patterns correspond

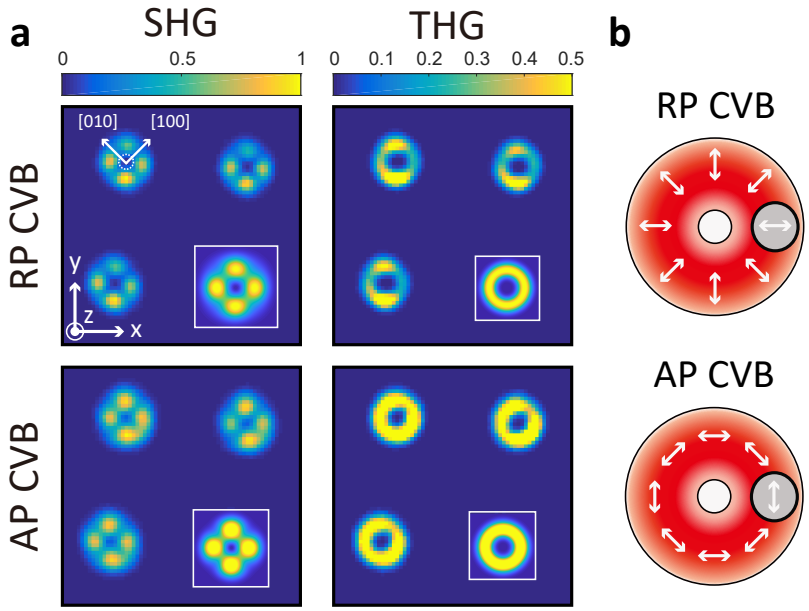

FIGURE 3.7: (a) Experimental far-field SHG and THG scanning maps from AlGaAs nanoantennas (d=585 nm) excited by RP and AP CVBs. The dotted circle shown in the SHG scanning map excited by a RP CVB, represents an AlGaAs nanoantenna together with its crystalline orientation. The maximum intensity (counts/ms) is observed in the SHG maps, as compared to the THG maps. Insets: MoM calculations of the far-field SHG and THG scanning maps using the corresponding CVB. Image size: 9.75 μm $\times$ 9.75 μm. (b) Representative cases showing the relative position of the nanoantennas with respect to the centre of the CVB. At this position (corresponding to certain pixels in the SHG and THG scanning maps), the nanoantenna is illuminated by the transversal electric field components of the corresponding CVB.

to the position where the centre of the CVB overlaps with the centre of the nanoantenna. At this particular position, the dark spot is explained by the lack of transverse electric field excitation (see Figure 3.4a) to generate either SHG or THG. As the nanoantenna is moved along the xy plane and away from the CVB centre, the transversal electric-field components of the corresponding CVB (see Figure 3.4b) become the dominant excitation field as depicted in Figure 3.7b, driving the corresponding harmonic generation in the nanoantenna.

Calculations of the SHG and THG in AlGaAs nanoantennas, performed using the MoM, are shown in the inset of Figure 3.7a. In the MoM a single AlGaAs disk embedded in a homogeneous medium (n = 1.44) was considered, with dimensions corresponding to those measured by scanning electron microscopy. Again, the SHG and THG scanning maps from

calculations agree with those from experiments, capturing the main features - a high contrast between the nonlinear emission from the nanoantenna and the substrate, a dark nonlinear emission at the centre of the intensity patterns, and a four-lobe or doughnut-shaped intensity patterns according to the order of the harmonic generated. With our nonlinear microscopy technique the anisotropic and isotropic behaviour of the SHG and THG processes respectively, was easily identified by observing at their intensity patterns.

Nonlinear polarisation-dependence studies have been previously used for crystal characterisation (*115*, *128*) and optical sensing (*129*, *130*) of nanostructures. In such studies, every measurement is performed using an input Gaussian beam whose linear polarisation states are rotated across the substrate-plane. In addition to the rotation of the LP beam, these studies usually require the acquisition of SHG or THG scanning maps to determine the nanostructure position accurately. In this thesis, we introduce a new technique to study the SHG and THG polarisation-dependence of nanoantennas using CVBs. The varying in-plane linear polarisation states of the CVBs act as the driving excitation field, enabling to determine the polarisation-dependence from a single scan measurement. Furthermore, with our technique, the crystalline orientation of AlGaAs nanoantennas is readily provided by a single SHG scanning map. As observed in Figure 3.7a, the minima of the SHG is aligned to the crystalline axis of the AlGaAs nanoantenna. In the case of a LP excitation, the spot-like intensity distribution obtained in the SHG scanning maps (see Figure 3.2) does not provide information about the crystalline orientation of the nanoantenna, even after several scans.

Additionally, the scanning maps obtained here can enable to study the contribution of transverse and longitudinal electric components in the SHG and THG. Similar dark nonlinear emissions were obtained at the centre of the SHG and THG intensity patterns, for either RP or AP CVB excitation (see Figure 3.7). However, at the centre of the tightly focused RP and AP CVBs, an important difference among the two beams is observed: the AP CVB exhibits null longitudinal components, while the RP CVB exhibits strong longitudinal components (see Figure 3.4). Therefore, the dark nonlinear emission obtained at the centre of the harmonic intensity patterns for both CVBs can indicate a weaker contribution of the longitudinal components, as compared to the transversal ones, in the generation of harmonics. Analysis of the

excitation beams components in the generation of harmonics is not possible when using a LP excitation, due to the spot-like intensity distribution obtained in the nonlinear scanning maps (see Figure 3.2).

The results in this section show the potential of the new optical technique to determine the crystalline orientation of semiconductor nanostructures through a single scanning measurement, using CVB excitation. By exploiting the spatially variant polarisation states of the CVBs and its relative location with respect to the nanoantennas, we were able to describe the SHG and THG polarisation-dependence and to directly determine the crystalline orientation of the nanoantennas through a single scanning map.

3.6 Polarisation analysis using nonlinear scanning maps

In addition to the general description of the SHG and THG polarisation-dependence given in the previous section, a more detailed study of the polarisation-dependence can be realised by performing a per-pixel analysis of the SHG and THG intensities. To illustrate this point, we analysed the harmonic intensities provided from the cross-lines traversing the SHG and THG scanning maps of a single nanoantenna represented by the orange lines in Figure 3.8a. Every cross line represents the excitation of the nanoantennas by a specific local linear polarisation state of the corresponding CVB (see Figure 3.8b). The pixel intensity of the SHG and THG maps overlapping with the cross-lines was integrated, normalised and plotted as a function of the CVB's local polarisation, as shown in Figure 3.8c. In this figure, every experimental point corresponds to an average of six scanning maps from single nanoantennas with nominally identical dimensions; this procedure reduce random errors produced by fabrication quality of the nanoantennas. Similar polarisation-dependence analysis can be performed by using the pixel intensities of circles surrounding the dark center spot.

In Figure 3.8c, the SHG intensity shows similar oscillating behaviour for both CVB excitations, with two maxima (at 0° and 90°) and two minima (at 45° and 135°). A non-oscillatory SHG behaviour is observed in the nanoantenna with d = 454 nm excited by an AP CVB, which was attributed to variations in the intensity of the CVB generated. The SHG minima and

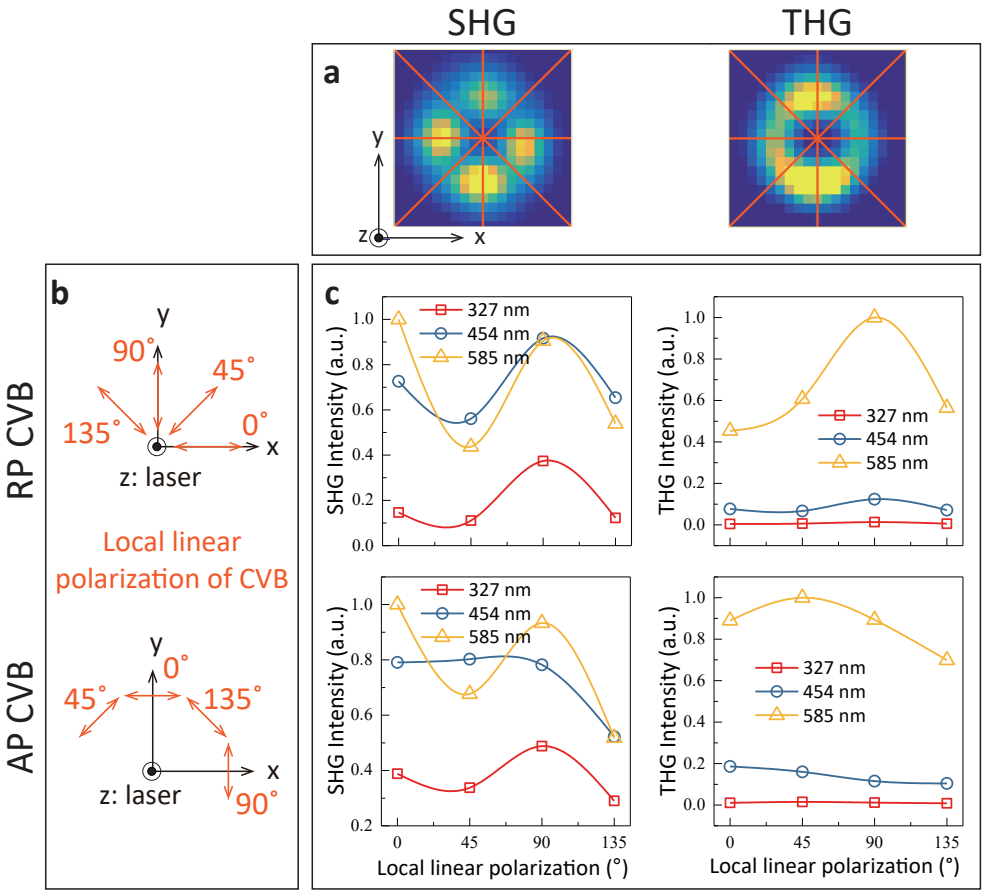

FIGURE 3.8: Analysis of experimental SHG and THG scanning maps. (a) SHG and THG scanning maps from individual AlGaAs nanoantennas with $d = 585$ nm, illuminated by a RP CVB. The cross-lines are indicated in orange colour. The image size is 2.7 $\mu m \times 2.7$ μm. (b) Local linear polarisation angles, with respect to the laboratory coordinate system, of RP and AP CVBs indicated by the orange arrows. (c) SHG and THG intensities of AlGaAs nanoantennas of different diameters (327, 454 and 585 nm), excited by the local linear polarisation of the corresponding CVB.

maxima correspond to the parallel and 45° local linear polarisations of the excitation beam, with respect to the crystalline axis, respectively. This behaviour originates from the specific properties of the second-order nonlinearity of the AlGaAs material, *i.e.*, to the only non-zero off-diagonal elements of the second-order AlGaAs susceptibility tensor. When the pump is polarised along 45° with respect to the crystalline axis, the projections of the pump field on both in-plane crystalline axes results in three non-trivial polarisation components of the SHG. As a result, the nonlinear polarisation induced will be larger than the one induced by a

pump polarised along the crystalline axes of the AlGaAs nanoantenna, where there is only one non-trivial polarisation component of the SHG (see Section 2.2).

To the best of our knowledge the study of THG in AlGaAs nanoantennas has not been widely studied before. While THG in AlGaAs nanoantennas has recently been observed (*108*, *114*), its properties have been generally ignored due to the large energy of the third-harmonic wave (above the AlGaAs band gap), falling within the strong absorption regime of the material. Therefore, important questions arise whether THG in AlGaAs nanoantennas is a resonant or an over-damped nonlinear phenomena. The THG scanning maps presented in this section have an intensity approximately one order of magnitude smaller than those of SHG. However, the optical and detection elements used in the optical system (see Section 3.2.1) were not calibrated for each harmonic wavelength, preventing the comparison among the intensities of both nonlinear processes. Therefore, only their polarisation-dependence behaviour could be compared with each other. In contrast to the oscillatory SHG intensities observed in Figure 3.8c, the THG intensities exhibit a fairly constant value across the different local linear polarisation states of the CVBs. This homogeneous behaviour is produced by the polarisation independence of the third-order nonlinear process in an AlGaAs material. A discrepancy with the expected THG homogeneous intensity is observed in the nanoantenna with d=585 nm, excited by a RP CVB. This discrepancy can be attributed to the non-uniform intensity of the CVB used in our experiment (see Figure 3.5).

The SHG and THG intensities observed in Figure 3.8c were found to be higher for some naonatennas as compared to others. In the case of SHG and for both CVBs excitation, a higher average intensity is observed for naonatennas with d=454 and 585 nm, as compared to a naonatenna with d=327 nm. In the case of THG excited either by a RP or an AP CVB, a higher average intensity is observed for a naonatenna with d=585 nm, as compared to nanoantennas with d=454 and 327 nm. The dependency of the SHG and THG average intensities with the diameter of the nanoantennas is indicative of a resonant condition.

SHG and THG scanning maps of single AlGaAs nanoantennas were calculated using the MoM. Cross-lines traversing the simulated scanning maps were used to analyse the polarisation behaviour of the SHG and THG, as done previously for the measured scanning maps (see

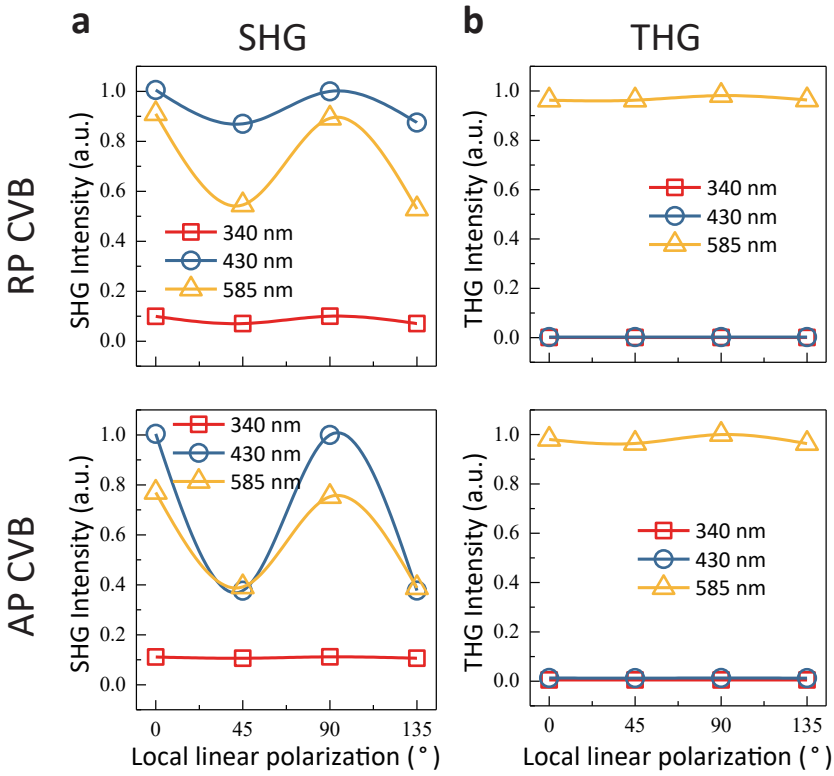

FIGURE 3.9: Analysis of calculated SHG and THG scanning maps. (a) SHG and (b) THG intensities of AlGaAs naonatennas with different diameters (d= 340, 430 and 585 nm) illuminated by the local linear polarisation of the corresponding CVB. For direct comparison, the intensities extracted from the calculated scanning maps correspond only to the angles shown in Figure 3.8.

Figure 3.8). For these calculations, comparable nanoantennas diameters as the ones measured before were used, and a diagonal third-order susceptibility tensor was assumed to simulate the THG. This assumption is valid for isotropic materials like AlGaAs whose crystalline structure is cubic. The obtained SHG and THG intensities were plotted as a function of the local polarisation of the CVBs, as shown in Figure 3.9. An oscillatory behaviour is observed in the SHG intensities, with two maxima and two minima, at the same positions as the ones observed in the corresponding measurements (see Figure 3.8c). The oscillatory behaviour is similar for both the AP and RP CVBs. In the case of the THG, the intensities remain constant across the different polarisation states of the CVBs, as previously observed in the corresponding measurements (see Figure 3.8c). The THG intensities for the two

CVBs are constant. Compared with their experimental counterparts (see Figure 3.8c), the calculated SHG and THG intensities shown in Figure 3.9 show the expected oscillatory or constant (according to the nonlinear process) behaviour for all the nanoantennas studied. We can therefore establish that the improvement of this characterisation technique requires the development of high quality light sources or high quality CVB converters, and careful alignment of the excitation beam with the nanostructure.

In Figure 3.9, a higher average SHG intensity is observed for nanoantennas with d=585 and 430 nm as compared to a nanoantenna with d=340 nm. Meanwhile, a higher average THG intensity is observed for a nanoantenna with d=585 nm as compared to the nanoantennas with d=430 and 340 nm. Similar behaviour was observed in the corresponding measurements of SHG and THG (see Figure 3.8c), strengthening the argument of the a resonant harmonic generation. In the next section, I will present several studies to further understand the resonant behaviour of AlGaAs nanoantennas.

The use of CVB in tandem with SHG and THG scanning maps can potentially simplify previously proposed crystallographic characterisation techniques, where SHG polarisation-dependence measurements are performed proving to be a reliable basis for non-invasive crystallographic characterisation of nanostructures (*115–119*).

3.7 Resonant harmonic generation

In this section, we use calculations to study the origin and characteristics of the resonant harmonic behaviour generated in AlGaAs nanoantennas. The calculations presented in this section were performed using the finite element method solver implemented in COMSOL Multiphysics. In the simulations, the AlGaAs disk nanoantennas were placed 500 nm away from the centre of the corresponding CVB, along the x direction. Throughout this section, the use of this particular illumination is referred as offset CVB excitation. As discussed earlier, the offset CVB excitation is the major contributor to the generation of harmonics. The field profiles of the CVBs in the paraxial region, *i.e.* before focusing, are obtained by considering a

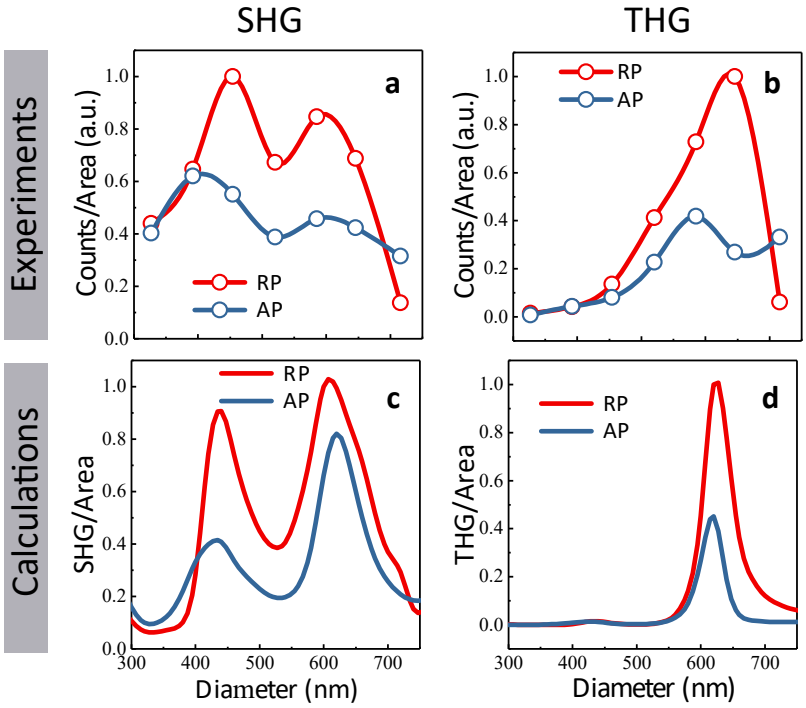

FIGURE 3.10: (a,b) Measured and (c,d) calculated backward SHG and THG of individual AlGaAs nanoantennas, as a function of its diameter. The experimental SHG and THG intensities were obtained by integrating the total intensity of the corresponding scanning map and normalising by the area of the nanoantenna. The calculated SHG and THG intensities were obtained by considering an offset CVB excitation. The beam is offset from the centre of the nanoantenna by 500 nm in the x direction.

Bessel-Gauss beam (*131*, *132*). After obtaining the field profiles, tightly-focused CVBs (*133*) with a wavelength of 1060 nm illuminate the AlGaAs nanoantennas in an offset excitation.

Experimental and calculated backward SHG and THG are shown in Figure 3.10, as a function of the nanoantenna diameter. The experimental SHG and THG emissions, shown in Figure 3.10a and b, were obtained by integrating the total number of counts of the corresponding scanning maps and normalising by the nanoantenna area. The calculated backward SHG and THG emissions, shown in Figure 3.10c and d, were obtained by considering offset RP and AP CVB excitation and normalising by the nanoantenna area. In the experiments, two resonant SHG peaks are observed around nanoantenna with d = 430 and 620 nm, as shown in Figure 3.10a. In contrast, a single THG resonant peak is experimentally observed around a nanoantenna with d = 620 nm, as shown in Figure 3.10b. Overall, the experiments show a

higher resonant harmonic emissions for a RP CVB excitation as compared to an AP CVB excitation. The corresponding calculations, shown in Figures 3.10c and d, are consistent with the experimental results, observing resonant peaks around the same positions and higher SHG and THG emissions for a RP excitation beam, as compared to an AP beam. The resonant harmonic generation processes in the AlGaAs nanoantenna are driven by the excitation of Mie resonances. A theoretical study of the electric and magnetic Mie resonances is performed and discussed in the following section.

3.7.1 Linear Multipolar Decomposition

When a nanoparticle is illuminated by a light beam, the dynamic charge current generated by the incident beam is distributed inside an area comparable to the effective wavelength (λ/n). This current might excite several multipoles that can contribute to the near and far-fields of the nanoparticle. To elucidate the linear optical response of AlGaAs nanoantennas and reveal the contribution of multipole modes, we performed calculations of their scattering spectrum using the spherical multipole expansion frame. The calculated fundamental scattering spectra of AlGaAs nanoantennas, excited by offset RP and AP CVBs, and its multipole decomposition are shown in Figure 3.11. In this figure, the decomposition of the total scattering spectra (see dotted lines) show the simultaneous contribution of electric and magnetic modes of different orders (dipole, quadrupole and octupole). Meanwhile for both offset CVB excitations, the total scattering (see black solid line) has two dips around the nanoantennas of interest with d = 430 and 620 nm. The reduced total scattering observed around a nanoantenna with d = 430 nm, coincides with a dip in the electric dipole (ED) mode. In turn, the reduced total scattering observed around a nanoantenna with d = 620 nm, coincides with a dip in the magnetic dipole (MD) mode. Thus, the ED and the MD are the main contributions to the reduced scattering spectra observed around the nanoantennas with d = 430 and 620 nm, respectively.

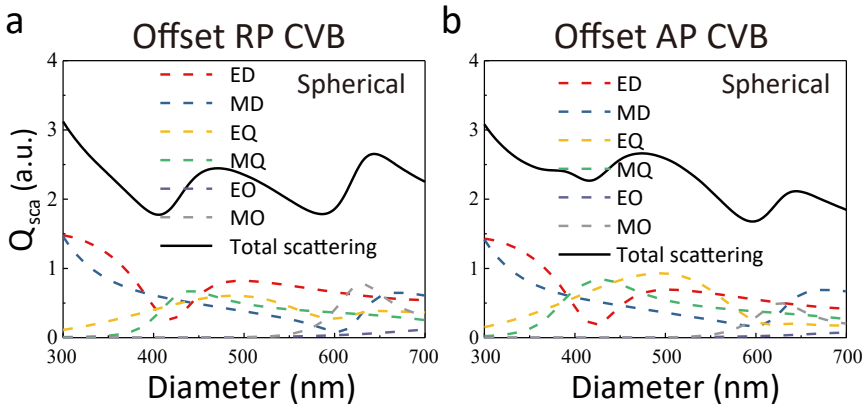

FIGURE 3.11: Calculated linear scattering of AlGaAs nanoantennas and its multipolar decomposition. The nanoantennas are excited by offset (a) RP and (b) AP CVBs with a wavelength of 1060 nm. The beam is offset by 500 nm in the x direction. The AlGaAs nanoantennas have diameters from 300 to 700 nm and fixed height of 300 nm.

3.7.2 Excitation of anapole-assisted modes

The reduced far-field scattering observed around a nanoantenna with d = 430 nm, can be induced by the simultaneous excitation of ED and a TD. When these two modes interfere with each other, mutual cancellation of their far-field scattering can arise (see Section 1.3.3.2). The simultaneous excitation of these two modes can not be studied in the frame of spherical multipole decomposition, since the radiation patterns of these two modes are indistinguishable from each other in this frame. Therefore, in the present section the multipole scattering decomposition is calculated in the frame of the cartesian expansion, where the ED and the TD modes can be separated. The calculated scattering spectra of TD and ED modes is shown in Figure 3.12a, where an overlap of the two modes is observed around a nanoantenna with d = 430 nm (see gray shading). The overlap of the ED and TD is known to induce an electric anapole condition, for which the linear far-field scattering is suppressed.

In a similar way, the reduced far-field scattering observed around a nanoantenna with d =6 20 nm (see Figure 3.11) can be induced by the simultaneous excitation of a MD and the mean radius (MR) distribution in the AlGaAs nanoantennas. These modes can not be separated in the frame of spherical multipole decomposition, but they are separated in the

Cartesian multipole expansion. The Cartesian MD is defined as (*134*, *135*):

$$\mathbf{m_{car}} = \frac{-i\pi c}{\lambda} \int \epsilon_0 (n^2 - n_0^2)(\mathbf{r} \times \mathbf{E}) d\mathbf{r}, \tag{3.5}$$

while the MR distribution is defined as:

$$\bar{\mathbf{R}}^{\mathbf{2}}_{\mathbf{m}} = \frac{-i\pi c}{10\lambda} \int \epsilon_0 (n^2 - n_0^2)(\mathbf{r} \times \mathbf{E}) r^2 d\mathbf{r}, \tag{3.6}$$

where c is the speed of light, λ is the wavelength of the incident field, ϵ_0 is the electric permittivity of vacuum, and **E** is the internal electric field.

The contribution of the Cartesian MD and the MR distribution to the scattering cross section can be calculated as

$$C_{sca}^{MD} = \frac{k_0^4 n^2 \mu_0}{6\pi\epsilon_0 |E_{inc}|^2} |\mathbf{m_{car}} - k^2 \bar{\mathbf{R}}^{\mathbf{2}}_{\mathbf{m}}|^2, \tag{3.7}$$

with k_0 and k being the wave number in free space and in the surrounding medium respectively, n_0 and n is the refractive index of free space and of the surrounding medium respectively, and μ_0 the magnetic permeability of vacuum (*135–137*). The MR contribution can be obtained as a third-order term of the expansion of the MD moment (*138*) and shares the same radiation pattern as the Cartesian MD. Thus, the MR and the Cartersian MD can destructively interfere with each other (*135*), cancelling their far-field scattering. Figure 3.12b shows the calculated scattering spectra of the MR and the Cartesian MD. Spatial overlap of the two modes is observed around a nanoantenna with *d* = 620 nm (see gray shading), canceling out the far-field scattering of each mode and leading to a magnetic anapole condition.

The anapole state is known to generate strong near-fields in nanoantennas (see Section 1.3.3.2). Thus, enhancement of the internal fields around the nanoantennas excited by either an electric or magnetic anapole condition is expected. To corroborate the near field-enhancement, the electric energy density inside the AlGaAs nanoantennas was calculated as shown in Figure 3.12c. The offset CVB excitation of the nanoantennas produces two main peaks of energy density around the nanoantennas with *d*=430 and 620 nm (see gray shading). The position of the energy density peaks coincide with the minimised far-field scattering observed in Figure 3.11. The minimised far-field scattering together with the maximum near-field

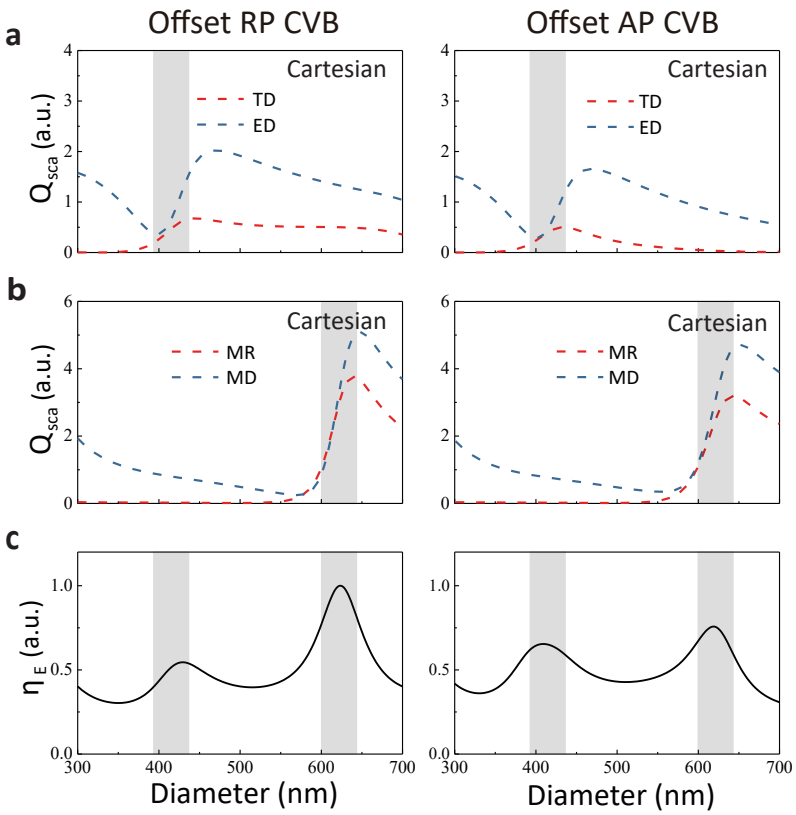

FIGURE 3.12: Calculation of the linear scattering of AlGaAs nanoantenna performed in the Cartesian multipole expansion, (a) Cartesian electric and toroidal dipole modes excitations, (b) Cartesian magnetic dipole mode and mean radius distribution. (c) Calculated electric energy density as a function of the diameter of the nanoantennas. In the simulations, the AlGaAs nanoantennas are excited by offset RP and AP CVBs at an excitation wavelength of 1060 nm. The beam is offset by 500 nm in the x direction.

observed around the nanoantennas with d = 430 and 620 nm corroborates the excitation of electric and magnetic anapole conditions, respectively.

The electric and magnetic anapole conditions are however not the only ones governing the near-field distribution of the nanoantennas with d = 430 nm and d = 620 nm. The presence of higher order multipoles including magnetic dipole (MD), electric quadrupole (EQ), magnetic quadrupole (MQ) and magnetic octupole (MO) can also contribute to the

near-field enhancement (see Figure 3.11) of the nanoantennas. As a consequence, an electric-anapole-assisted mode is excited around a nanoantenna with d=430 nm , while a magnetic-anapole-assisted mode is excited around a nanoantenna with d=620 nm. The enhanced near-field distributions originated by anapole-assisted multipole effects have reported increment of nonlinear conversion efficiencies (*52*, *139–142*).

3.7.3 Distribution of near and far-fields

Calculations of the total SHG and THG intensities and its multipolar decomposition are shown in Figure 3.13. The intensities were calculated as a function of the nanoantenna's diameter by considering offset CVB excitation. The calculations show two peaks of enhancement, around the nanoantennas with d = 430 and 620 nm, originated by the electric and magnetic anapole-assisted states, respectively (see Section 3.7.2). Figure 3.13 shows the contribution of several multipolar components to the resonant SHG and THG. The dominant contribution of a specific multipole was not observed in either of the harmonic processes.

Compared to the AP CVB excitation, the RP CVB excitation gives higher conversion efficiencies in the total SHG and THG, in agreement with previous calculations of the backward SHG and THG (see Figures 3.10c and d). The relative intensities of the two SHG peaks shown in the left-hand panels of Figure 3.13 are different from the ones shown in Figure 3.10c. Meanwhile, the THG intensity shown in the right-hand panels of Figure 3.13 is characterised by two peaks of enhancement, differently from the single THG peak observed in Figure 3.10d. The differences observed in Figures 3.13 and 3.10 can be explained by the directionality of the SHG and THG. Strong directionality of the harmonics generated, either in the backward or forward direction, induces different behaviour of the backward/forward harmonic emissions as compared to the total emissions.

The SHG and THG far-field radiations patterns of AlGaAs nanoantennas were calculated, considering RP and AP CVBs excitation, as shown in Figure 3.14. Two diameters of nanoantennas were considered, d = 430 and 620 nm, where the generation of harmonics is driven by anapole-assisted states. The SHG far-field radiations patterns of both nanoantennas are

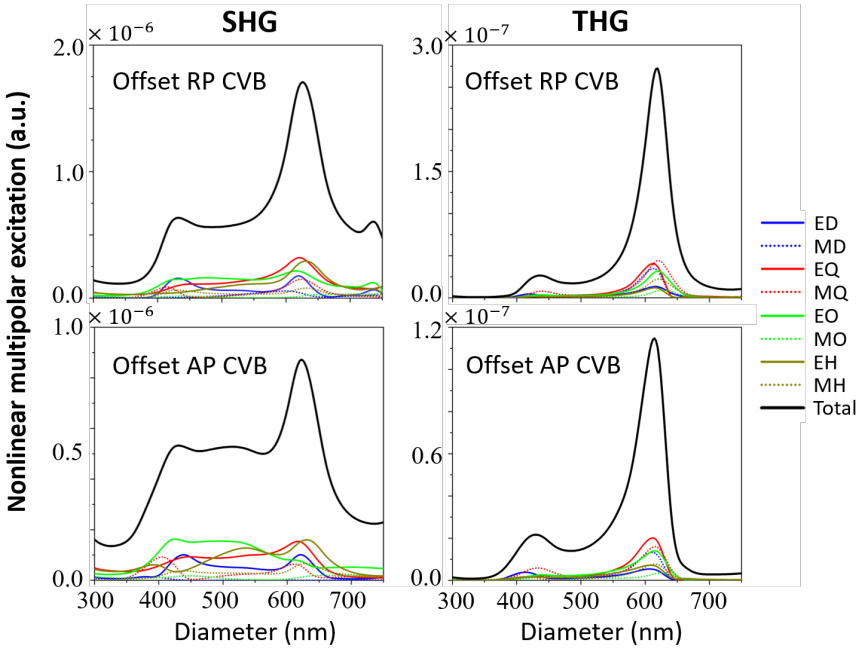

FIGURE 3.13: Calculations of the total SHG and THG intensities and its multipolar decomposition, as a function of AlGaAs nanoantennas diameter. The nanoantennas are excited by offset RP and AP CVBs. The CVBs are offset by 500 nm in the x direction.

characterised by broad angles of emission in both, backward and forward directions. In every case, the emission angles of the backward SHG dictate the relative intensities of the peaks observed in Figure 3.10c. In contrast, the THG far-field radiation patterns of both nanoantennas reveal strong forward directionality, leading to a low backward THG. In particular for the nanoantenna with d = 430 nm, the weak backward THG is emitted at broad angles; therefore it is not captured by our experimental setup which only collects radiation emitted at smaller angles than $\approx 53^{\circ}$ (corresponding to a NA of 0.8). This explains the lack of a significant peak in the backward THG, around the nanoantenna with d = 430 nm (see Figure 3.10d). The strong forward directionality of the THG is explained by the constructive interference of the nonlinearly generated multipoles, in the direction forward. Also this characteristic of the THG, indicates the absorption of the material at this frequency does not over-damp the resonant behaviour of the nonlinear process. This observation resolves some of the issues raised in Ref. (*110*) regarding the strong absorption at harmonic frequencies.

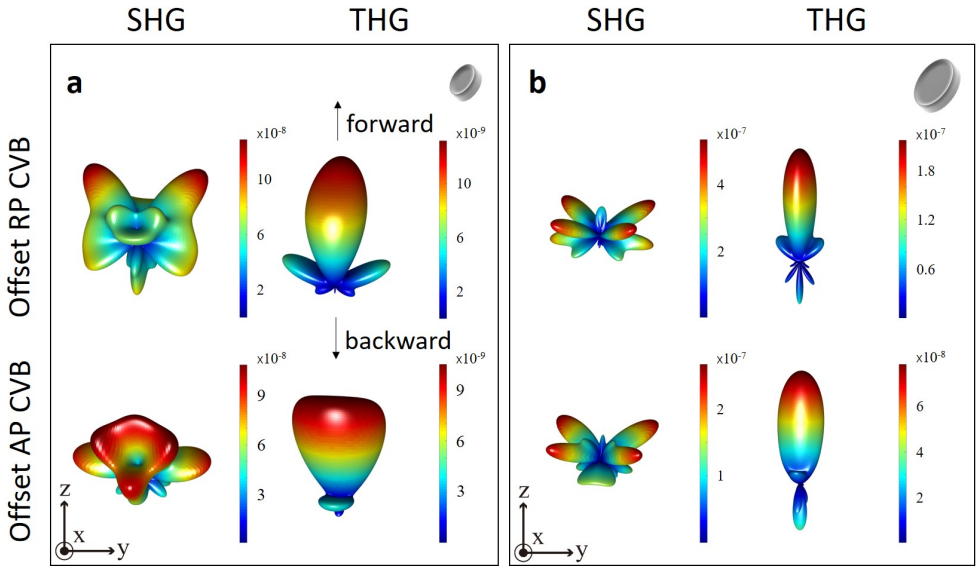

FIGURE 3.14: Calculated SHG and THG far-field emission patterns from an AlGaAs nanoantenna with (a) $d = 430$ nm and (b) $d = 620$ nm. The nanoantenna is excited by an offset RP and AP CVB with a wavelength of 1060 nm. The beam is offset by 500 nm in the x direction.

As discussed earlier in Figure 3.10, higher backward SHG and THG are observed around the resonant nanoantennas excited by an offset RP CVB rather than with an offset AP CVB. The same behaviour was observed in the calculated total SHG and THG (see Figures 3.13 and 3.14). This behaviour is not only observed in the far-field, but it is also observed in the fundamental and harmonic near-field distributions of a resonant nanoantenna (d = 620 nm), as shown in Figure 3.15. This was attributed to the different electric and magnetic multipolar components of an offset RP and AP CVB (*143*). However, a complete understanding of this phenomenon requires further studies that are beyond the scope of this thesis.

Our results has demonstrated the enhancement of the harmonic fields originated by the excitation of anapole-assisted states of electric and magnetic character. The collection efficiencies of the harmonic far-fields are highly dependent on the directionality of the harmonic fields.

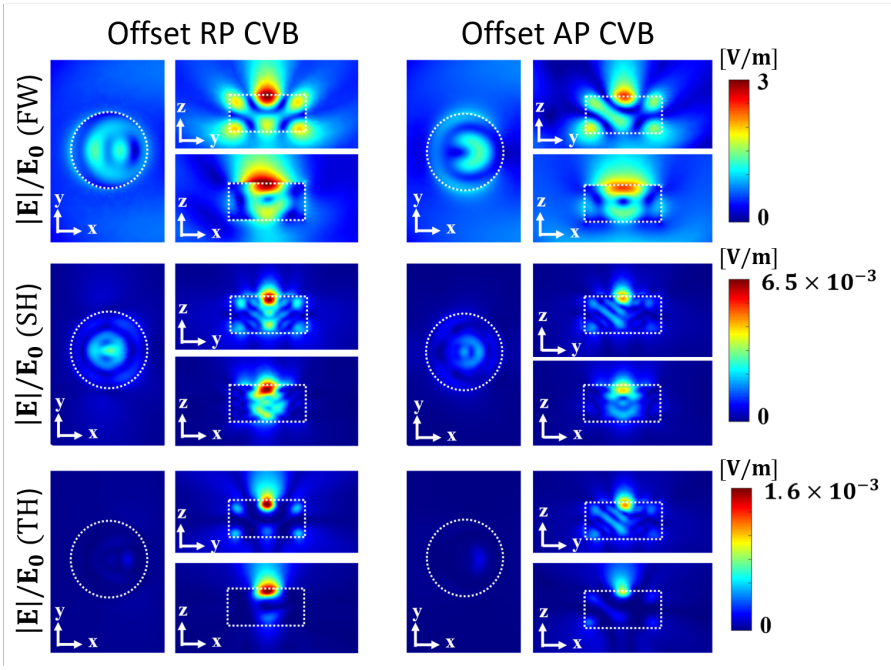

FIGURE 3.15: Calculated electric near-field distributions at the fundamental wavelength (FW), second-harmonic (SH), and third-harmonic (TH) emissions of an AlGaAs nanoantenna with d= 620 nm excited by an offset RP and AP CVB. The beam is offset by 500 nm in the x direction.

3.8 Conclusions

We have applied a new nonlinear microscopy technique to determine the crystalline orientation of individual AlGaAs nanoantennas. Our technique is based on SHG and THG microscopy with RP and AP CVBs. The symmetric SHG scanning maps display four-lobe intensity patterns, where the intensity minima are aligned with the crystalline axes of the material. THG scanning maps were also obtained, the maps show uniform doughnut-shaped intensity patterns. The nonlinear microscopy technique is only limited by the homogeneity and fine alignment of the incident CVBs.

The study of SHG and THG as a function of the nanoantenna's diameter proved the generation of resonantly enhanced harmonic processes, driven by the presence of electric- and magnetic-anapole assisted states excited by offset CVBs. The agreement between experimental results and calculations indicates the generated harmonics are dominated by the bulk response of the material. In the anapole assisted states, the fundamental near-fields are strongly enhanced

while the fundamental far-fields are suppressed. More importantly, the resonant behaviour of the harmonics generated is preserved despite the strong absorption of the material at the second- and third-harmonic frequencies, even though the resonances correspond to bulk-type excitations.

CHAPTER 4

Study of SHG in (100)-AlGaAs nanoantennas probed by LP beams

4.1 Introduction

In the previous chapter, CVBs were used to excite SHG and THG in AlGaAs nanoantennas. The studies performed demonstrated that the main sources in the generation of harmonic emissions are the transverse electric field components of the CVBs. It is well known that LP beams have strong transverse electric field components. In this chapter, LP beams are used to study the properties of SHG in individual AlGaAs nanoantennas. The possibility to shape the radiation pattern and polarisation state of the SHG in the forward and backward direction is demonstrated, together with a high SHG conversion efficiency (*144*). A complex polarisation spatial distribution of the SHG is shown, which can lead to the generation of a nonlinear cylindrical vector beam, radially polarised. In addition, nonlinear optical magnetism in AlGaAs nanoantennas is discussed (*145*). The continuous transition between electric and magnetic nonlinearities is shown, achieved by tuning the polarisation angle of the LP fundamental beam.

4.2 Linear scattering of AlGaAs nanoantennas

AlGaAs nanoantennas of different diameters (d), fixed height of 300 nm, and periodicity of 5 μm were fabricated along the (100) crystal axis, following the procedure explained in Section 2.4. The linear extinction spectra of the individual AlGaAs nanoantennas were measured using a white-light source illumination (see Figure 4.1a). The incoming white-light was focused by an air objective lens with a NA of 0.85 onto the AlGaAs nanoantennas (sitting

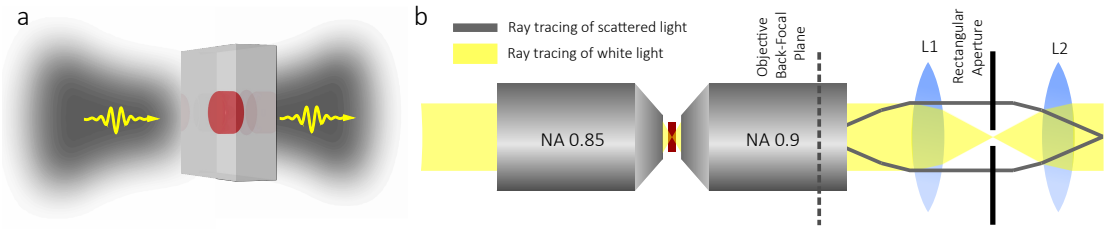

FIGURE 4.1: (a) Schematic of linear scattering of single nanoantenna illuminated by a white-light source. (b) Schematic of optical system used to measure the linear extinction spectrum of a nanoantenna. The scattered light, focused at the objective back-focal plane, is being collected by a lens (L1) and filtered out from the system by a rectangular aperture. Consequently, only the transmitted white light is collected by the second lens (L2).

on a glass substrate), and precisely positioned within the focal plane of the objective by a 3D piezo-stage. A second air objective lens with a NA of 0.9 was used to collect the transmitted white-light and the forward scattering of the nanoantennas. By placing a rectangular knife-edge aperture at the focus of two confocal lenses, as depicted in Figure 4.1b, the forward scattering light was filtered out from the optical system. Therefore, only the transmitted light was coupled to a multimode optical fiber and detected by two spectrometers: an Ocean Optics 65000 to measure the visible spectrum and a Princeton Instruments Acton SP 2300 monochromator with Andor DU490A-1.7 InGaAs array detector to measure the near-infrared spectrum. Through the measured spectra, the extinction cross-sections was obtained using the approximate relation

$$\begin{aligned} C_{ext} &\propto -ln(T) \\ &\approx 1 - T, \end{aligned} \tag{4.1}$$

where T is the transmission spectrum obtained through the following expression:

$$T = \frac{S_{sample} - S_{background}}{S_{reference} - S_{background}}. \tag{4.2}$$

S_{sample} refers to the transmission spectrum from the nanoantennas, $S_{background}$ refers to the transmission spectrum from the background and $S_{reference}$ refers to the transmission spectrum from the glass substrate.

The measured extinction spectra of individual nanoantennas with different diameters are shown in Figure 4.2a, as a function of the incident wavelength. The different colours correspond to the different diameters of the nanoantennas, while the two vertical dashed lines correspond to the spectral position of the fundamental wavelength (FW) and second-harmonic wavelength. The gray region indicates the spectral range not covered by any of the two spectrometers used in the experiments. As observed in the extinction spectra, several sharp resonances are excited around the second-harmonic wavelength. In contrast, a single and broad resonance is excited around the FW, which is red-shifted as the diameter of the nanoantennas is increased. The maximun of the FW resonance occurs in the nanoantennas with diameters from 490 to 570 nm. Calculations of the extinction spectra, shown in Figure 4.2b, were performed using the rigorous-coupled wave analysis (RCWA) method (*146*). In the simulations, the geometrical parameters considered for the AlGaAs nanoantennas correspond to the ones of the fabricated nanoantennas. As shown in Figure 4.2, the numerical calculations performed agree with the measured spectra. The small discrepancies observed between experiments and calculations were attributed to fabrication imperfections and the finite NA of the experimental system.

The contribution of the multipole modes to the total extinction is calculated using multipole expansion analysis. The linear extinction and its multipolar decomposition are calculated at the FW as shown in Figure 4.3, using the polarisation currents induced inside the nanoantennas. The solid and dashed lines in Figure 4.3 indicate the numerical simulations while the blue dots indicate the experimental results extracted from Figure 4.2. According to the multipole expansion, the total scattering (black solid line) is mainly described by the contribution of an ED and MD mode. The contribution of the EQ and MQ modes becomes noticeable when the diameter of the nanoantennas is increased. The experimental and calculated total scattering (or extinction) reveal a resonant profile which is maximal around the diameters in the range of 450 to 550 nm. This resonant condition is achieved when the amplitude of the ED and MD are equal to each other. In other words, the highest extinction is observed when the ED and MD modes excited inside the nanoantennas satisfy the first Kerker condition (*147*).

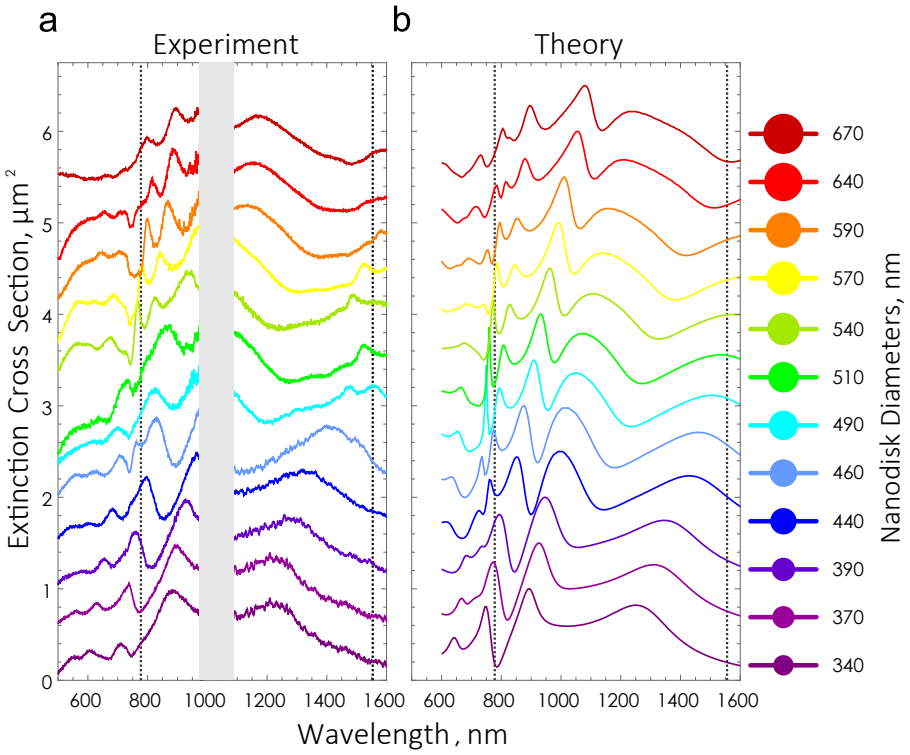

FIGURE 4.2: (a) Measured and (b) calculated extinction spectra of AlGaAs nanoantennas. The different colours correspond to different diameters of the nanoantennas, as indicated in the right side of the plots. The dashed lines mark the spectral positions of the fundamental and the second-harmonic wavelengths.

4.3 Nonlinear scattering of AlGaAs nanoantennas

When an AlGaAs nanoantenna is excited at the fundamental wavelength, second-harmonic emission is generated in both backward and forward directions. The transparent and homogeneous surrounding environment of our fabricated AlGaAs nanoantennas (see Section 2.4), enable us to measure the properties of the SHG in both directions. Thus, in this chapter the properties of the backward and forward SHG were investigated as a function of the naoantennas diameter, under the excitation of a LP beam.

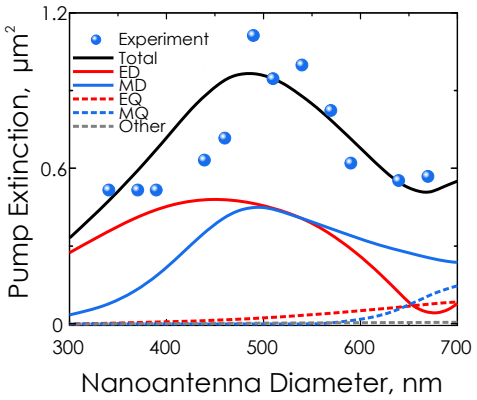

FIGURE 4.3: Linear extinction of AlGaAs nanoantenna and its multipolar decomposition, as a function of the nanoantenna diameter. The black solid line is obtained from calculations while the dots are obtained from experiments, both at the pump wavelength of 1550 nm. Coloured lines indicate the multipolar contributions to the total extinction.

4.3.1 Optical system

The AlGaAs nanoantennas were excited by a pulsed Er^{3+}-doped fiber laser (PriTel, Optical Fiber Amplifier HPFA-18-10-FS duration pulse of ≈500 fs, repetition rate of 5 MHz) operating at a central wavelength of 1550 nm. At the output of the LP laser beam, a zero-order (operating wavelength of 1550 nm) half-wave plate was used to rotate the polarisation state of the fundamental beam. Using a confocal configuration consisting of two air objectives, the nanoantenna backward and forward SHG were studied as explained below. The fundamental beam was focused on various nanoantennas by an infrared objective (Olympus LCPlanNIR, $100\times$ and NA of 0.85). The nanoantennas were placed within the focal plane of the infrared objective by a 3D piezo-stage. The transmitted fundamental beam and the forward SHG were collected by a visible objective (Olympus MPlanFLN, $100\times$ and NA of 0.9). The nanoantennas face the infrared objective, while the glass substrate faces the visible objective. At the back aperture of the visible objective lens, a shortpass and a bandpass filter were used to block the transmitted fundamental beam, thereby only the SHG was detected by a cooled CCD camera (StarlightXpress SXV-H9). The camera was aligned to a lens (f=100 mm), to capture the light from a collimated beam and focus it on the camera detector. In the backward direction, a dichroic mirror and a bandpass filter were used at the back aperture of the infrared

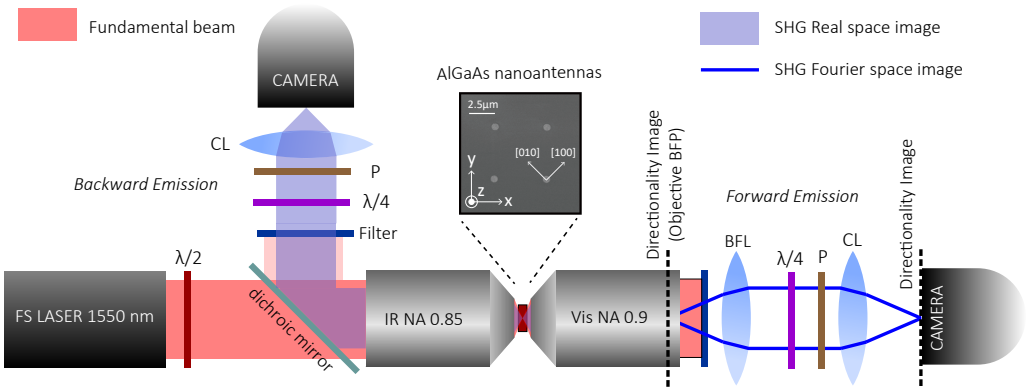

FIGURE 4.4: Schematic of experimental setup used to study the backward and forward SHG from AlGaAs nanoantennas using different optical components such as (λ/2) half-wave plate, (BFL) back focal lens, (λ/4) quarter-wave plate, (P) polariser and (CL) camera lens. A scanning electron microscopy of the AlGaAs nanoantennas with its crystalline orientation is also shown.

objective lens to direct the backward SHG onto a CCD camera (StarlightXpress SXVR-H9) and block the reflected fundamental beam. The camera was aligned to a lens with a focal distance of f=150 mm. The high NA of the infrared and visible objectives allowed large angular collection efficiencies of 58° and 64°, respectively. These collection angles are given by NA=$n\sin\theta$, where n is the refractive index of the surrounding media (assuming air, n=1) and θ is the collection angle. The fabricated nanoantennas were however, partially embedded in a 4 μm BCB layer ($n\approx$1.4), reducing the angular collection in the forward direction. The size of the fundamental beam at its focus was measured using the knife-edge method to ensure that the beam is close to its diffraction limit of 2.2 μm.

Second-harmonic directionality. The directionality of the SHG can be visualised by its 3D far-field radiation pattern. Experimentally, the 3D radiation pattern is captured by an objective lens and projected in its back-focal-plane (BFP) as a 2D radiation pattern. The method described is known as BFP imaging, which enables to measure the emission angles of a scattering object through the use of lenses, as it is know from the Fourier theory (see Section A3). Thus, by imaging the BFP of the visible and infrared objective lens, the forward and backward SHG radiation patterns were obtained. The forward BFP images of the SHG were built by adding a lens (f=75 mm) at 75 mm of the BFP of the visible objective lens (see forward emission in Figure 4.4). Similarly, backward BFP images of the SHG were built by

adding a lens (f=100 mm) at 100 mm of the BFP of the infrared objective lens (not shown in Figure 4.4). Through these configurations, the BFP of each objective lens is projected onto the imaging camera. Appropriate filters were used in each case to filter out the transmitted and reflected fundamental beam and measure only the SHG. A third removable lens is added in each direction (forward and backward) to switch the camera images from the real space to the Fourier space (or BFP).

Polarisation states analysis. According to the Stokes vector formalism, a complete description of the polarisation state of an optical signal can be obtained by measuring the polarisation of the signal through six polarisation bases (see Section A2). The six polarisation bases are: horizontal, vertical and two diagonal linear polarisations together with right-hand and left-hand circular polarisations. In the study presented in this chapter, a quarter-wave plate and a linear polariser with different angular positions were used to obtain the six polarisation bases of the SHG. The angular positions required, in the linear polariser and the quarter-wave plate, to measure each of the six polarisation bases are described in Section 4.3.3. In the experiments, the quarter-wave plate and the linear polariser were controlled by two servo motorised rotation mounts and a Labview program to facilitate the sequential measurements.

4.3.2 Second harmonic generation (SHG) efficiency

In the experiments, a LP beam was used as the pump beam to excite AlGaAs nanoantennas. According to the results obtained in the previous chapter (see Section 3.5), the polarisation of the pump beam was set at 45° of the nanoantennas crystalline axes (see Figure 4.4) to maximise the SHG conversion efficiency. The pump beam, with an average power of $\approx$ 1 mW, was focused by an infrared objective lens to a diffraction-limited spot of 2.2 μm, resulting in a peak intensity of $\approx$ 7 GW/cm^2. The AlGaAs nanoantennas are fabricated on/embedded in a transparent medium, thus the visible and infrared objective lens can be used to collect the forward and backward SHG (Figure 4.5a.). Due to the finite NA of the objective lenses, only a small portion of the total SHG is collected. The SHG is detected by two CCD cameras previously calibrated using a power meter, while the average power of the fundamental beam was directly measured. The SHG efficiency was obtained according

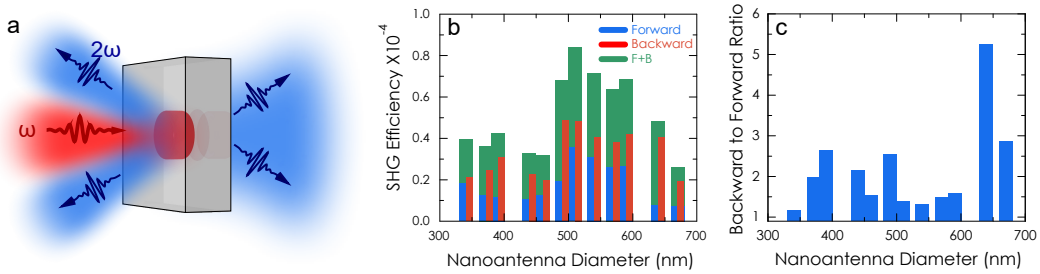

FIGURE 4.5: Nonlinear spectroscopy of single nanoantennas. (a) Schematic of single nanoantenna experiment. (b) Measured SHG efficiency (P_{SHG}/P_{FW}) from single nanoantennas of different diameters, at a pump wavelength of 1550 nm. Blue indicates forward radiation, red indicates backward radiation, and green indicates the sum of both radiations. (c) Backward-to-forward ratio of the SHG as a function of the nanoantenna diameter.

to $\eta = P_{SHG}/P_{FW}$, where P_{SHG} is the average power of the SHG and P_{FW} is the average power of the fundamental beam impinging in the cross section of the nanoantennas. The measured SHG efficiency is shown in Figure 4.5b, as a function of the nanoantenna diameter. The total SHG efficiency, shown by the green bars, was obtained by summing the forward and backward SHG. The SHG efficiency exhibits a maximum around a nanoantenna with d = 500 nm, and lower efficiencies for the smallest and largest diameters studied. A similar trend is observed in the linear extinction measured at the FW (see Figure 4.3). The similarities observed between both profiles indicate the SHG conversion efficiency is mainly driven by the extinction of the fundamental field. The resonant behaviour of higher-order modes excited at the second-harmonic wavelength (see dotted line in Figure 4.2), can also contribute to the SHG enhancement. The highest SHG collection efficiency, equal to $8.5\times\ 10^{-5}$, is observed in a nanoantenna with d = 490 nm. The backward to forward SHG can be tailored by changing the nanoantenna diameter, as shown in Figure 4.5c. For example, around a nanoantenna with d = 400 nm the SHG is mostly directed in the backward direction; while for nanoantennas diameters in the range of 500 to 600 nm, the backward and forward SHG similarly contribute to the total SHG. At larger nanoantenna diameters, where higher order multipoles are excited, the backward to forward ratio peaks again. As shown in Figure 4.5c, in all the nanoantennas studied the backward to forward ratio of the SHG is greater than unity. Thus, the backward SHG dominates over the forward SHG in all the AlGaAs nanoantennas studied.

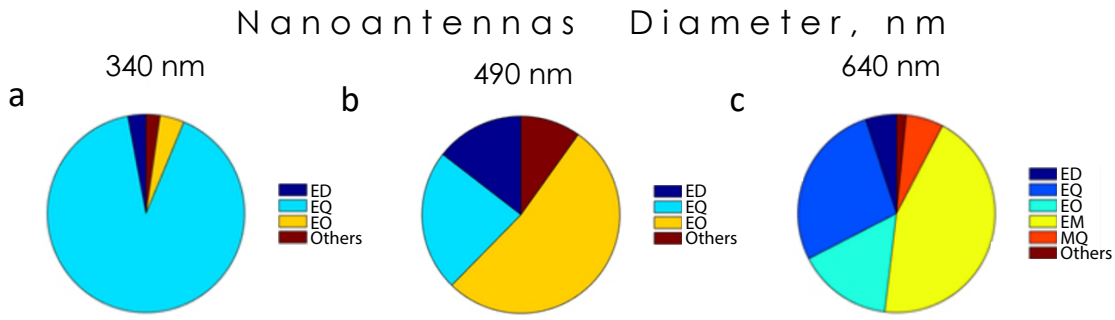

FIGURE 4.6: Chart diagrams showing the SHG multipolar contributions. The multipolar contributions are calculated for three nanoantennas with diameters of (a) 340, (b) 490, and (c) 640 nm.

The SHG efficiency (Figure 4.5b) and their backward to forward ratio (Figure 4.5c) are both sensitive to the diameter of the nanoantennas. In particular, the nanoantenna diameter can be tuned to achieve high efficiency together with comparable backward-to-forward ratio (see *e.g.* nanoantenna with $d = 490$ nm). The possibility to tune other geometrical parameters can be explored to achieve high efficiency and unidirectional SHG, simultaneously.

The SHG efficiency is strongly influenced by the extinction of the fundamental field, while the SHG directionality is strongly influenced by the mutual interference of the modes generated at the second-harmonic field. To show the contribution of different modes to the SHG, multipolar decomposition of the second-harmonic field was performed for three nanoantennas, as shown in Figure 4.6. The multipolar decomposition was performed using COMSOL Multiphysics, the details of these simulations will be discussed in the next section. According to the multipolar analysis, the major contribution to the SHG is provided by the electric modes of different order, while the contribution of magnetic modes is only observed in nanoantennas with large diameters (see *e.g.* nanoantenna with $d = 640$ nm in Figure 4.6). The number of modes generated at the second-harmonic field increases with the diameter of the nanoantennas.

In this section, we have discussed different parameters that influence the SHG efficiency and its directionality. The spatial overlap between the fundamental and second-harmonic modes, and its influence in the SHG efficiency was not discussed here.

4.3.3 Directionality and polarisation distribution of SHG

The far-field emission and polarisation state of the SHG were simulated using the finite element method solver in COMSOL Multiphysics. In the simulations, the disk nanoantenna is embedded into a homogeneous medium with a refractive index of 1.44, equivalent to the one of the glass substrate and the BCB layer used during the fabrication of the nanoantenna. The material dispersion of the AlGaAs material was taken from COMSOL tabulated data. A value of 100 pm/V was considered for the bulk second-order susceptibility tensor $\chi^{(2)}$, according to zinc blende AlGaAs material. The components of the second- and third-order susceptibility tensor can be seen in Section 2.1. An undepleted excitation field was assumed and two coupled steps were used to calculate the nonlinear emissions (*50*, *106*). First, we simulate the linear extinction of a disk nanoantenna excited by a focused monochromatic Gaussian beam polarised along the (110) direction, in accordance with the experimental conditions. The bulk nonlinear polarisation $P_i^{2\omega}$ induced inside the nanoantenna is then employed as a source for the next electromagnetic simulation, where the nonlinear emission is obtained. Finally, the far-field nonlinear emission is employed to obtain the multipole contributions of the second-harmonic emission, based on the Mie theory (*148*).

The 3D SHG far-field radiation pattern of a nanoantenna with d = 490 nm, which is the one with the highest efficiency observed, is shown in Figure 4.7a. The SHG far-field shows mainly, an electric octupole emission characterised by six-lobbed radiation with null intensity along the z-axis direction. Other nonlinear modes such as an EQ and ED are generated inside the nanoantenna (see Figure 4.6 with d = 490 nm), leading to low forward SHG due to its mutual interference. A projection of the SHG far-field radiation pattern in the xz plane is shown in Figure 4.7b. The forward and backward experimental collection angles, limited by the NA of the objective lenses, are indicated by gray shaded areas. Projections of the upper (forward emission) and lower (backward emission) half-space of the 3D radiation pattern, across the xy plane, are shown in Figures 4.7c and d, respectively. The projections constitute the 2D radiation patterns of the SHG. Two circles are shown in every radiation pattern, the black outer circle delimits the total SHG (see NA of 1.44 in Figure 4.7b), while the gray inner circle delimits the collected SHG (see NA of 0.9 and 0.85 in Figure 4.7b). The portion

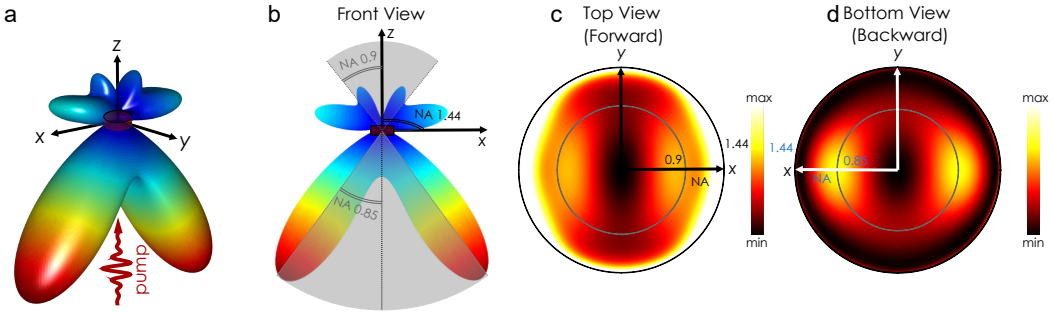

FIGURE 4.7: SHG far-filed emission of a nanoantenna with a d=490 nm. (a) Calculated 3D SH far-field pattern. (b) Front view of the pattern. Cones indicate the range of angles experimentally accessible with our high-NA objective lens. (c,d) Top and bottom view of the SHG radiation pattern. The inner gray circles indicate the maximum experimental collection angle.

of the collected SHG can be estimated by integrating the total (outer circle) and collected (inner circle) SHG and comparing them. According to our estimations about 30% of the total SHG is collected in the experiments, thus the SHG conversion efficiency reported before (see Figure 4.5) is about three times larger.

The SHG angular distribution and polarisation state of the most efficient nanoantenna, with d = 490 nm, were measured using BFP imaging and the Stokes formalism, respectively. BFP imaging is an optical technique used to measure the angular distribution of an scattering object (see Section A3), while the Stokes formalism allows to completely describe the polarisation state of an optical signal (see Section A2). In the optical system, BFP images of the SHG were built in the backward and forward direction by adding a lens in each direction. A quarter wave-plate and a linear polariser were also added to measure the polarisation state of the SHG (see Section 4.3.1).

The SHG BFP images of six ongoing polarisation bases are shown in Figure 4.8. The SHG BFP images were taken in the backward direction from a nanoantenna with d = 490 nm, by setting the quarter wave plate and the linear polariser at a pair of angles (α, β). Considering the quarter wave plate at an angular position α and the linear polariser at angular position β,

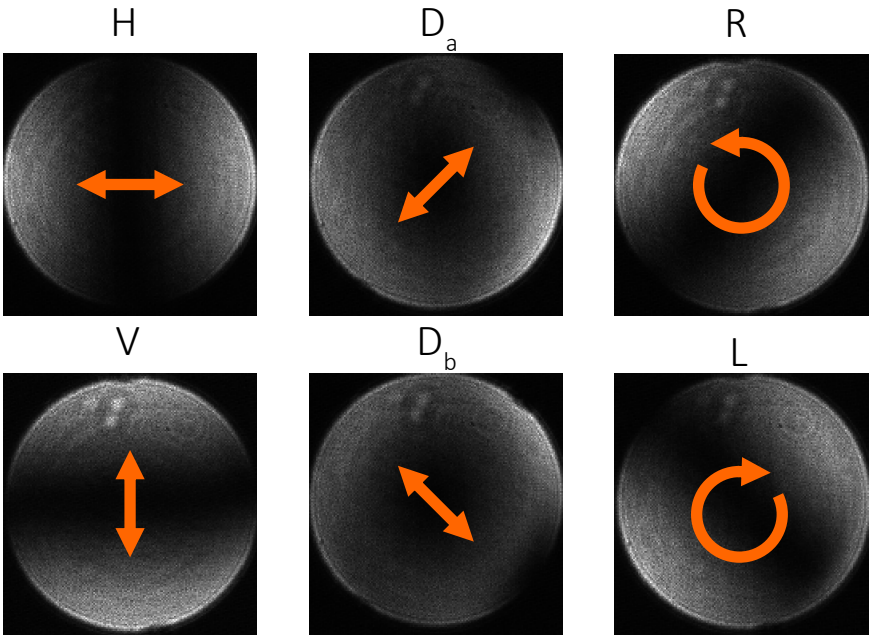

FIGURE 4.8: BFP images of the backward SHG from a nanoantenna with d=490 nm, acquired through six polarisation bases: linear horizontal (H), linear diagonal at 45° (D_a), right-hand circular (R), linear vertical (V), linear diagonal at -45° (D_b) and left-hand circular (L), as indicated by the orange arrows.

the six polarisation bases were obtained according to

$$(0°, 0°) \Rightarrow H \qquad (-45°, -45°) \Rightarrow D_a \qquad (0, 45°) \Rightarrow R$$
$$(90°, 90°) \Rightarrow V \qquad (-45°, 45°) \Rightarrow D_b \qquad (0, -45°) \Rightarrow L.$$

Once the six polarisation bases of the SHG were obtained, the parameters of the Stokes vector can be calculated according to:

$$\begin{bmatrix} I \\ Q \\ U \\ V \end{bmatrix} = \begin{bmatrix} H + V \\ H - V \\ D_a - D_b \\ L - R \end{bmatrix} \tag{4.3}$$

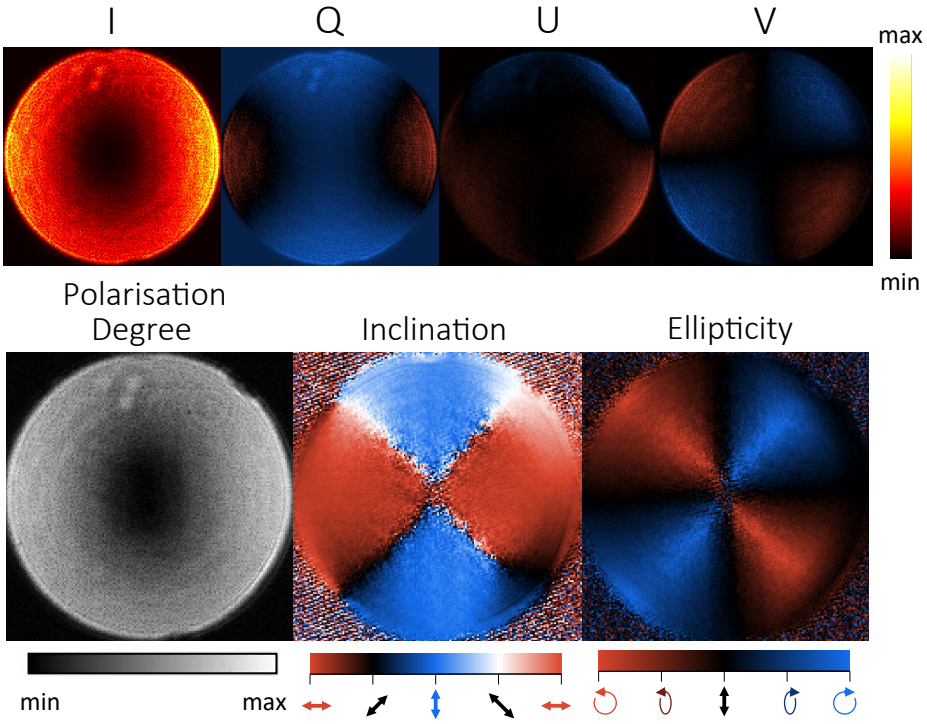

FIGURE 4.9: (a) Stokes vector components obtained from the backward SHG. (b) Retrieved spatially-resolved degree of polarisation, inclination and ellipticity. The images correspond to the SHG of a nanoantenna with d = 490 nm.

The four components of the Stokes vector, obtained in the backward direction for a nanoantenna with d=490 nm, are shown in Figure 4.9a. The polarisation degree, inclination, and ellipticity obtained from the Stokes vector (see Section A2) are shown in Figure 4.9b.

The BFP images of the forward and backward SHG from a nanoantenna with d = 490 nm are shown in the top of Figures 4.10a and c, respectively. In the SHG BFP images, we observe zero emission in the normal direction (*i.e.* the (0,0) coordinate of the images), in accordance to theoretical predictions (*107*). The same feature was observed in all SHG BFP images obtained from nanoantenna with d = 340-670 nm. This feature is explained by the symmetry of the nonlinear bulk tensor $\chi^{(2)}$ of the AlGaAs, therefore is not sensitive to the size of the nanoantenna. The THG BFP image in contrast, shows a maximum emission along the optical axis (see Figure 4.11) according to the components of the nonlinear tensor $\chi^{(3)}$ (see details in Section 2.1). The white arrows in Figure 4.10, correspond to the polarisation state of the SHG. The polarisation states were retrieved from the measured polarisation inclination and

ellipticity (see bottom panels of Figures 4.10a and c), obtained from the Stokes parameters. The polarisation of the forward and backward SHG show the formation of vector-beams with spatially variant polarisation states. In particular, the BFP image of the forward SHG (top of Figure 4.10a) observes a nearly perfect RP beam. While the BFP image of the backward SHG (bottom of Figure 4.10b) observes a more general polarisation state: a partially RP beam together with circular polarisation states. The calculations of the forward and backward SHG radiation patterns are shown in the top of Figure 4.10b and d, respectively. The intensities of the simulated 2D radiation patterns are consistent with the corresponding SHG BFP images, while the calculated polarisation states (see white arrows) are similar to the ones observed in the experiments. The small differences on the polarisation states, between calculations and measurements, was attributed to the homogeneous embedding medium of the AlGaAs nanoantenna considered in the simulations as compared to the partially homogeneous medium (BCB layer and air) of the fabricated AlGaAs nanoantennas. The nonlinear generation of the vector beams can be intuitively understood by the excitation of Mie-type multipoles at the SHG field. The higher-order multipoles excited at the SHG are superimposed and their superposition governs the output polarisation state. The multipoles excited at the SHG can be engineered to generate a nontrivial polarisation state or to create a specific polarisation state, as it has been shown in this chapter.

Under specific conditions, surface second-order nonlinearities can be observed in GaAs nanoantennas (*110*). The agreement observed between measurements and calculations (see Figure 4.10) suggests surface second-order nonlinearities do not play an important role in our case, since in the simulations only a $\chi^{(2)}$ bulk tensor was considered.

4.4 SHG of AlGaAs nanoantennas as a function of the incident polarisation beam

In the previous section, the properties of the SHG and the excitation of nonlinear multipoles were studied as a function of the nanoantenna diameter. In this section, we study the SHG and the excitation of nonlinear multipoles as a function of the fundamental beam polarisation.

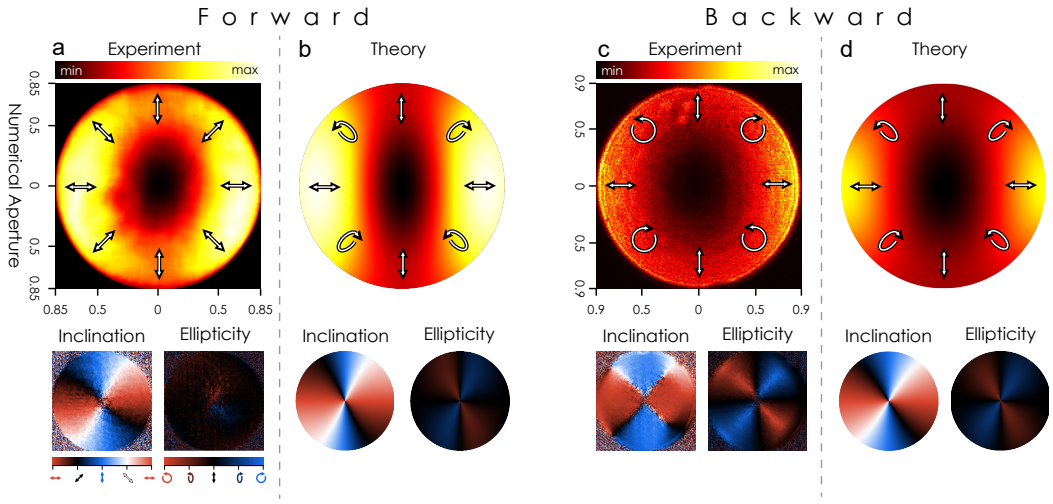

FIGURE 4.10: SHG directionality and polarisation state of a nanoantenna with d=490 nm. Top row: directionality diagrams in (a,b) forward and (c,d) backward directions. (a,c) Measurements and (b,d) theoretical calculations. White arrows represent the polarisation states. Bottom row: experimentally retrieved (a,c) and theoretical calculations (b,d) of polarisation inclination and ellipticity, corresponding to the cases of the top row.

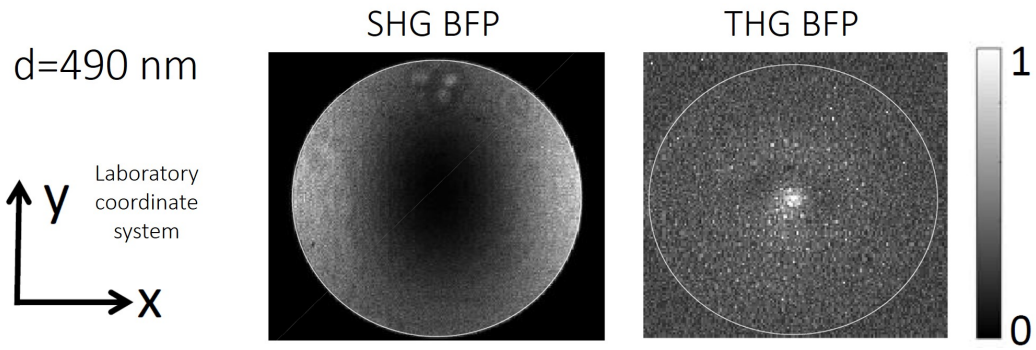

FIGURE 4.11: SHG and THG back-focal plane images of an AlGaAs nanoantenna with d=490 nm, measured in the backward direction.

Therefore, the co-relation between the excitation of nonlinear multipoles and the polarisation state of the SHG, mentioned in the previous section, will be further explored.

4.4.1 SHG multipolar decomposition

In this section we analyse the multipolar decomposition of the SHG, for different polarisation angles φ of the fundamental beam. Here, the polarisation angle φ is taken in reference to

the [100] crystalline axis of the AlGaAs nanoantenna, as depicted in Figure 4.12a. The finite element method solver in COMSOL Multiphysics was used to calculate the nonlinear decomposition of AlGaAs nanoantennas embedded in a homogeneous medium (n=1.44), and illuminated by a fundamental beam at 1550 nm wavelength. For more details regarding the simulations refer to Section 4.3.3. The SHG multipolar decomposition was calculated for two pump polarisation angles $\varphi = 45°$ and $\varphi = 0°$, as shown in Figure 4.12b and c, respectively. In general, the decomposition of the SHG field shows that the number of nonlinear multipoles increases with the diameter of the nanoantenna. The nonlinear decomposition also shows that the SHG is characterised by electric multipoles when $\varphi = 45°$, while it is predominantly magnetic when $\varphi = 0°$ since a single electric octupole mode contributes to the SHG in this case. In fact, when $\varphi = 0°$ the contribution of the electric octupole mode to the SHG becomes close to zero for nanoantennas with small (300 to 350 nm) and large (450 to 500 nm) diameters, as shown in Figure 4.12c. Therefore, specific nanoantenna diameters allows studying electric and magnetic SHG, depending of the polarisation angle φ of the fundamental beam. For example, for a nanoantenna with d = 360 nm a clear distinction of the excited SHG multipolar modes can be observed: for $\varphi = 45°$ the emission is dominated by an EQ, while for $\varphi = 0°$ the emission is dominated by a MD and a MO. In the next section, the SHG properties of a nanoantenna with d = 360 nm are investigated. The choice of this nanoantenna was made in terms of the purely electric or magnetic nonlinear optical modes selectively excited by the polarisation angle of the fundamental beam, together with the enhancement of the SHG efficiency around this diameter. In the case of $\varphi = 45°$, the high efficiency of the second-harmonic is explained by the excitation of a strong nonlinear EQ mode. While for $\varphi = 0°$, the strong nonlinear optical magnetism is explained by the excitation of two resonant magnetic modes, dipole and octupole.

4.4.2 Directionality and polarisation state of SHG

The 3D far-field SHG radiation patterns of a disk nanoantenna with d =360 nm were calculated, using COMSOL Multiphysics. The calculated far-field SHG radiation patterns, induced by two polarisation angles of the fundamental beam, $\varphi = 45°$ and $\varphi = 0°$, are shown in

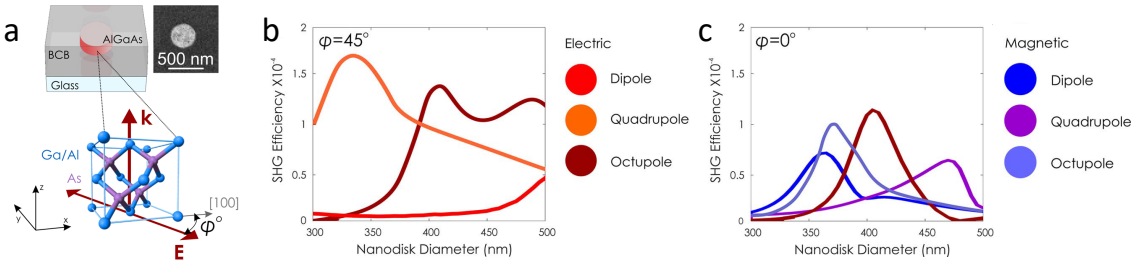

FIGURE 4.12: (a) Schematic structure and SEM image of fabricated AlGaAs nanoantenna. The crystalline structure of the AlGaAs material, together with the relative directions of the fundamental propagation vector **k** and the fundamental electric field **E** are shown at the bottom. Multipolar decomposition of SHG, induced by two polarisation angles of the fundamental field: (b) $\varphi = 0°$, and (c) $\varphi = 45°$. Panel *b* is dominated by electric multipoles, whereas panel *c* is dominated by magnetic multipoles.

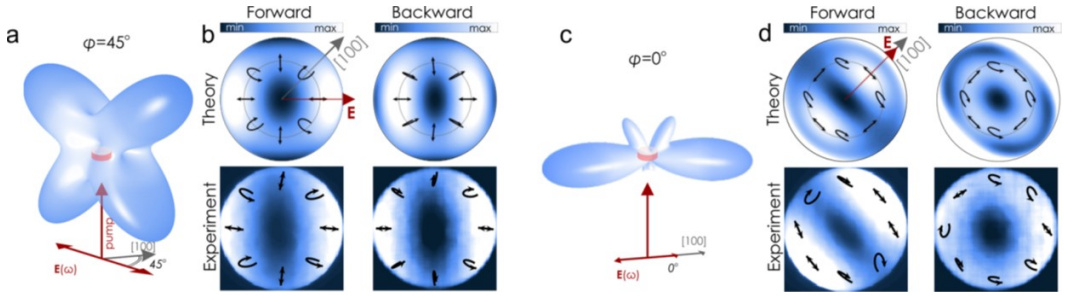

FIGURE 4.13: SHG directionality and polarisation diagrams of a nanoantenna with *d*=360 nm. Calculated SHG 3D radiation patterns of a nanoantenna excited by a fundamental beam polarised at (a) 45° and (c) 0° angles. Calculated and measured SHG 2D radiation patterns of a nanoantenna excited by a fundamental beam polarised at (b) 45° and (c) 0°, together with its polarisation states indicated by the black arrows. In the calculations the outer circle indicates a full NA of 1.44 while the inner circles indicate the NA of the experimental optical system. The measured radiation patterns are limited by the NA of the objective lenses, 0.9 in the forward direction and 0.85 in the backward direction.

Figures 4.13a and c. The far-field SHG radiation pattern corresponding to an angle $\varphi = 45°$ shows a symmetric four-lobe emission typical of an electric quadrupole. Meanwhile, the far-field SHG radiation pattern corresponding to an angle $\varphi = 0°$ shows two side lobes strongly emitting at angles perpendicular to the propagation of the fundamental beam. These side lobes are typical of an octupolar emission.

The 2D angular radiation patterns, projected from the upper and lower half-space of the 3D far-field radiation patterns, together with its polarisation states (see black arrows) are shown in the top of Figures 4.13b and d. The corresponding SHG BFP images, shown in the bottom of Figures 4.13b and d, agree with the calculated 2D radiations patterns. Experimentally, the polarisation states of the SHG were retrieved using Stokes formalism (see Section 4.3.3). The 2D radiation patterns corresponding to an excitation at $\varphi = 45°$ (see Figures 4.13b) exhibit a second-harmonic polarisation pattern similar to a RP beam. In contrast, the 2D radiation patterns corresponding to an excitation at $\varphi = 0°$ (see Figures 4.13d) exhibit a second-harmonic polarisation pattern similar to an AP beam. In both cases, there is a small degree of ellipticity.

4.4.3 Electric and magnetic SHG

A nearly-azimuthally polarised second-harmonic beam is observed in Figure 4.13d, where the SHG is dominated by magnetic modes (see Figures 4.12c). Meanwhile, a nearly-radially polarised second-harmonic beam is observed in Figure 4.13b, where the SHG is dominated by electric modes (see Figure 4.12b). These polarisation patterns can be understood by considering a source radiating in a purely electric or magnetic dipole mode. When the SHG is dominated by an electric dipole, the SHG electric field vectors exhibit a radially polarised pattern, as shown in Figure 4.14a. Meanwhile, when the SHG is dominated by a magnetic dipole mode, the SHG electric field vectors exhibit an azimuthally polarised pattern as shown in Figure 4.14b.

In a more general case, where electric or magnetic modes of different orders are excited (as in our case), the second-harmonic polarisation state can be studied to determine the generation of either electric or magnetic modes at the second-harmonic field. Moreover, the transition between electric and magnetic nonlinearities can be determined by studying the SHG polarisation state. For this purpose, the parameter M was defined as:

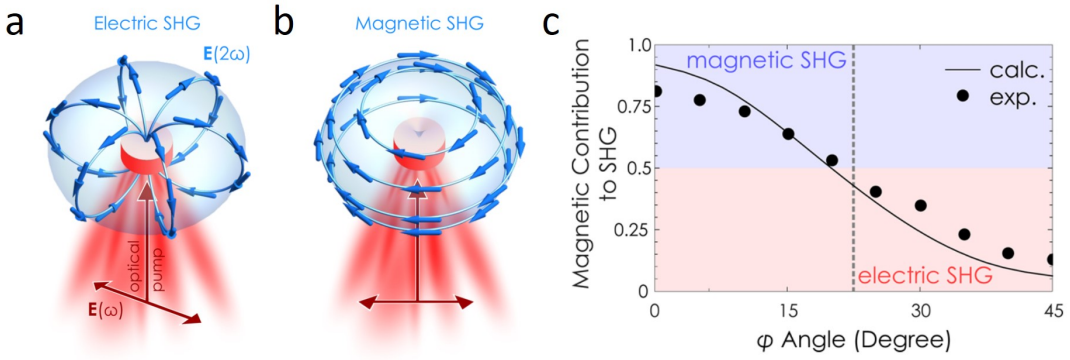

FIGURE 4.14: (a) Electric and (b) magnetic SHG for the simplest cases of dipolar emission. Blue arrows show the electric field vectors of the SHG radiation patterns. (c) Calculated and experimentally retrieved magnetic contribution to the SHG of an AlGaAs nanoantenna with d=360 nm.

$$M = \frac{\int |E_{\perp}(2\omega, \rho, \theta)|^2 \, d\rho}{\int |E_{tot}(2\omega, \rho, \theta)|^2 \, d\rho},$$

where ρ and θ are the polar coordinates of the far-field radiation pattern, E_{tot} is the total amplitude of the second-harmonic field and $E_{\perp}$ is the portion of the second-harmonic field perpendicular to crystalline axis. The calculation of M allows to quantify, both experimentally and numerically, the contribution of electric and magnetic multipoles to the SHG. When $M = 1$ the SHG is characterised by a purely magnetic multipolar emission also know as nonlinear optical magnetism; when $M = 0$ the SHG is characterised by a purely electric multipolar emission. The parameter M was retrieved from a nanoantenna with $d = 360$ nm, as a function of the fundamental polarisation angle φ (see Figure 4.14c). The experimental values of M are shown by dots, while the calculated values of M are shown by the black solid line. A continuous transition between electric and magnetic SHG is observed in Figure 4.14c, when φ is tuned from 0° to 45°. The differences between experiments and calculations can be explained by the smaller integration angle ρ considered in the measurements, limited by the NA of the optical system, as compared to the simulations.

To obtain the experimental value of M, the corresponding SHG BFP images and their polarisation states were measured, as shown in Figure 4.15a. In the forward direction, the SHG BFP

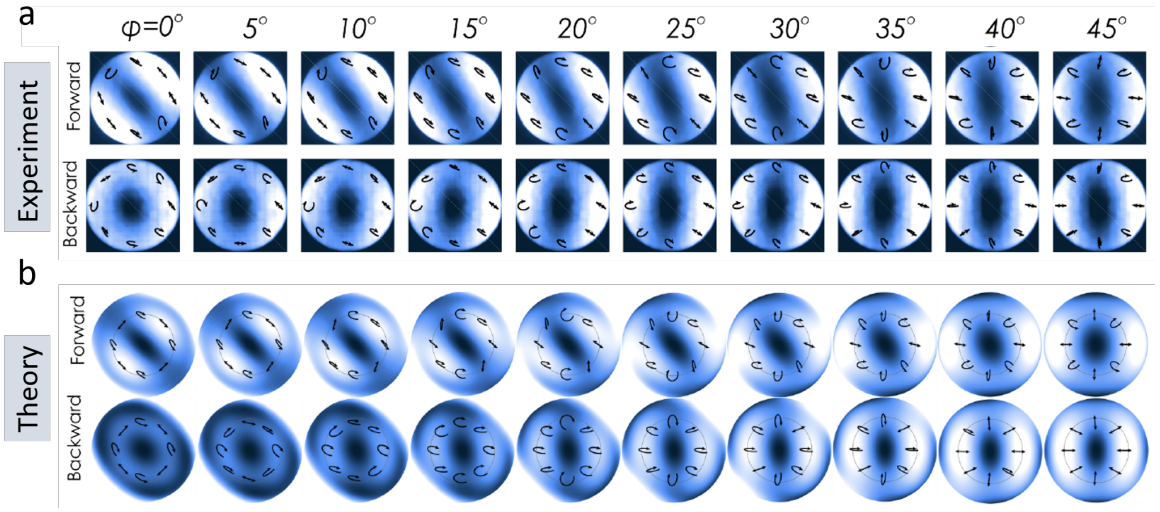

FIGURE 4.15: (a) Measured and (b) calculated second-harmonic radiation patterns of a nanoantenna with d=360 nm, and their corresponding polarisation states. The angle of the fundamental beam is changed from 0° to 45°, with a 5° step.

images observe a continuous rotation of the side lobe emission (white areas), following the rotation of the angle φ. In the backward direction, the SHG BFP images observe a similar rotation of the side lobe emission and a total intensity that is dependent of the angle φ. The total intensity is low for $\varphi = 0°$, as the angle approaches to $\varphi = 45°$ the total intensities are higher. In both propagation directions, the second-harmonic polarisation states observe a transition between a nearly-azimuthally polarised beam for $\varphi = 0°$ to a nearly-radially polarised beam for $\varphi = 45°$, with a high contribution of elliptically polarisation states. The corresponding simulations shown in Figure 4.15b, are consistent with the performed measurements.

4.5 Conclusions

In summary, we studied the radiation patterns and polarisation states of the SHG from AlGaAs nanoantennas. We have shown experimental SHG conversion efficiencies of the order of 10^{-4}, and nonlinear nanoscale light sources emitting vector beams with designed polarisation state, *e.g.*, radial polarisation. In addition, a continuous control in the transition between electric and magnetic nonlinear responses was demonstrated by tuning the polarisation of the optical excitation beam. As the electric and magnetic nonlinear processes generate light with

orthogonal polarisation states, the induced second-harmonic electric and magnetic modes can be experimentally differentiated by studying their polarisation state. The results shown in this chapter are promising in achieving nanoscale functional nonlinear devices.

CHAPTER 5

Tailored SHG from (111)- and (110)-GaAs nanoantennnas

5.1 Introduction

In the previous chapter, individual (100)-AlGaAs nanoantennas demonstrated different nonlinear effects under the excitation of Mie resonances such as generation of vector beams and nonlinear optical magnetism. However, an important case of SHG has not been observed in this thesis: SHG emitted along the optical axis, limiting the applications of GaAs-based nanoantennas. The absence of SHG along the optical axis prevails in the studies performed by other groups, where individual (*106*, *149*) and dimer (*141*) (100)-AlGaAs nanoantennas were excited under normal incidence. A non-zero second-harmonic emission can be generated along the optical axis by breaking the symmetry of the system.

Several approaches have been adopted to reduce the symmetry of the system including tuning the angle of incidence of the fundamental beam (with respect to the normal direction) (*107*, *150*), and designing asymmetric nanodimers to reduce the symmetry of the resonant modes (*151*). Both alternatives however, come at the price of complexity in the experimental implementation or in the nanoantenna design and fabrication. A common fact that has been overlooked in the mentioned approaches is the special properties of the zinc blende nonlinear tensor. In the nonlinear regime, the symmetry of the system can be broken by changing the orientation of the second-order nonlinear tensor (see Section 2.2). More generally, the nonlinear properties of the zinc blende tensor can be used to engineer the SHG properties of GaAs-based nanoantennas, *e.g.* by fabricating nanoantennas along different crystallographic orientations. In our fabrication method, the crystal growth axis of the GaAs nanoantennas is controlled by the GaAs wafer cut (see Section 2.4).

In this chapter, we use the nonlinear tensorial properties of zinc blende material to break the symmetry of the system and to design (111)- and (110)-GaAs nanoantennas exhibiting specific second-harmonic directionalities. Under the simple case of normal incidence, we show non-zero second-harmonic emission along the optical axis by employing (111)-GaAs nanoantennas (*152*). In addition to non-zero second-harmonic emission, we demonstrate switching between forward and backward second-harmonic emission by using (110)-GaAs nanoantennas. The switching was possible by controlling two parameters: the size of the nanoantennas and the polarisation angle of the fundamental beam (*104*). The control of the SHG directionality includes the interesting case of unidirectional nonlinear emission.

5.2 Fabrication of (111)- and (110)-GaAs nanoantennas

The growth of GaAs epitaxial layers on the (100) crystallographic plane by MOCVD is a well established process, however the growth of GaAs epitaxial layers on the (111)- and (110)-GaAs oriented substrates is not trivial (*153*, *154*). The orientation of the substrate in the growth of epitaxial GaAs layers plays an important role in the surface quality of the layer. Epitaxial layers of GaAs on (100) substrates can give exceptional surface quality over a wide range of growth conditions, while the growth of GaAs layers on (111) and (110) substrates has showed defects which are highly dependent on the growth parameters (*154*). Under limited growth conditions, epitaxial layers of GaAs with a smooth surface morphology has been reported on (111)A substrates (*155*). Hence, optimisation of GaAs and AlAs planar growth was performed on (111)A- and (110)-GaAs substrates to fine tune the growth parameters, improve the surface morphology of the layers and attain minimal surface roughness. The growth of this epitaxial layers was performed by our collaborators using the ANFF, ACT Node facilities.

To fabricate the (111)- and (110)-GaAs nanoantennas, a 20 nm layer of AlAs followed by a 400 nm layer of GaAs were growth on a (111)A and (110) GaAs substrate. The thin AlAs layer was used as an lift-off buffer layer. On the top of the GaAs layer, a SiO_2 layer was deposited via PECVD. A patterned SiO_2 mask was fabricated using a conventional e-beam

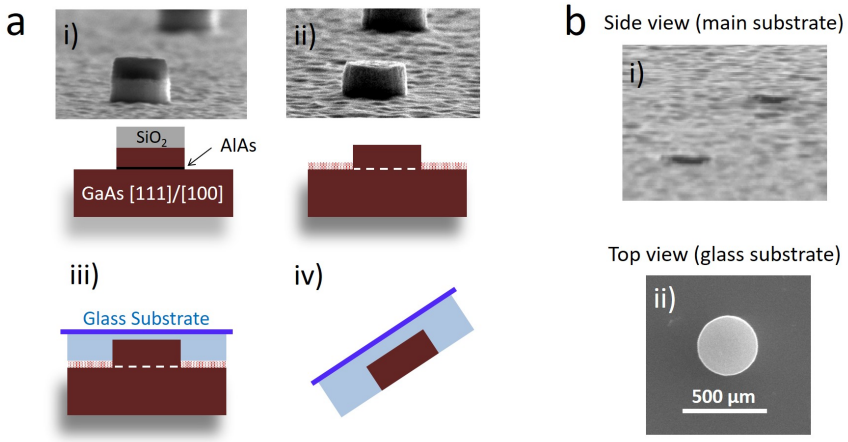

FIGURE 5.1: (a) Fabrication procedure performed to obtain GaAs nanoantennas in a transparent medium: (i) GaAs nanoantennas defined on a GaAs wafer via electron-beam lithography and sequential etching. The SiO_2 is used as a mask and the AlAs as a sacrificial layer. (ii) Removal of the SiO_2 mask and AlAs buffer layer by HF acid, followed by (iii) coating of a BCB layer, curing and bonding it onto a thin glass substrate. (iv) Final sample containing the GaAs nanoantennas, after peeling off. (b) Scanning electron microscope images after peeling off: (i) side view of the main substrate (ii) top view of the final sample on glass substrate.

lithography procedure. Using a reactive ion etching (RIE), SiO_2 pattern was transferred to the GaAs and AlAs layers, as well to a part of the GaAs wafer. The SiO_2 mask and the AlAs layer were removed by hydrofluoric acid, which resulted in having GaAs nanodisks sitting on the GaAs wafer with minimum adhesion. Next, 4 μm of BCB layer was spin-coated on the sample, followed by its curing and bonding to a thin glass substrate. Finally, the glass substrate with the GaAs nanodisks embedded in the BCB layer was peeled off from the main GaAs wafer. This fabrication procedure is illustrated in Figure 5.1a, for more details see Section 2.4. Scanning electron microscope images of (i) the main substrate after the lift-off, and (ii) the nanodisk after being transferred to a thin glass substrate are shown in Figure 5.1b.

This fabrication procedure offers several benefits as compared to conventional methods, where GaAs nanoantennas are fabricated on a thin aluminium-oxide low-index layer (*110*, *111*, *113*). In our case, the index contrast between the bottom of the GaAs nanoantennas and the underlying glass substrate is larger than when low-index underlying layers are used; this larger index contrast decreases the leakage of resonant modes into the substrate.

Conventional fabrication methods restrict the study of SHG to a single direction: backward second-harmonic emission using a reflection geometry, or forward second-harmonic emission when the nanoantenna is illuminated through the substrate. In our case, the glass substrate is transparent not only to the wavelength of the excitation beam but also to the second-harmonic wavelength (considering an excitation wavelength of 1550 nm), allowing the optimisation of the SHG radiation pattern in the backward and forward directions. SHG of GaAs substrate can interfere with the SHG of GaAs nanoantennas, difficulting the separation of both SHG (*113*). Therefore, the use of a glass substrate avoids the interference of both nonlinear emissions and facilitates the measurements.

5.3 SHG of (111)-GaAs nanoantennas

Individual GaAs nanoantennas were excited by a fundamental beam at a frequency ω, generating a second-harmonic emission at a frequency 2ω, as illustrated in Figure 5.2a. The nanoantennas were fabricated from a (111)-GaAs epitaxial layer which effectively rotates the nonlinear susceptibility tensor of the GaAs material. In this case, the tetrahedral bonding of the atoms within the zinc blende lattice leads to one of the bonds pointing downwards and the three other bonds pointing upwards and spreading out with an angle of 120°, as indicated in the inset of Figure 5.2a. In the next section, a three-fold symmetry of the SHG from (111)-GaAs nanoantennas is demonstrated as a translation of the mentioned atomic arrangement.

5.3.1 Fundamental and second-harmonic resonances

Simulations of the fundamental field in GaAs nanoantennas were performed by employing the finite element method. In the simulations, GaAs nanoantennas (with a fixed height of 400 nm and varying radii) were excited by a normal plane wave at a FW of 1550 nm. In the calculations normal incidence of the fundamental beam was considered, even when a tightly focused beam is experimentally employed. This approximation is valid since the non-normal

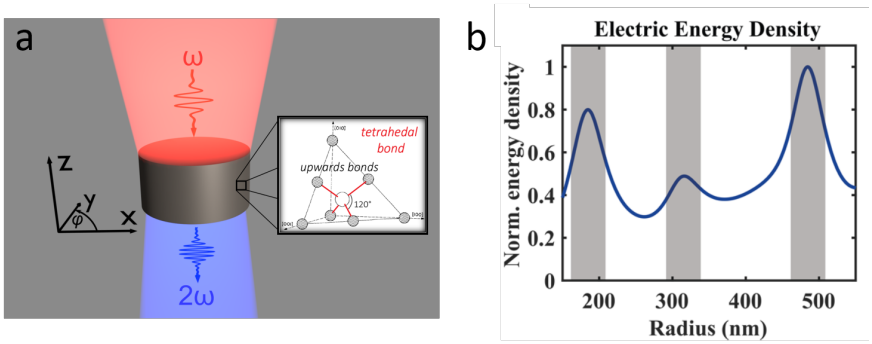

FIGURE 5.2: (a) Schematic of individual nanoantennas experiment. The inset shows the zinc blende crystal structure in the (111) plane orientation, with atoms bonded in a tetrahedal phase. (b) Calculated electric energy density as a function of the nanoantenna radius. The gray bars highlight the peaks of enhancement.

components of a tightly focused beam can be grouped in pairs (with same angle but opposite sign) that cancel with each other.

First, the electric energy density was calculated as a function of the nanoantenna radius and normalised, as illustrated in Figure 5.2b. The electric energy density is characterised by three peaks of enhancement indicated by gray shaded areas. This near-field enhancement can lead to an increase in the SHG efficiencies. To understand the origin of the electric energy peaks, the scattering cross-section and its multipolar decomposition were calculated through the study of the polarisation currents excited inside the GaAs nanoantennas.

The calculation of the scattering cross section and its multipolar decomposition (using spherical coordinates) is shown in Figure 5.3a. Again, the gray areas indicate the positions of the energy density peaks, according to Figure 5.2b. The first peak observed in the scattering cross section originates from the resonant behaviour of the ED and MD; it also explains the enhancement of the energy density around a nanoantenna with radius (r) of 150 nm. As the radius of the nanoantennas increases, the scattering cross section observes two dips; the first one around a nanoantenna with $r = 315$ nm and the second around a nanoantenna with $r = 480$ nm. According to the multipolar decomposition, the first dip in the total scattering is mainly attributed to the ED mode, while the second dip is mainly attributed to the MD mode. Most importantly, the two dips in the total scattering are located around the same positions of the energy density peaks. The two conditions, near-field enhancement (given by the energy

density peaks) and suppression of the total scattering, around the nanoantenna with r = 315 nm and r = 480 nm are indicative of the excitation of an anapole state. To verify the excitation of an anapole state around these nanoantennas, multipolar decomposition calculations were performed in cartesian coordinates as a function of the nanoantenna radius, the calculations are shown in Figure 5.3b. The overlap of the cartesian ED mode and the TD mode around a nanoantenna with r = 315 nm originates an electric anapole mode (see Section 1.3.3.2). The energy density around the nanoantenna with r = 315 nm is enhanced by the excitation of the anapole state and higher-order modes like the EQ and MQ (see Figure 5.3a). Meanwhile, the overlap of the cartesian MD and the MR around a nanoantenna with r = 480 nm originates a magnetic anapole state. The excitation of a magnetic anapole state around the nanoantenna with r = 480 nm, together with the excitation of higher order modes like the MO results in the enhancement of the energy density inside the nanoantenna. The cylindrical symmetry of the GaAs nanoantennas, together with the isotropic refractive index of the GaAs material have consequences in the linear behaviour of the nanoantennas. The linear scattering and the energy density of the nanoantennas are both independent of the polarisation angle of incident beam and the crystal orientation of the nanoantennas. The nonlinear behaviour of the GaAs nanoantennas is however, sensitive to both parameters: the polarisation angle of the incident beam and the crystal orientation of the nanoantennas.

The total SHG efficiency was calculated as a function of the nanoantenna radius for three polarisation angles of the fundamental beam, following the expressions of the nonlinear currents derived for a (111)-oriented GaAs material. The calculated SHG efficiency, shown in Figure 5.4a, is independent of the polarisation angle φ of the fundamental beam and is characterised by three peaks of enhancement. The forward SHG was measured for the same incident polarisation angles. In the measurements, individual GaAs nanoantennas were excited by a femtosecond laser (Toptica FemtoFiber Pro NIR) with a pulse length of 100 fs, repetition rate of 80 MHz and centre wavelength of 1556 nm. The laser beam was focused on the GaAs nanoantennas using an infrared objective lens with a NA of 0.7. The forward SHG together with the transmitted fundamental beam was collected by a visible objective lens with a NA of 0.9. The fundamental beam was filtered-out using a 800 nm short-pass filter. The SHG efficiency was measured using $\eta = P_{SHG}/P_{FW}$, where P_{SHG} is the average

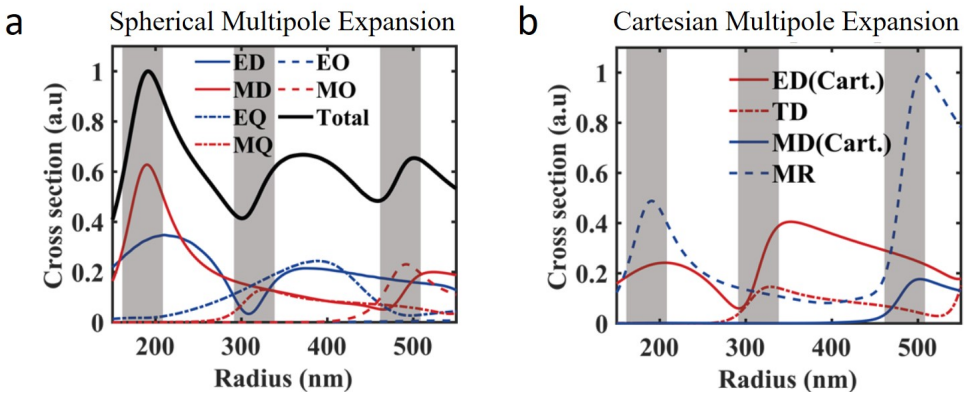

FIGURE 5.3: (a) Calculated linear scattering cross section and its spherical multipolar expansion (b) Calculated cartesian multipole expansion of cartesian electric and toroidal dipole modes, together with the cartesian magnetic dipole (MD) mode and mean radii (MR) distributions. In the calculations, cylindrical GaAs nanoantennas with height of 400 nm and varying radii were illuminated by a plane wave with a wavelength of 1550 nm. The gray areas highlight the three peaks observed in the calculated electric energy density.

power of the SHG measured by a calibrated camera and P_{FW} is the average power of the fundamental beam impinging in the cross section of the nanoantennas. In our experiments, the intensity of the fundamental beam was equal to 1 GW/cm^{-2}. The measured forward SHG is shown in Figure 5.4b, as a function of the nanoantenna radius. As expected, the SHG efficiency shows three peaks of enhancement driven by the behaviour of the fundamental near-field (see Figure 5.2b). Each peak has the same amplitude for the three polarisation angles φ. Differences in the relative amplitude of the calculated and measured SHG efficiency peaks are observed in Figure 5.4. In the simulations, the total SHG efficiency was calculated, accounting for the forward and backward emission. While in the experiments only the forward SHG, from a cone within an opening angle of 64° around the normal direction, was measured. The position of the measured SHG resonant peaks are shifted with respect to the calculated peaks. This shift was attributed to fabrication imperfections.

In this section, three peaks of enhancement were observed in the SHG efficiencies, attributed to the near-field distribution of the fundamental field. The amplitude of the SHG efficiencies was constant for the three incident polarisation angles. In the next section, the SHG radiation patterns of GaAs nanoantennas will be studied.

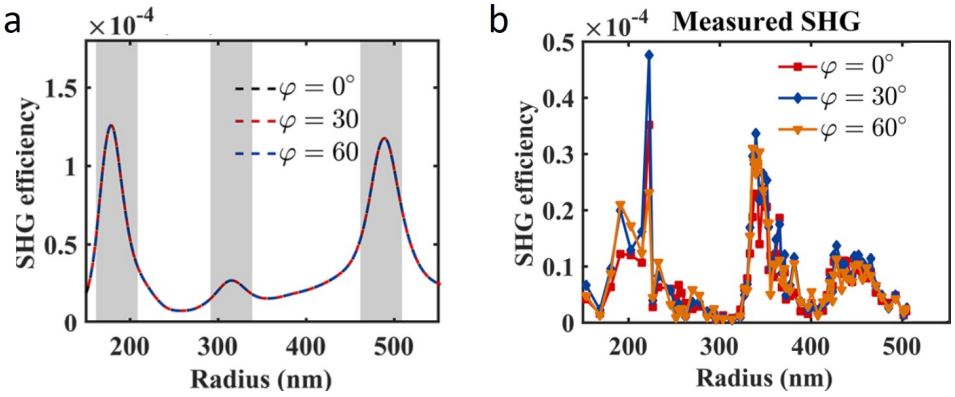

FIGURE 5.4: (a) Total SHG efficiencies of (111)-GaAs nanoantennas, calculated for three polarisation angles φ of the fundamental beam. (b) Forward SHG efficiencies of (111)-GaAs nanoantennas measured for the same three polarisation angles φ. The calculations and measurements display a polarisation independent behaviour of the SHG from (111)-GaAs nanoantennas.

5.3.2 SHG radiation patterns of GaAs nanoantennas

The SHG radiation patterns of a GaAs nanoantenna were simulated and measured as illustrated in Figure 5.5. In the simulations, a nanoantenna with r = 320 nm was considered, where the calculated SHG efficiency is enhanced due to the excitation of an electric anapole mode (see Section 5.3.1). In the experiments, a nanoantenna with r = 340 nm was measured, where enhancement of forward SHG efficiency was observed (see Figure 5.4b). The simulated 3D far-field SHG radiation patterns of a nanoantenna excited by three polarisation angles (φ = 0°, 30° and 60°) are shown in Figure 5.4a. For the three polarisation angles, the upper-half space projection of the SHG far-field radiation pattern, corresponding to the forward SHG radiation patterns, is shown in Figure 5.5b. In every case, the radiation pattern inside the black circles corresponds to the SHG collected by an objective lens with a NA of 0.9, and therefore to the measured SHG BFP images displayed in Figure 5.5c. The calculated forward SHG radiation patterns are repeated every 60°, with a rotation of 120° around the y axis (see Figure 5.5b with φ = 0° and φ = 60°). Another important feature of the SHG radiations patterns is the emission shown around the normal direction. Compared to the SHG radiation patterns of (100)-AlGaAs nanoantennas (see Section 4.3.3 and Section 4.4.2), here the SHG radiation patterns of (111)-GaAs nanoantennas show emission around the normal direction. The differences between the calculated and experimental SHG radiation patterns were attributed to a possible tilt of the

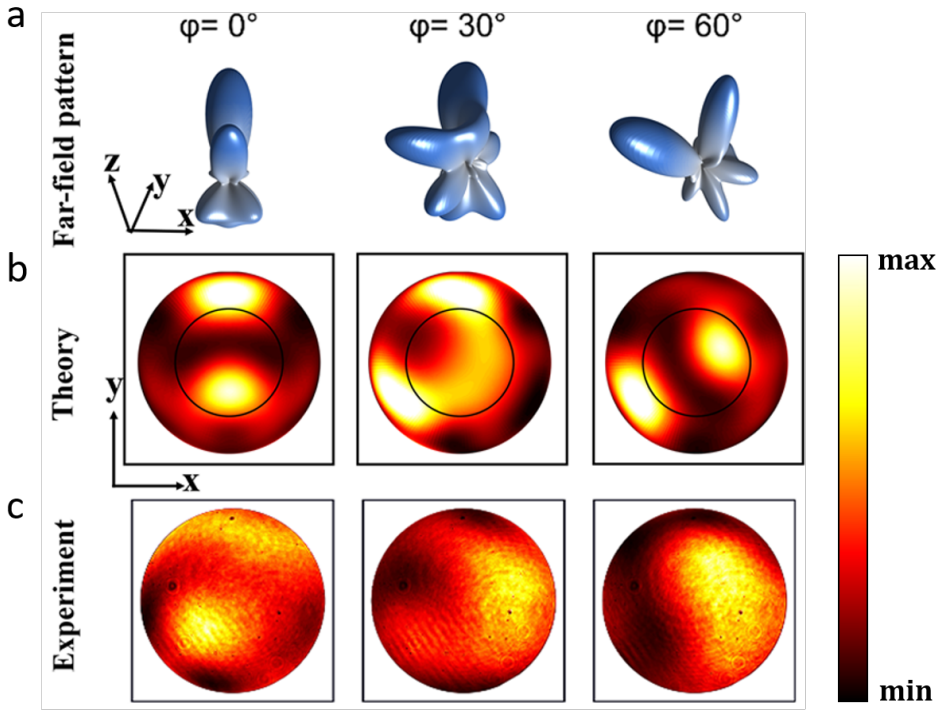

FIGURE 5.5: SHG radiation patterns of (111)-GaAs nanoantenna excited by three incident polarisation angles: $\varphi = 0°$, $\varphi = 30°$, and φ=60°. (a) Calculated 3D SHG far-field radiation patterns. (b) Calculated and (c) measured forward SHG radiation patterns. The black circles in the calculated forward SHG radiation patterns indicate the angular aperture of the objective lens used in the optical system (NA of 0.9). In the simulations, a nanoantenna with r=320 nm was considered while in the experiments, a nanoantennas with r=340 nm was measured.

nanoantennas with respect to the glass substrate surface. This tilt can be induced during the fabrication procedure, due to tension within the BCB layer when it is transferred to the glass substrate (see Section 5.2). Onward, the second-harmonic emission shown at the centre of the radiation patterns will be nominated normal second-harmonic generation to make reference to the nonlinear emission along the optical axis and in the normal direction.

In this section, we showed the SHG far-field patterns of (111)-GaAs nanoantennas can be controlled by the polarisation angle of the fundamental beam, while the total SHG efficiency of the same nanoantenna remains constant at different polarisation angles.

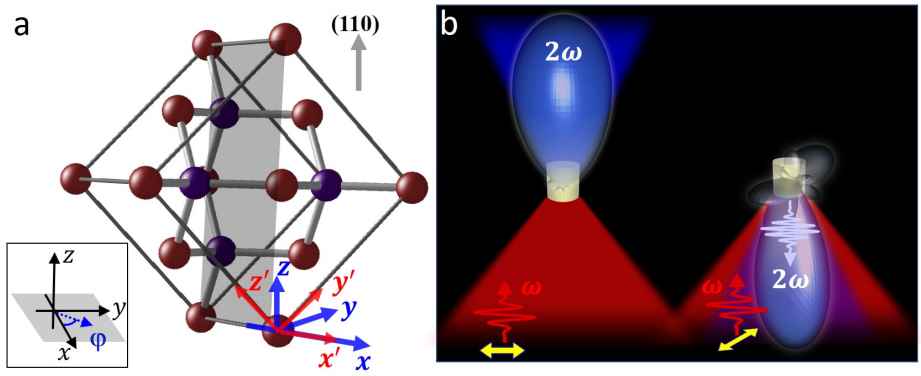

FIGURE 5.6: (a) Illustration of the (110) zinc blende crystal plane. The laboratory and crystal coordinates are defined as (x, y, z) and $(x^{'}, y^{'}, z^{'})$, respectively; φ is the in-plane polarisation angle of the fundamental beam with respect to the x-axis. (b) Schematic of all-optical switchable nonlinear emission from (110)-GaAs nanoantennas.

5.4 SHG of (110)-GaAs nanoantennas

In this section, we study the SHG from individual (110)-GaAs nanoantennas, excited at different polarisation angles φ of the fundamental beam (see Figure 5.6a). The forward and backward SHG of GaAs nanoantennas, embedded in a transparent low-index material, were simultaneously studied. Switchable directional SHG was obtained by controlling the size of the nanoantenna and the polarisation angle of the fundamental beam (see Figure 5.6b).

5.4.1 Forward and backward SHG intensity

Individual (110)-GaAs nanoantennas were fabricated (see Section 5.2) in the range of 150 to 350 nm radius, with a step size of 2 nm, and at a fixed height of 400 nm. In this range, the nanoantennas support only low-order multipoles (up to quadrupoles) at the FW of 1450 nm. The nanoantennas were positioned 10 μm apart, which makes them optically isolated. A femtosecond laser beam (duration pulse of 225 fs and repetition rate of 80 MHz) with 10 mW of average power and operating wavelength of 1450 nm, was used as the fundamental beam. The fundamental beam was focused by an objective lens (NA of 0.7) on the nanoantennas, to

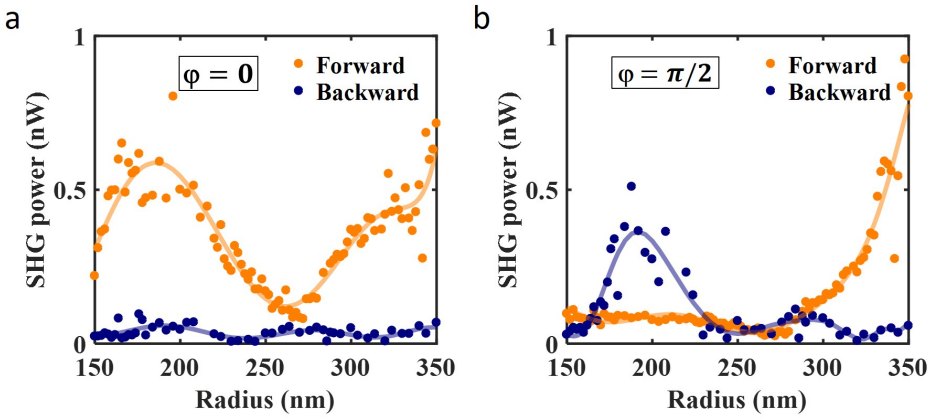

FIGURE 5.7: Measured power of the forward and backward SHG, as a function of the nanoantenna radius, when the angle φ of the fundamental beam is polarised along the (a) x-axis and (b) y-axis.

a 2 μm diffracted-limited spot size. The backward SHG was collected by the same objective lens, while the forward SHG was collected by another objective lens (NA of 0.8).

The average power of the forward and backward SHG was measured (dots) and calculated (solid line), as shown in Figure 5.7. The power of the SHG was plotted as a function of the nanoantenna radius for two polarisation angles, $\varphi = 0$ (x-polarised) and $\varphi = \pi/2$ (y-polarised), of the incident beam. As shown in Figure 5.7a, when a polarisation angle of $\varphi = 0$ is considered, the forward SHG shows two peaks of enhancement, while the backward SHG is low for all the nanoantenna studied. Figure 5.7b considers a polarisation angle of $\varphi = \pi/2$, where in contrast the forward SHG has one peak of enhancement for large nanoantenna radii and the backward SHG has one peak of enhancement for small nanoantenna radii. Thus, for a polarisation angle of $\varphi = \pi/2$, the forward to backward SHG can be controlled by changing the nanoantenna radius. For small nanoantenna radii the backward SHG dominates over the forward emission. Around a nanoantenna with $r = 250$ nm, similar contribution of the forward and backward SHG is observed. Finally, for the largest nanoantenna radii the forward SHG dominates over the backward emission. Interestingly, when considering specific nanoantenna, the backward to forward SHG ratio can be also controlled by the polarisation angle φ. For example, around a nanoantenna with $r = 200$ nm and a polarisation angle of $\varphi = 0$, the forward SHG dominates over the backward SHG. Instead, if the polarisation angle is $\varphi = \pi/2$,

the backward SHG dominates over the forward SHG. Therefore, the relative forward and backward SHG can be tuned by the nanoantenna radius or the polarisation of the fundamental beam. The interesting features observed in the SHG are attributed to the properties of the second-order nonlinear tensor of (110)-orientated GaAs nanoantennas (*104*).

5.4.2 Forward and backward SHG radiation patterns

The 2D backward and forward SHG radiation patterns of (110)-GaAs nanoantennas were measured by imaging the BFP of the objective lenses (see Section A3). The SHG radiation patterns of three nanoantennas with different radii, obtained with an angle $\varphi = 0$, are shown in Figure 5.8. The nanoantennas with $r = 180$ nm and $r = 260$ nm correspond to a resonant and off-resonance forward SHG, respectively (see Figure 5.8a); while the nanoantenna with $r = 230$ nm correspond to a middle state. The forward SHG radiation patterns observe strong normal emission for the three nanoantennas studied. In contrast, the backward SHG radiation patterns only observe strong normal emission for the resonant nanoantennas with $r = 180$ nm. The calculated SHG radiation patterns are well correlated with the corresponding experimental images. The small differences observed between experiments and calculations were attributed to non-uniform fabricated nanoantennas.

Earlier in Section 5.4.1, the control of the forward to backward SHG was discussed by changing the incident polarisation angle. This concept is illustrated in Figure 5.9, where the SHG radiation patterns of a nanoantenna with $r = 210$ nm were measured for two polarisation angles, $\varphi = 0$ and $\varphi = \pi/2$. A strong forward SHG occurs when $\varphi = 0$, while the backward SHG is simultaneously suppressed (see Figure 5.9a). If the polarisation angle is changed to $\varphi = \pi/2$, enhanced SHG occurs in the backward direction with the suppression of the forward SHG (see Figure 5.9b). These results demonstrate the possibility of using (110)-GaAs nanoantennas as tunable nonlinear "Huygens" sources, where high directionality and vanishing backward scattering is observed.

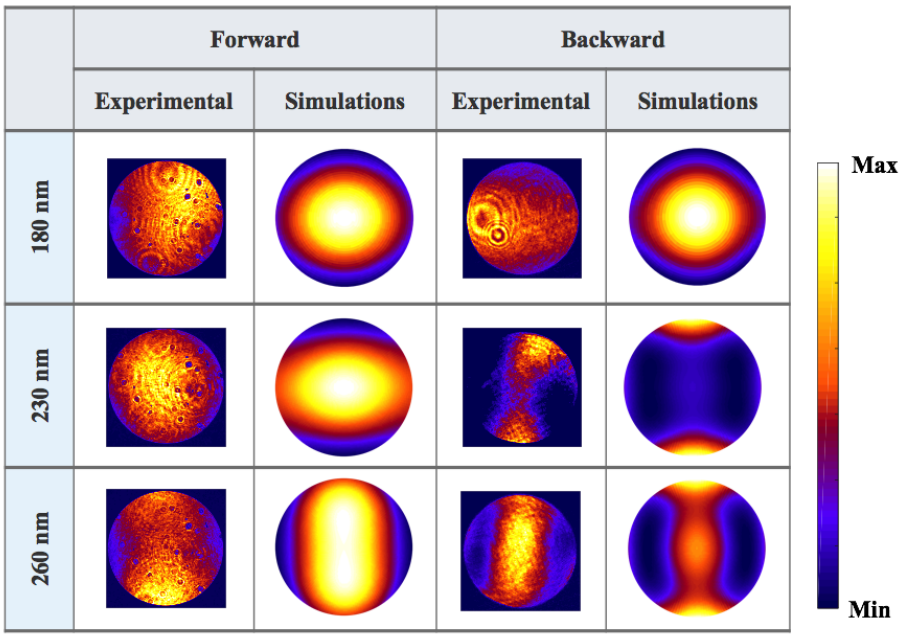

FIGURE 5.8: Measured and calculated SHG radiation patterns of three nanoantennas with different radii: 180, 230 and 260 nm, under a polarisation angle of $\varphi = 0$. Each experimental image is normalised to its respective maximum pixel value to obtain a good contrast.

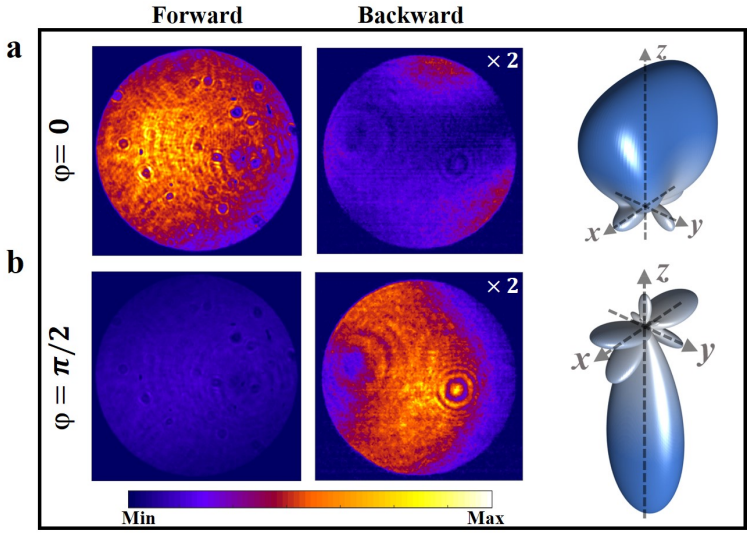

FIGURE 5.9: Forward and backward SHG radiations patterns of nanoantenna (r=210 nm) excited by two polarisation angles: (a) $\varphi = 0$ and (b) $\varphi = \pi/2$. The measured SHG radiation patterns (left) and the calculated SHG far-field radiation patterns (right) are shown in every case.

5.5 Comparison among differently oriented GaAs-based nanoantennas

The second order nonlinear response of GaAs, a non-centrosymmetric material, is anisotropic, that is $\chi^{(2)}_{ijk}$ is not invariant under rotation. The nonlinear response of GaAs-based nanoantennas significantly depends on the mutual orientation between the crystalline axes and the polarisation angle of the incident beam. In this thesis, we have shown experimentally and theoretically different features of the second-harmonic emission from GaAs-based nanoantennas grown along different crystallographic orientations. In particular, we have shown the differences of the SHG radiation patterns from GaAs-based nanoantennas grown along different crystallographic orientations. In Chapter 4, we observed a doughnut-shaped forward and backward SHG with zero normal emission from (100)-AlGaAs nanoantennas. This characteristic radiation pattern does not change with the size of the nanoantennas or the polarisation angle of the incident beam. At the beginning of this chapter we presented the SHG radiation patterns from (111)-GaAs nanoantennas, in this case non-zero forward second-harmonic emission was observed for a particular nanoantenna; while the forward SHG radiation patterns were dependent of the incident polarisation angle. After that, we studied the radiation patterns of (110)-GaAs nanoantennas, demonstrating normal forward and backward SHG for several cases. Normal SHG is important since it increases the collection efficiency, allowing us to explore more applications for GaAs-based nanoantennas.

We finalise this chapter by performing simulations of the SHG from GaAs nanoantennas with different crystallographic orientations. To facilitate the comparison, only the crystallographic orientations were changed while all the other parameters remained constant. We considered a GaAs nanoantenna with r = 210 nm and h = 400 nm, placed in a homogeneous host medium with a refractive index n = 1.44, and illuminated by a fundamental beam with a wavelength λ = 1450 nm. Three crystallographic orientations of the GaAs nanoantennas were considered: (100), (111) and (110). The dependence of the SHG efficiency on the incident polarisation angle φ is shown in Figure 5.10a. The SHG of the (100)-GaAs nanoantenna has a minimum at $\varphi = 0°$ and a maximum at $\varphi = 45°$, as the angle increases from 45° to 90° the SHG goes from

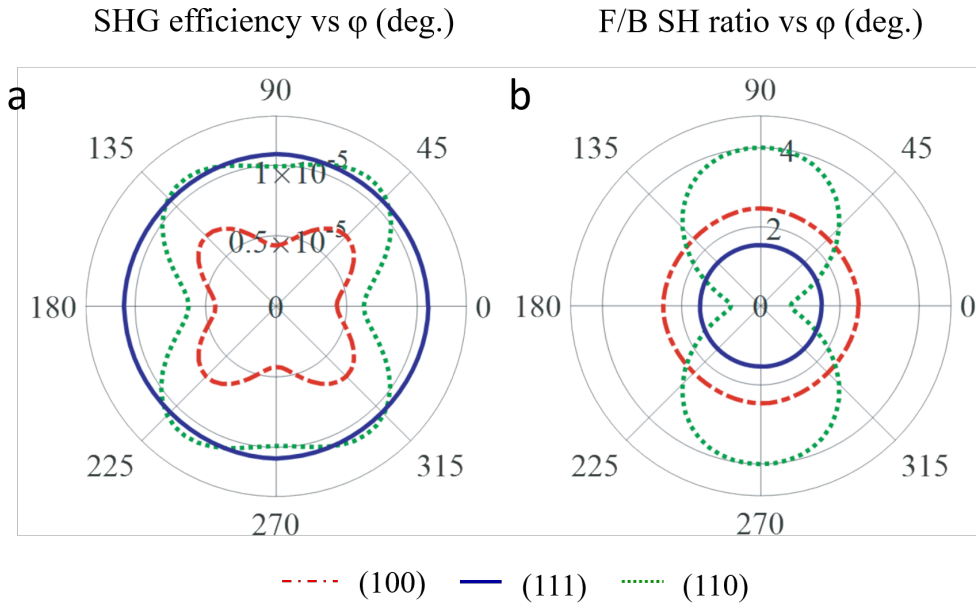

FIGURE 5.10: Calculated polar plots of (a) total SHG efficiency and (b) forward to backward SHG ratio, as a function of the incident polarisation angle φ. In the simulations, GaAs nanoantennas (r = 210 nm, h = 400 nm) with different crystalline plane orientations were considered: (100) in red, (111) in blue and (110) in green.

a maximum to a minimum. This behaviour is in agreement with the one previously observed in Section 3.6 (see Figure 3.9). The behaviour is repeated every 90°, giving a four-fold SHG symmetry. The SHG of a (111)-GaAs nanoantenna is constant for any incident polarisation angle, as it was previously shown in Section 5.3.1 (see Figure 5.4). The SHG of a (110)-GaAs nanoantenna has a minimum at $\varphi = 0°$, the efficiency increases with the polarisation angle until $\varphi = 45°$, where the SHG remains almost constant as the angle φ increases. At $\varphi = 135°$ the SHG starts to decrease presenting another minimum at $\varphi = 180°$. After $\varphi = 180°$, the behaviour is repeated giving a two-fold SHG symmetry. Also, the forward to backward SHG ratio was calculated as a function of the polarisation angle, for three crystallographic orientations. The calculations are shown in Figure 5.10b. In this case, the forward to backward SHG ratio of the (100)- and (111)-GaAs nanoantennas remains constant for any incident polarisation angle. While high SHG directionality of the (110)-GaAs nanoantenna can be tuned by the incident polarisation angle. The backward SHG dominates over the forward SHG for $\varphi = 0°$, while the forward SHG dominates over the backward SHG for $\varphi = 90°$.

5.6 Conclusions

In this chapter, we studied the influence of the crystallographic orientations of GaAs nanoantennas in their nonlinear response. First, we studied the SHG of (111)-GaAs nanoantennas and demonstrated, theoretically and experimentally, non-zero normal SHG. We demonstrated SHG efficiencies that are independent on the incident polarisation angle and SHG radiation patterns that are dependent on the incident polarisation angle. Next, we studied the forward and backward SHG of (110)-GaAs nanoantennas, demonstrating control over the forward and backward SHG by changing the radius of the nanoantennas and the incident polarisation angle. Most importantly, we demonstrated nonlinear unidirectional and normal emission. The switching between all-forward and all-backward SHG was achieved optically, *i.e.* without introducing physical changes to the system. Last but not least, we compared the SHG of GaAs nanoantennas with three crystallographic orientations, which demonstrates the unique capabilities of (110)-GaAs nanoantennas to control the SHG at the nanoscale.

Our results pave the road towards new and practical applications in nonlinear photonics, such as ultrathin nonlinear mirrors based on dielectric metasurfaces where the fundamental beam and the harmonic emission are directed in opposing directions. The GaAs nanoantennas can be also used in nonlinear nanophotonics technologies with applications in nanoscale light sources, tunable routing elements, optical switches, etc.

CHAPTER 6

Infrared imaging in nonlinear (110)-GaAs metasurfaces

6.1 Introduction

The previous chapters were dedicated to fundamental studies of SHG using individual GaAs-based nanoantennas with different crystallographic orientations. The SHG intensity, polarisation and directionality were studied and controlled under the excitation of multipolar Mie-type resonances within the nanoantennas. The control over the properties of the second-order emission allow us to explore the potential application of GaAs nanoantennas arrays, also known as metasurfaces.

Metasurfaces consist of structured arrays made up of resonant nanoantennas which provide resonant enhancement of the incoming electromagnetic fields. In addition, the in-plane coupling between the individual nanoantennas can lead to a complex optical response of metasurfaces (see Section 1.5). In our previous studies, we observed zero normal SHG of individual (100)-AlGaAs nanoantennas (see Section 4.3.3); meanwhile vanishing zero-order diffraction SHG has been reported in metasurfaces composed of (100)-GaAs nanoantennas (*111*). In the case of individual (110)-GaAs nanoantennas, our studies showed non-zero normal SHG and controllable SHG directionality (see Section 5.4). These results anticipate attractive properties of (110)-GaAs metasurfaces to be applied in the nonlinear optical regime.

Infrared imaging is a technique used to capture invisible infrared images and convert them, through different physical mechanism, into visible ones. In this chapter, we used GaAs metasurfaces to perform infrared imaging by using a nonlinear optical process: SFG. First

we analyse the second- and third-order nonlinear emissions generated by (110)-GaAs metasurfaces, including SFG. Then, we demonstrate up-conversion of an infrared signal beam to the visible spectrum, assisted by the use of a strong pump beam and realised through the SFG nonlinear process. Even more, when an infrared image of a target (in the signal beam) and a pump beam simultaneously illuminate the metasurface, a visible image of the target is produced at the output of the metasurface. The SFG nonlinear mixing process enables the realisation of visible images from the target, which can be resolved in the femtosecond regime and can be detected by a conventional CCD camera.

6.2 Design of GaAs metasurface

SHG can be seen as the degenerate case of the SFG process (see Section1.3.2), therefore similar approaches to the ones used earlier in this thesis can be used to study SFG. In this section, we use numerical simulations to design resonant (110)-GaAs metasurfaces and enhance the nonlinear optical response of the metasurfaces. From the obtained results, the corresponding (110)-GaAs metasurfaces are fabricated.

6.2.1 Linear response of GaAs metasurface

We start this chapter by engineering the linear optical properties of (110)-GaAs metasurfaces using numerical calculations. The numerical 3D electromagnetic calculations were performed using the finite element method in COMSOL Multiphysics. The GaAs metasurfaces, composed of an array of GaAs disk nanoantennas embedded within a homogeneous medium with $n = 1.44$, are simulated by implementing Floquet boundary conditions to mimic an infinite 2D periodic structure. The dispersion of the GaAs permittivity was taken from tabulated data previously reported (*98*).

The metasurfaces are designed through geometric tuning to support strong resonances at both signal and pump wavelengths, thus increasing the conversion efficiency of the SFG process. Several geometric parameters can be optimised to obtain strong resonances in the metasurface, *e.g.* the radius r and height h of the nanoantennas, and the periodicity P of the

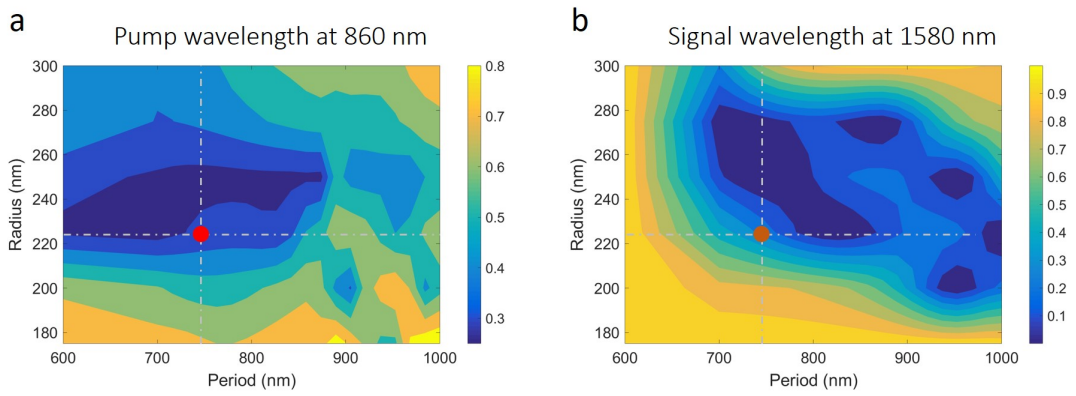

FIGURE 6.1: Calculated two-dimensional transmission plot (colour scale at right side) as a function of the array periodicity of the GaAs metasurface and GaAs nanoantenna radius. The calculations were performed at a fixed wavelength of (a) 860 nm (pump) and (b) 1580 nm (signal). The nanoantenna height is fixed at 400 nm. Double resonant behaviour, at the pump and signal wavelengths, is achieved in a metasurface with periodicity of 750 nm and nanoantenna radius of 225 nm, indicated by the red and orange dots.

array; while the wavelengths of the pump and signal beam can be tuned around the spectral region of interest. In our calculations, the height of the nanoantennas and the wavelengths of the excitation beams were fixed. The height of the nanoantennas was fixed at 400 nm, while the wavelength of the pump and signal beams were fixed at 860 nm and 1580 nm, respectively. These wavelength were chosen according to the potential application of GaAs metasurface for infrared imaging. When infrared imaging is performed, laser diodes emitting at 860 nm could be used as the pump laser source to up-convert the near-infrared radiation (1-3μm) into the visible spectrum. The near-infrared radiation is created by hydroxyl ion emissions in the upper atmosphere, a phenomenon that is called *atmospheric night glow*. Among the range of wavelengths in the near-infrared region, we decided to work with a signal beam at 1580 nm since its frequency-mixing (SFG) with 860 nm generates the radiation of green photon, where the human eye has a maximum sensitivity. The transmission map obtained when varying the metasurface period from 600 to 1000 nm, and the nanoantennas radius from 175 to 300 nm is shown in Figure 6.1. The areas of interest in this figure are the low transmission areas indicated by blue coloured regions, which correspond to the strong resonant behaviour of the metasurface. Figure 6.1a was calculated considering an incident wavelength at 860 nm (pump), while Figure 6.1b was calculated considering an incident wavelength at 1580 nm

(signal); in both cases normal illumination was considered. In Figure 6.1a, strong resonances are observed in metasurfaces with periodicities in the range of 600 to 850 nm and radius in the range of 220 to 260 nm, approximately. In the case of Figure 6.1b, strong resonances are observed for metasurfaces with periodicities in the range of 700 to 850 nm and radius in the range of 220 to 280 nm, approximately. Thus, the transmission maps shown in Figure 6.1 offer a range of geometric parameters where strong resonances are observed simultaneously in the two wavelengths of interest. For example, by observing the vertical white dotted line in Figure 6.1a and b (at P = 750 nm) strong resonances are observed simultaneously for nanoantennas radii between 220 and 280 nm. The pair of geometric parameters (P and r) indicating a double resonant behaviour of the metasurface were used to simulate the SFG emission. According to a strong double resonant behaviour and maximum SFG normal emission, the final design consists of a GaAs metasurface with P = 750 nm, r = 225 nm (see red and orange dots in Figure 6.1) and h = 400 nm.

6.2.2 Field spatial profiles

The spatial field profiles of the pump, signal and SFG are calculated in the designed GaAs metasurface (h = 400 nm, r = 225 nm and P = 750 nm). The nonlinear response of the metasurface is obtained in a two steps approach. First, the linear problem at the incident frequencies is calculated. Then, the problem at the SFG frequency is solved by employing the nonlinear polarisation as the source of the SFG field. Due to the zinc blende GaAs crystal structure, we can define the i-th component of the nonlinear polarisation as $P_i(\omega_3) = 2\epsilon_0\ \chi^{(2)}_{ijk}$ $[E_j(\omega_1)E_k(\omega_2)+E_k(\omega_1)E_j(\omega_2)]$ with $i \neq j \neq k$, where ϵ_0 is the vacuum permittivity. $E_j(\omega_1)$ is the j-th component of the electric field at the angular frequency ω_1 corresponding to a wavelength of 1580 nm, $E_k(\omega_2)$ is the k-th component of the electric field at the angular frequency ω_2 corresponding to a wavelength of 860 nm, and $P_i(\omega_3)$ is the i-th component of the nonlinear polarisation field at the angular frequency ω_3 corresponding to a wavelength of 557 nm.

The distribution of the electromagnetic field in the metasurface was calculated for the pump, signal, and SFG fields, as shown in Figure 6.2. In each case, the spatial profile of the electric

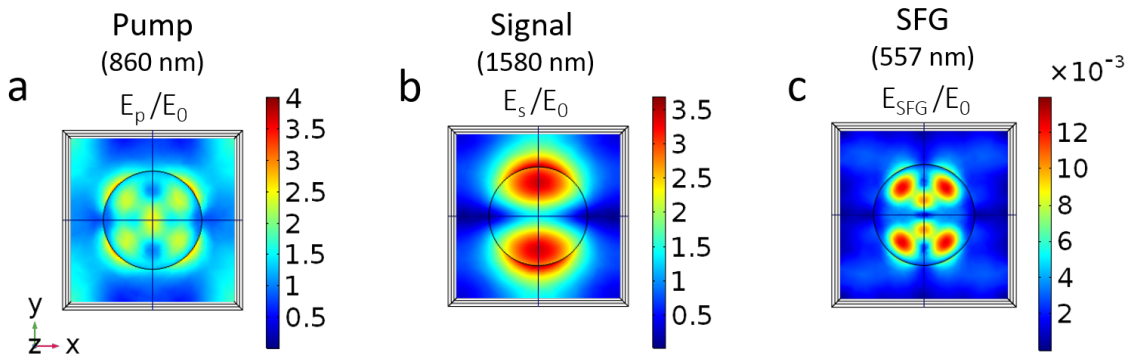

FIGURE 6.2: Calculated electric field amplitudes in the *xy*-plane of a GaAs nanoantennas with $r = 225$ nm and $h = 400$ nm at (a) 860 nm pump wavelength, (b) 1580 nm signal wavelength and (c) 557 nm SFG wavelength. The calculations were performed in COMSOL Multiphysics by implementing Floquet boundary conditions to mimic an infinite 2D periodic structure ($P = 750$ nm) and considering *y*-polarised pump and signal beams.

field is shown in the *xy* plane of a unitary cell disk nanoantenna. The spatial field profile of the pump is shown in Figure 6.2a. A maximum enhancement of about 2 times, with respect to the incident field, is exhibited according to its resonant behaviour (see Figure 6.1a). The spatial distribution of the pump field suggests the excitation of a quadrupolar mode. Multipolar decomposition of the total scattering from the metasurface corroborates the contribution of a strong electric quadrupolar mode, followed by a magnetic quadrupolar mode at the pump wavelength (860 nm). The field spatial profile of the signal, illustrated in Figure 6.2b, shows a field enhancement of as much as three times, with respect to the incident field. The spatial distribution of the signal field suggests the excitation of a dipole mode. Multipolar decomposition of the total scattering from the metasurface corroborates the contribution of a strong magnetic dipole mode followed by an electric dipole mode at the signal wavelength (1580 nm). The distribution of the induced SFG electric field is shown in Figure 6.2c. The spatial distribution of the SFG field resembles a quadrupolar mode, suggesting stronger coupling of the sum-frequency field with the pump than with the signal beam. However, a combination of magnetic and electric modes describes the spatial distribution of the sum-frequency field and further calculations are required to quantify the mode overlap of the nonlinear field with the pump and signal beams.

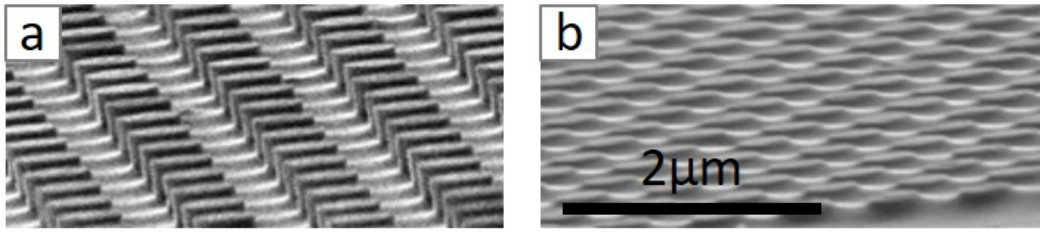

FIGURE 6.3: Oblique scanning electron microscopy images of a region of the GaAs substrate used in the fabrication (a) before the transfer, with the fabricated GaAs array on the top of it and (b) after the transfer.

6.2.3 Fabrication of GaAs mestasurface

According to the design obtained in Section 6.2.1, arrays of GaAs nanoantennas with h = 400 nm, r = 225 nm and P = 750 nm were fabricated. First, a GaAs substrate wafer oriented in the (110)-direction was used to perform planar growth of AlAs and GaAs epitaxial layers using MOCVD. The first AlAs layer was used as a lift-off buffer layer, while the GaAs layer was used to obtain arrays of single-crystalline GaAs disk nanoantennas. The nanoantenna arrays were defined using electron-beam lithography and sequential inductively coupled plasma etching (see Figure 6.3a). Next, the nanoantenna arrays were bonded to a BCB layer, followed by its curing and bonding to a thin glass substrate. Finally, the glass substrate with the GaAs nanoantennas arrays embedded in the BCB layer was peeled off from the main GaAs wafer (see Figure 6.3b). More details of the fabrication procedures can be found in Sections 2.4 and 5.2. The fabricated metasurfaces consist of GaAs nanoantennas square arrays of different sizes, embedded in a BCB layer and lying upon a glass substrate. The sizes of the fabricated metasurfaces were: 30 x 30 μm, 55 x 55 μm and 70 x 70 μm.

6.3 Optical characterisation of GaAs metasurface

In this section, I present the linear and nonlinear characterisations of the GaAs metasurfaces, emphasising on the SFG process. At the end of this section, the application of the metasurfaces to transform an infrared image into the visible spectrum is presented and discussed.

6.3.1 Linear characterisation

The linear transmission of the GaAs metasurface was measured using a white light spectroscopy setup. The setup was built based on the *Köhler illumination* which creates a uniform and grainless illumination across the field of view, despite the use of a non-uniform brightness lamp. Light is collected from the near side of the halogen lamp using a collector lens (L1). The collector lens focuses the light from the source on the back focal plane of the condenser lens (L2). The condenser lens (f=30 mm) transforms the focused light, according to the Fourier transform, to a plane collimated beam. As a result, the sample focal plane is evenly illuminated as illustrated in Figure 6.4. A polariser and two diaphragms are inserted in the optical path of the *Köhler illumination*. The polariser (P) transforms the unpolarised light from the lamp source into a linear polarisation state. The first diaphragm (D1), also called field diaphragm, controls the area of the sample being illuminated *i.e.* the field of illumination on the sample plane, without affecting the angle of the illumination. The second diaphragm (D2), so called condenser aperture, controls the illumination angle. When the condenser aperture is narrowed down, the collimated beams which intersect the sample get progressively cut-off. Consequently the light cone angle which illuminates the sample is decreased and the light illuminating the sample further resembles a plane wave. However, in such case, the intensity of the light in the system drops. An objective lens (20X Mitutoyo Plan Apo NIR with a NA of 0.40) collects the transmitted light and builds the image of the sample. By placing a rectangular knife-edge aperture at the focus of two confocal lenses (L3 and L4 both with f=75 mm) the forward scattering light is filtered out from the optical system. The light transmitted through the sample is collected by the lens L4 and is finally coupled to an optical fiber. The optical fiber is connected to either a visible spectrometer (Ocean Optics 65000) or to an infrared one (Princeton Instruments Acton SP 2300 monochromator with Andor DU490A-1.7 InGaAs array detector), detecting the corresponding spectrum from the sample. A flip mirror is used after the lens L4 to see the image of the sample with a CMOS camera (Thorlabs, DCC1545M).

Using the spectroscopy setup explained above, the transmission spectrum of the GaAs metasurface was measured, as schematically depicted in Figure 6.5a. In our measurements the

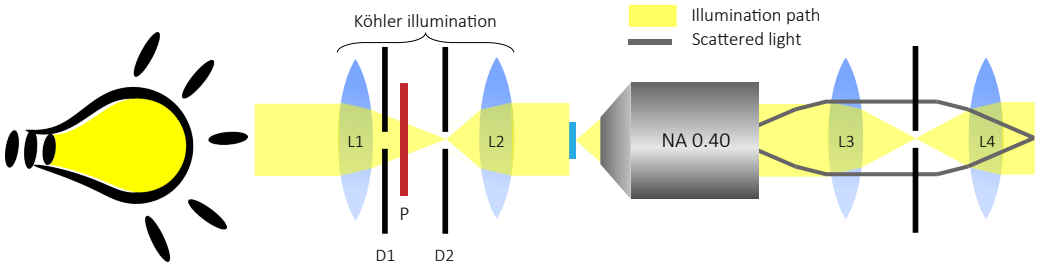

FIGURE 6.4: Schematic of optical system used to measure transmission spectra from metasurfaces. Light is collected from a lamp by a collector lens (L1) and focused in the rear focal plane of a condenser lens (L2), creating a plane uniform light beam that illuminates the metasurface. The diaphragms in the optical system control the illumination area on the metasurface plane and the light intensity reaching the metasurface (*Köhler illumination*). The light transmitted through the metasurface is collected by an objective lens and transmitted to a pair of confocal lenses (L3 and L4).

condenser aperture was nearly closed (diameter of the iris aperture was ≈ 2 mm) to reduce the illumination angles to $\pm 3°$. This aperture ensures a near-normal plane wave illumination of the metasurface in accordance to the conditions considered earlier in the calculations (see Figure 6.1). The visible and near-infrared transmission spectra were measured as a function of the wavelength, as shown in Figures 6.5b and c, respectively. Figure 6.5b shows a transmission spectrum with three strong resonances (dips) centred around 580, 770 and 885 nm. The resonant behaviour of the metasurface at the pump wavelength (860 nm) is indicated by a red dot in Figure 6.5b. In addition, a resonant behaviour is observed around the SFG wavelength (550 nm), indicated by a green dot. Figure 6.5c shows a transmission spectrum with two strong resonances centred around 1250 and 1630 nm and a small resonance centred around 1385 nm. The resonant behaviour of the metasurface around the signal wavelength (1580 nm) is indicated by an orange dot in Figure 6.5c. The transmission spectra of the metasurface (see blue dots in Figure 6.5b and c) exhibited periodic fringes due to Fabry-Perot interference. This interference was introduced by two thin glasses, glued to each other, which constitute the substrate of the GaAs metasurfaces. An average filter function from Matlab was used (see black line in Figure 6.5b and c) to smooth the measured transmission spectra.

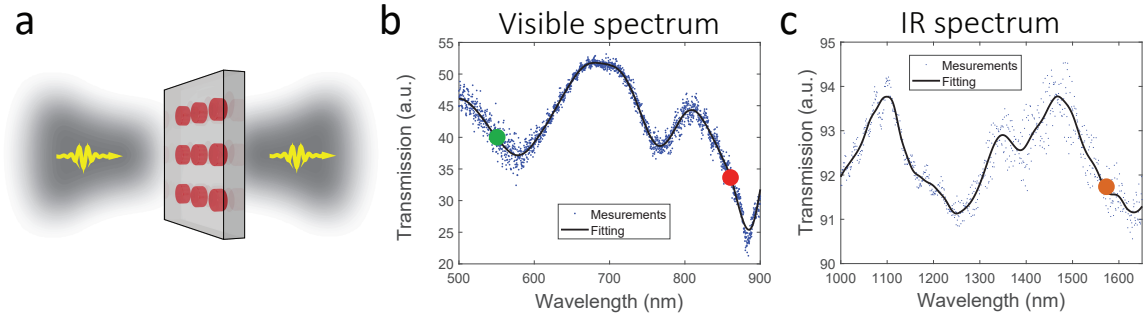

FIGURE 6.5: (a) Schematic of a metasurface illumined by light waves producing scattering of light. Measured transmission spectra of GaAs metasurfaces in the (b) visible and (c) near-infrared spectrum. The wavelength position of the SFG, pump and signal is indicated by the green, red and orange dots, respectively.

6.3.2 Nonlinear characterisation

6.3.2.1 Optical system

The optical system used for the nonlinear characterisation of the GaAs metasurface is described below. The output of a tunable mode-locked Ti:Sapphire laser (Chameleon, Ultra II with a repetition rate of 80 MHz) is split into two beams to obtain a pump and a signal beam. The pump beam is delivered by the tunable Ti:Sapphire laser with a central wavelength that can be tuned from 680 to 1080 nm. The signal beam is obtained from an Optical Parametric Oscillator (OPO) (Coherent, Compact OPO with a repetition rate of 80 MHz), coupled to the main oscillator (Chameleon, Ultra II). When coupled to the OPO, the tuning wavelength of the main oscillator is reduced, from 740 to 880 nm, while the wavelength of the signal beam has a tuning range of 1000-1600 nm. The output beams are sent through different optical paths, one of which passes through an optical delay line as observed in Figure 6.6. The temporal duration of the pump and signal pulses was measured using the frequency-resolved optical grating (FROG) method, across a range of wavelengths. In the case of the pump pulse laser, the beam was tuned from 800 to 900 nm obtaining an average temporal duration of 181 $\pm$ 10 fs. For the signal pulse laser, the temporal duration was measured from 1520 to 1560 nm obtaining an average temporal duration of 152 $\pm$ 4 fs. The output polarisation of the pump and signal beam (horizontally linearly polarised) was controlled separately by two achromatic

half-wave plates (Thorlabs AHWP10M-980 and AHWP05M-1600, respectively). The image of a target is encoded in the signal beam through an imaging system which is described in Section 6.4. An optical delay line, consisting of two mirrors sitting at about 90 degrees to each other and mounted in a travel translation stage (Thorlabs, PT1/M), extends or shortens the length of the pump beam path without changing its alignment. The temporal synchronisation between the pump and signal pulses was controlled by tuning the optical delay line. The signal and pump beams are spatially combined by a dichroic mirror (DM), afterwards the two beams propagating collinearly to each other are focused at the same position on the GaAs metasurface by a plano-convex lens (L1 with f=50 mm). The generated frequency-mixing emissions and the transmitted pump are collected by an objective lens (100X Mitutoyo Plan Apo NIR Infinity Corrected Objective) with a NA of 0.5. The transmitted pump is filtered-out from the optical system by two short-pass filters (Fs) with a cut-off wavelength of 600 nm (Thorlabs, FESH0600). The remaining nonlinear emissions were collected by a lens (L2) and sent to a CCD camera (StarlightXpress SXVR-H9) or coupled by a lens (L3) to an optical fiber connected to a spectrometer (Ocean Optics 65000). Note that only a portion of the generated nonlinear emissions are collected by the NA of the objective lens, which has a maximum collection angle of $\approx 30^{\circ}$. An schematic of the optical system described above is shown in Figure 6.6, together with its more important optical elements.

6.3.2.2 Nonlinear emission of metasurface

In the present section, the nonlinear spectra generated by the GaAs metasurface is presented, analysed and discussed. Through all the measurements shown in this section, the imaging system (encoding the image of the target) was placed in the optical system. However, the practical use of the imaging system was prevented by placing the target outside the optical path of the signal beam. The imaging system is only used in the last part of this chapter.

The SFG intensity of the metasurface was measured by independently tuning the wavelength of the signal and pump beam around the resonances of interest (see red and orange dots in Figure 6.5b and c). First, the wavelength of the signal beam was fixed at 1510 nm and the wavelength of the pump was tuned from 830 to 880 nm, as shown in Figure 6.7a. Both

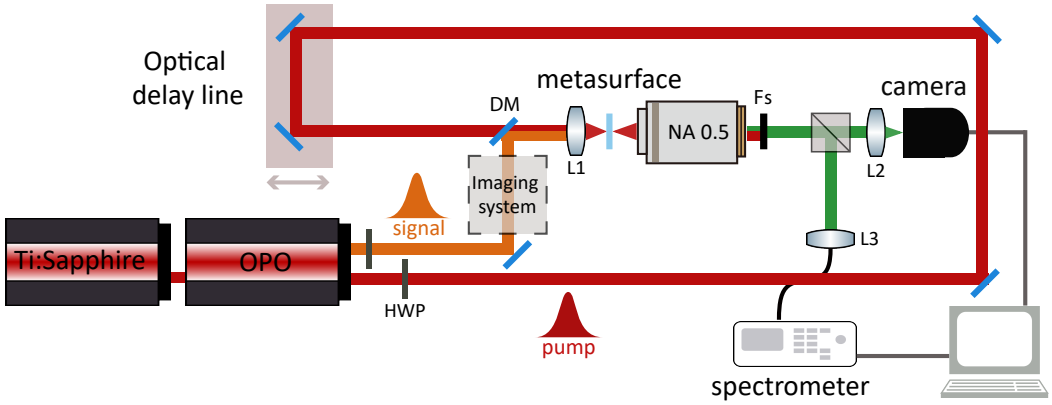

FIGURE 6.6: Schematic of optical system used to study the nonlinear emissions from the GaAs metasurface. A Ti:Sapphire laser pumps an optical parametric oscillator (OPO) cavity. At the output of the OPO cavity, two beams with the same polarisation and repetition rate, but different wavelength are used as the signal and pump excitation beams. The polarisation of the signal and pump beams is controlled by half-wave plates (HWP). The signal beam encodes the information of a target (through the imaging system). The pump pulse is temporally synchronised to the signal pulse by an optical delay line. The signal and pump beams are spatially combined by a dichroic mirror (DM) and focused by a lens (L1) at the same position on the GaAs metasurface. The nonlinear emissions generated by the GaAs metasurface, together with the transmitted excitation beams are collected by an objective lens with a NA of 0.5. At the back aperture of the objective lens, two short-pass filters (Fs) are used to filter-out the transmitted excitation beams. The remaining nonlinear emissions are either focused (by the lens L2) in the CCD of a visible camera, or coupled (by the lens L3 and a 3D stage not shown in this figure) to an optical fibre connected to a spectrometer. In the schematic, the pump and signal beam are not spatially overlapped only for visualisation purposes.

beams were linearly polarised along the horizontal direction. The spectrum in Figure 6.7a shows the emission of the SFG from 534 to 554 nm, with a maximum efficiency at 546 nm, corresponding to an excitation pump beam at 860 nm. After exhibiting a maximum at 549 nm, the SFG intensity decreases with the increase of the pump wavelength. The use of a pump beam with a wavelength longer than 880 nm is limited by our laser system. The weak peak observed around 570 nm is generated by a third-order nonlinear process, details of this third-order nonlinear process are discussed later on in this section. Next, the wavelength of the signal beam was tuned from 1470 to 1570 nm, while maintaining the pump beam fixed at 860 nm (see Figure 6.7b). The wavelength of the pump beam was chosen according to the maximum SFG observed in Figure 6.7a. Figure 6.7b shows the SFG emission from

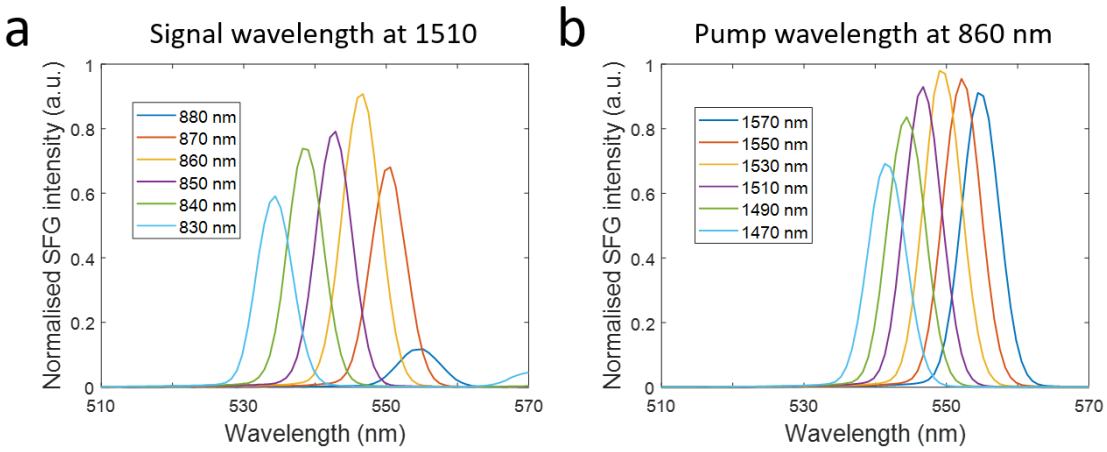

FIGURE 6.7: Normalised SFG spectra of GaAs metasurface, measured when tuning the wavelength of (a) the pump beam from 830 to 880 nm (signal beam wavelength fixed at 1510 nm) and (b) the signal beam from 1470 to 1510 nm (pump beam wavelength fixed at 860 nm).

541 to 554 nm, with a maximum at 549 nm, corresponding to a signal beam at 1530 nm. After the maximum at 549 nm, the SFG intensity gradually decreases with the increase of signal wavelength. Through all these measurements, the average power of the pump and signal beams, measured right before the metasurface, was kept constant at 18 and 14 mW, respectively. The power was controlled by a continuously variable neutral density filter placed in the optical path of each beam. The temporal overlap between the pump and signal pulses has a small dependence with the wavelength of the excitation beams, consequently the optical delay line was adjusted in each measurement to obtain the maximum SFG. As can be seen in Figures 6.7a and b, the optimized SFG intensity takes place when the metasurface is excited by a pump beam at 860 nm and a signal beam at 1530 nm. This behavior is explained by the near-field enhancement of the excitation beams, when the metasurface is resonantly excited (see Figure 6.5b and c) at these excitation wavelengths.

According to the previous results, the nonlinear response of the GaAs metasurface was studied under the excitation of signal and pump beams at the optimised wavelengths (pump at 860 nm and signal at 1530 nm) using an average power of 10 mW in each beam, measured before the metasurface. The visible nonlinear spectrum of the metasurface is shown in Figure 6.8a, characterised by two strong nonlinear emissions centred at 430 and 550 nm. The emission at

430 nm is originated by the SHG of the pump ($2\omega_p$), while the 550 nm emission is originated by the SFG process ($\omega_s + \omega_p$). The wavelengths of the SHG and SFG are smaller than the periodicity of the metasurface (*P* = 750 nm), thus diffraction of the nonlinear emissions is expected. The diffraction of the SHG and SFG emissions was corroborated by performing Fourier plane imaging. In both cases, strong zero and first diffraction orders were observed, while the collection of higher diffraction orders was prevented by the NA of the objective (see Figure 6.6). In the spectra shown in Figure 6.8a, the optical system was aligned to the maximum SFG intensity *e.g.* by aligning the position of the collecting objective and the coupling of the optical fiber to the SFG wavelength. The intensities of the $\text{SHG}_{2\omega_p}$ and SFG, and their intensity ratio, are slightly different when the optical system is maximised to the $\text{SHG}_{2\omega_p}$ wavelength. In Figure 6.8a, the higher intensity of the $\text{SHG}_{2\omega_p}$, as compared to the SFG intensity, is unexpected due to the absorption of the material. Above the band gap of GaAs (1.42 eV, 873 nm), the absorption coefficient increases as the incident wavelength decreases. In addition, the calculations indicate stronger field enhancement of the incident signal beam, as compared to the pump beam (see Figure 6.2a and b). The higher intensity of the SHG ($\omega_p + \omega_p$) can be attributed to the full spatial overlap of the pump field with itself (see Figure 6.2a). Whereas, in the case of SFG ($\omega_s + \omega_p$) the spatial overlap between the signal and pump beams (see Figure 6.2a and b) is not complete, thereby generating a weaker SFG intensity. It is worth noting that the SFG intensity is also dependent on the spatial overlap between the excitation and SFG fields (see Figure 6.2c). Further studies can be performed to investigate the relative intensities of the nonlinear emissions. However, these studies are outside the scope of our work.

To verify the origin of the strong nonlinear emissions observed in Figure 6.8a, the power of the pump beam was gradually incremented from 2 to 20 mW with a 2 mW step, while the power of the signal beam was kept constant. The intensities of the parametric emissions were recorded and analysed in a log-log plot, as shown in Figure 6.8b. The dependency of the $\text{SHG}_{2\omega_p}$ intensity was linearly fitted to the power of the pump beam, the linear fitting indicated a slope of 2.11 ± 0.11, typical of a second-harmonic process. Similarly, the dependency of the SFG intensity was linearly fitted to the power of the pump, the linear fitting indicated a slope of 1.13 ± 0.01, typical of a sum-frequency process.

Besides the strong nonlinear emissions observed in Figure 6.8a, three additional nonlinear emissions of low intensity were recorded; their spectral positions are indicated by a start to facilitate its recognition. The first one is generated around 400 nm, close to the $SHG_{2\omega_p}$, the second one is generated around 600 nm close to the cut-off wavelength of the short-pass filter used in experiments (see details in the description of optical system), therefore it has an attenuated intensity. A third nonlinear emission is generated around 765 nm. The origin of each nonlinear emission is explained below. The nonlinear emission centred at 405 nm is originated by a FWM process ($2\omega_s + \omega_p$). To verify its origin, the emission spectrum was measured for various signal beam wavelengths. The corresponding spectra are shown in the left panel of Figure 6.8c, where the nonlinear emission is tuned from 396 to 410 nm when the signal beam wavelength varies from 1470 to 1570 nm. The spectral position of every peak in the left panel of Figure 6.8c corroborates the FWM origin of the emission centred around 405 nm. This emission creates a small shoulder on the left side of the $SHG_{2\omega_p}$ peak and therefore an asymmetry on it, as observed in Figure 6.8a. Another weak emission centred at 597 nm is observed in Figure 6.8a, due to another FWM process ($2\omega_p - \omega_s$). The physical origin of the corresponding FWM process was verified by measuring its spectrum for various signal beam wavelengths, as shown in the right panel of Figure 6.8c. In this Figure, four nonlinear emission are tuned from 590 to 596 nm, when the signal beam wavelength varies from 1570 to 1510 nm, in agreement to the expected FWM spectral positions. When the metasurface is excited by shorter wavelengths, 1490 and 1470 nm, the FWM is generated at wavelengths longer than 596 nm. These emissions are, however, completely blocked by the short-pass filter used in the optical system (cut-off wavelength of 600 nm). The spectra shown in Figure 6.8c were taken with a constant average power of 18 and 14 mW in the pump and signal beams, respectively. The intensities in Figure 6.8c are not shown as they are not comparable with the experimental conditions of Figure 6.8a. Finally, the longest nonlinear wavelength shown in Figure 6.8a corresponds to a peak centred at 765 nm, generated by the SHG of the signal beam ($2\omega_s$). The $SHG_{2\omega_s}$ spectrum was measured by removing the shortpass filter used in the optical system and turning off the pump beam. The spectrum obtained under these experimental conditions, with a single peak centred at 765 nm, was plotted together with the other nonlinear emissions generated by the GaAs metasurface, as

shown in Figure 6.8a. In summary, five parametric nonlinear emissions are generated by the GaAs metasurface. Two strong emissions were generated in the visible spectrum through a second-order nonlinear process, while three additional emissions of low intensity were generated by second- and third-order nonlinear processes, as shown by the diagram levels of Figure 6.8d. A previous study reported the generation of diverse nonlinear processes in GaAs metasurfaces *e.g.* third- and forth- harmonic generation, six-wave mixing and photoluminescence (*114*). The richness of the nonlinear processes remains as an interesting study, however in this thesis we aim to employ the enhancement of the SFG process for its potential applications in infrared imaging.

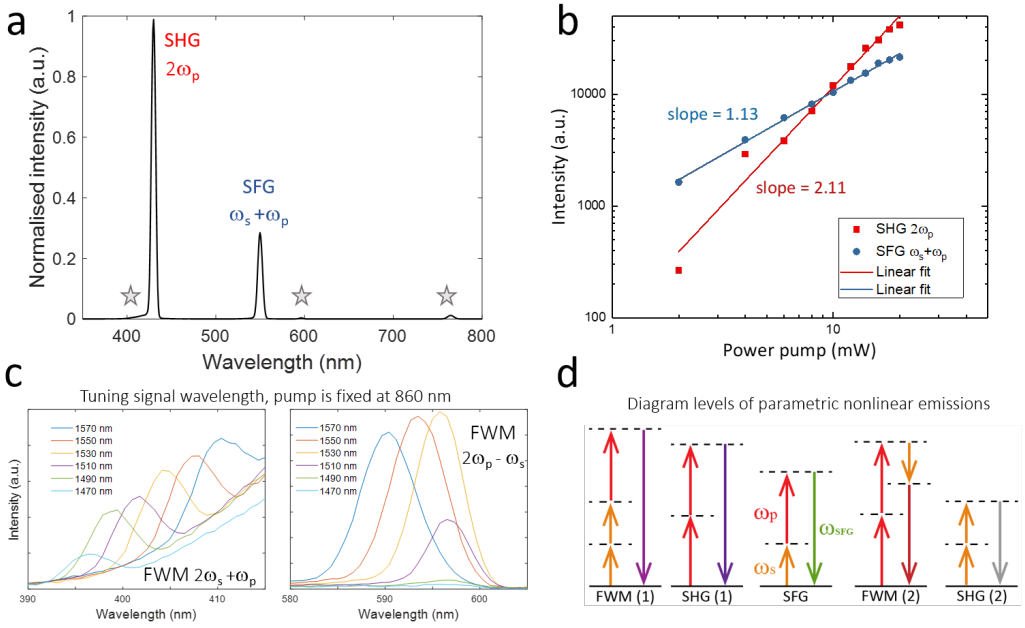

FIGURE 6.8: (a) Normalised nonlinear spectrum of GaAs metasurface. Two strong emissions centred at 430 and 550 nm are generated by the $\text{SHG}_{2\omega_p}$ (of the pump) and SFG, respectively. In addition to the two strong nonlinear emissions observed, three more emissions of low intensity are generated by the metasurface. Its spectral position, 405, 597 and 765 nm, are indicated by a star. (b) Intensity dependencies of $\text{SHG}_{2\omega_p}$ and SFG on the pump power, shown in a log-log plot. The $\text{SHG}_{2\omega_p}$ intensity depends quadratically on the pump power, while the SFG intensity depends linearly. (c) The tuning of the signal beam wavelength, between 1470 and 1570 nm, corroborates the FWM origin of the nonlinear emissions centred at 405 and 597 nm. In the right panel, the FWM process corresponds to $2\omega_s + \omega_p$. In the left panel the FWM process corresponds to $2\omega_p - \omega_s$. (d) Diagram levels of the up-converted nonlinear emissions generated by the GaAs metasurface.

The $SHG_{2\omega_p}$ is produced by the mixing of one frequency, one pulse, therefore the temporal synchronisation of the pump and signal pulses is not required for this process, as illustrated in the top of Figure 6.9a. In contrast to $SHG_{2\omega_p}$, the SFG is a frequency-mixing process that requires temporal synchronisation of pump and signal pulses, as illustrated in the bottom of Figure 6.9a. To temporally synchronise the pump and signal pulses, first is necessary to understand the pulse propagation of both beams. As previously explained (see Section 6.3.2.1), the output of a Ti:Sapphire laser was divided into two beams to obtain a pump and a signal beam. One of the two Ti:Sapphire laser beams enters the OPO cavity travelling back and forward inside the resonator cavity, around 167 cm more than its pair beam, to generate a tunable near-infrared output beam at the output of the OPO cavity. In this thesis the output beam from the OPO cavity is named signal beam. According to the configuration described, the signal and pump beam have different optical paths, producing a time delay (Δt) between the signal and pump pulses. The temporal synchronisation of the pulses at the metasurface plane was achieved by matching the optical path length of both beams. The pump beam travelled a long distance, as shown in Figure 6.6, to compensate for the additional distance traveled by the signal beam inside the OPO cavity, thus matching the optical paths of both excitation beams at the metasurface plane. The optical delay line shown in Figure 6.6 finely adjusts the path length of the pump beam, allowing for precise control of the time delay between the pump and signal pulses. The spectra of the up-converted nonlinear emissions generated by the GaAs metasurface was measured as a function of the time delay, as illustrated in Figure 6.9b. The $SHG_{2\omega_p}$ is observed at any time delay, while the strongest SFG emission is observed at zero time delay. As the time delay increases from zero to $\pm$333 fs, the SFG intensity continuously drops until becoming negligible. According to the data presented in Figure 6.9b, the temporal duration of the SFG emission was measured by plotting the SFG intensity as a function of the time delay, as shown in Figure 6.9c. The measured temporal duration of the SFG emission was 267 fs. This value is comparable to the temporal duration of the convoluted pump and signal pulsed beams (217 fs), the differences among the two values can be explained by dispersive effects. Short exposures times are required in the study of ultra-dynamic mechanisms, therefore the SFG emission could be used as a probe in the analysis of ultra-dynamic phenomena.

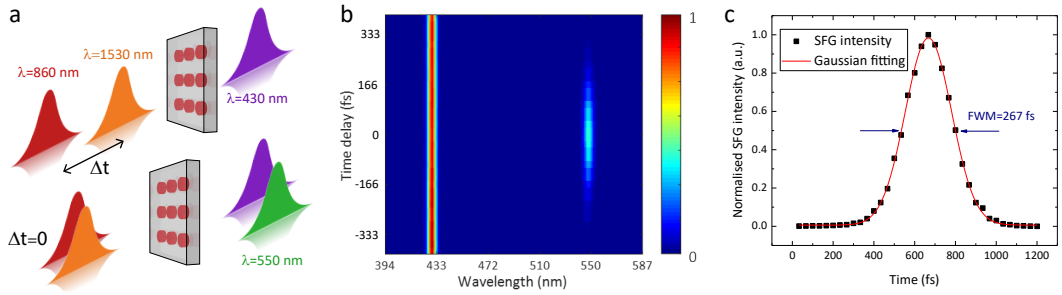

FIGURE 6.9: (a) Schematic of the nonlinear emissions generated by the metasurface at different time delays (Δt) between the pump and signal pulses. The SHG of the pump centred at 430 nm is observed at any time delay (top of figure). When the time delay is zero an additional strong nonlinear emission is generated by the GaAs metasurfaces - the SFG centred at 550 nm (bottom of figure). (b) Measured nonlinear spectrum generated by the metasurface as a function of the time delay between the pump and signal pulses. The SFG is only generated when the two pulses are temporally synchronised, while the strongest spectral emission centred at 430 nm is generated at all time delays. (c) Normalised SFG intensity as a function of the time delay, indicating the SFG emission has a duration of 267 fs.

When light propagates through a medium, its velocity is governed by the refractive index of the corresponding medium. Every time the signal or pump beam propagates through an optical component such as a lens, optical density filter or half-wave plate, the velocity of the beams changes, inducing different time delays between both pulses. For this reason and to simplify the measurements, all the optical components shown in Figure 6.6 remained in the optical system at all times, including the imaging system which is only employed to perform infrared imaging, as presented in the next section.

6.4 Near-infrared imaging in GaAs metasurface

In this section, I present the results obtained by imaging the nonlinear emissions generated by the GaAs metasurface. In particular, I demonstrate infrared imaging of a target, encoded in the signal beam, through the up-conversion of both excitation beams using resonant GaAs metasurfaces.

An imaging system was used to transfer the information of the target into the signal beam (see Figure 6.6). The imaging system consists of a Keplerian telescope that projects the real image

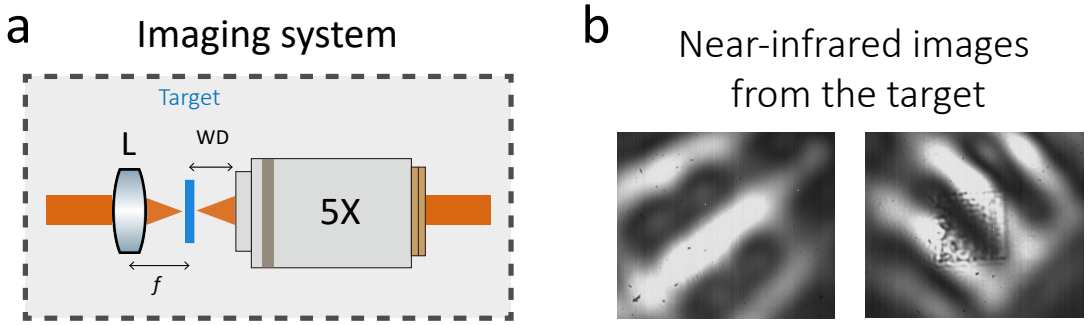

FIGURE 6.10: (a) Schematic of the imaging system used to encode the image of a target in the signal beam. The system consists of a lens (L) and an objective lens (5x magnification) placed in a confocal configuration. The target is positioned at the focal distance of the lens. (b) Images of the target acquired with an infrared camera, using only signal beam illumination. The images of the target correspond to a portion of a Siemens star. In the right panel, the target and metasurface were imaged on the same plane. The size of the imaged metasurface is 30 x 30 μm.

of the target onto the metasurface plane, as explained below. A resolution target (Thorlabs, R1L3S5P) was placed at the focal distance of a plano-convex lens (f=100 mm), the position of the target across the xy plane was controlled by a translation mount (Thorlabs, XYF1/M). After the target, a 5X objective lens (Mitutoyo Plan Apo NIR Infinity) with a NA of 0.14 was used to collect the signal beam. The objective lens was fixed at its working distance (WD) from the target resulting in a confocal configuration, as shown in Figure 6.10a. Through this imaging system, a collimated signal beam containing the real image of the target was obtained. The collimated signal beam was then focused onto the metasurface plane by a lens (see L1 in Figure 6.6) projecting the image of the target onto this plane, as shown in the left panel of Figure 6.10b. The right panel of Figure 6.10a shows the images of the target and the GaAs metasurface on the same plane. The two images in Figure 6.10b were acquired with an infrared camera (Xenics, XS-1.7-320), using only the signal beam to illuminate both the target and metasurface.

When an infrared image of the target (signal beam) and a pump beam illuminate the GaAs metasurfaces, the infrared image is transformed to the visible spectrum, through the SFG process. This process is schematically represented in Figure 6.11a, where the infrared image of a Siemens star is transformed to the visible. This process defines the operating principle of

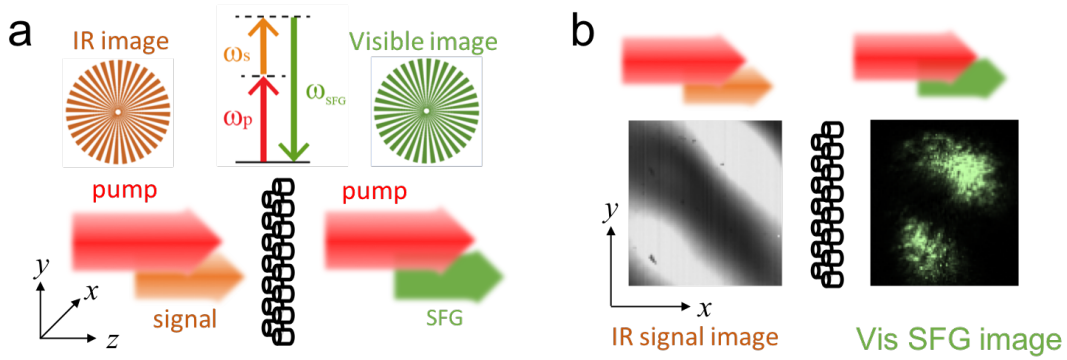

FIGURE 6.11: Concept schematic of infrared imaging. (a) An infrared signal beam, encoding the image of a target, and a pump beam illuminate the GaAs metasurface simultaneously. At the output of the metasurface a visible image of the target is obtained through the SFG emission. In the measurements, a Siemens star was used as the target image. (b) Schematic of infrared imaging using a GaAs metasurface: an infrared image of the target (in the signal beam) illuminates the GaAs metasurface, at the output of the metasurface a visible image of the target (in the SFG) is obtained. The infrared and visible images were acquired with an InGaAs and CMOS cameras, respectively.

an infrared imaging device: detect an infrared image and transform it to a visible one. In our case, a nonlinear optical process (SFG) transforms the infrared image to the visible using a GaAs metasurface, as illustrated in Figure 6.11b.

Figure 6.12 shows four SFG images of a 30 x 30 μm GaAs metasurface, captured by a CCD camera. The images correspond to different positions of the target (see Figures 6.12b-d), including the case when the target is fully removed from the path of the signal beam (see Figure 6.12a). The inhomogeneities observed in Figure 6.12a are due to fabrication defects in the metasurface, as well as inhomogeneities in the pump beam. These inhomogeneities were introduced by the additional 1.6 m distance travelled by the pump beam, with respect to the signal beam (see Figure 6.6), required to temporally synchronize both pulses. Nevertheless, when the target is inserted into the path of the signal beam, the spatial features of the target are preserved in the up-converted images, as shown in Figure 6.12b-d. In the measurements, an additional optical filter was used to filter out the $\mathrm{SHG}_{2\omega_p}$. The section of the Siemens star used to obtain the SFG images is shown in the right panel of Figure 6.12. Ideally, since the SFG is a coherent parametric process, all the spatial information in the SWIR image

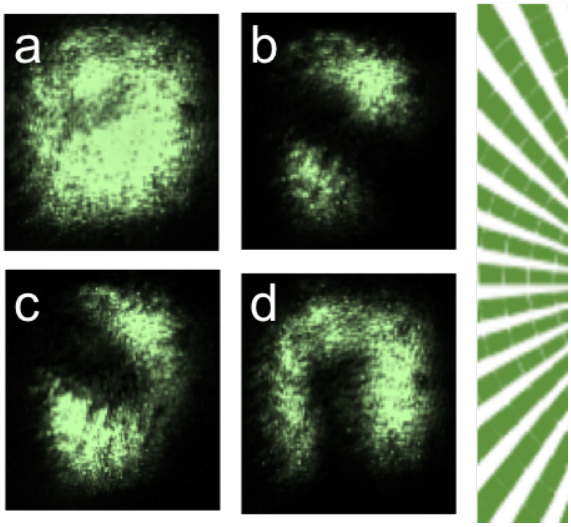

FIGURE 6.12: (a) SFG emission from GaAs metasurface and (b-d) three SFG images of the target when it is moved across the signal beam in the *xy* plane. The section of the Siemens star used in these measurements is shown in the right panel.

should be preserved to the visible. However, in the case of a metasurface the different spatial features of the target are being converted by hundreds of independent nanoantennas, which are spatially distributed within the metasurface. Therefore, any fabrication imperfections of the nanoantennas could introduce additional noise into the up-converted image (in contrast to conventional schemes). Thus, metasurfaces require good fabricated quality and uniformity to obtain clear images from the target in the visible spectrum. The visible images shown in Figure 6.12 completely disappeared when the pump and signal beam were temporally desynchronised (using the optical delay line), corroborating they are only originated by the SFG process.

6.5 Discussion

As it is the case for many other applications of GaAs metarufaces, infrared imaging requires high nonlinear conversion efficiencies. In this section, different factors influencing the conversion efficiency of the SFG process are discussed.

In general, the efficiency of nonlinear processes is enhanced by increasing the power of the incident beams. The use of high powers in plasmonic metasurfaces is limited by their low damage thresholds, while semiconductors metasurfaces have higher damage threshold when excited below its band gap. In our studies, the power of the incident beams was increased to enhance the conversion efficiency of the SFG process. While increasing the power of the pump and signal beam, the GaAs metasurface reached its saturation point. At this point, the SFG intensity started to continuously decrease and after a few seconds it became steady at low intensity levels. After observing this behaviour, the metasurface was removed from the optical system and placed in an optical microscope. Structural changes were observed in the excited metasurface, such as disordered arrangement of the GaAs disk nanoantennas, otherwise periodically arranged, and changes in the colour of the metasurface observed by the optical microscope; these changes were associated to the melting of the BCB layer. To avoid this, the damage threshold of the pump and signal beam were separately determined. First, a non-damaged metasurface was illuminated by the signal beam and the $\mathrm{SHG}_{2\omega_s}$ intensity was recorded while increasing the power of the signal beam. Then, another non-damaged metasurface was illuminated by the pump beam and the $\mathrm{SHG}_{2\omega_p}$ intensity was recorded while increasing the power of the pump beam. The damage threshold of the pump beam was determined to be lower than the one from the signal beam, indicating stronger absorption of the pump beam due to its proximity to the GaAs band gap. All the measurements presented in this chapter were performed far from the damage thresholds of the GaAs metasurface.

The size of the incidents beams, at the metasurface plane, are relevant to the SFG conversion efficiency and to the size of the target image. At the metasurface plane, the spot size of the pump and signal beams are usually different from each other. In our case, the spot size of the pump beam was smaller than the one from the signal beam. Thus, the SFG conversion efficiency is limited by the smallest spot size *i.e.* by the pump beam, since the portion of the signal beam that does not spatially overlap with the pump beam will not contribute to the SFG process. The spot size of the pump beam does not only limit the efficiency of the SFG process, but also the size of the infrared target imaged (see Figure 6.10b). Thus, even when bigger metasurfaces were available to perform infrared imaging (see Section 6.2.3), the smallest available metasurface of 30 x 30 μm was used through all the measurements

presented in this chapter. In future works, careful attention will be given to the spot size of the incident beams. Enlarged and equal spot sizes of the pump and signal beam are desirable for infrared imaging applications.

Another strategy to increase the SFG efficiency is the excitation of anapole or Fano states. As earlier discussed in this thesis (Section 1.4.2), when an anapole state is excited within individual dielectric nanoantennas increased conversion efficiencies of nonlinear processes are observed (*52*, *53*). In dielectric metasurfaces, the excitation of anapole or Fano states is characterised by sharp resonances with high quality factors (*88*, *113*, *156*) which increases the nonlinear conversion efficiencies (*88*, *113*). Also the excitation of bound states in the continuum (BIC), characterised by infinitely large quality factors, would enhance the nonlinear conversion efficiencies in nanoantennas. The excitation of quasi-BIC resonances have demonstrated enhanced SHG in AlGaAs nanoantennas (*157*). To increase the SFG conversion efficiency, future designs can explore GaAs metasurfaces supporting anapole, Fano or quasi-BIC resonances.

The spatial overlap of the incident modes with the nonlinearly generated modes can also improve the nonlinear conversion efficiencies in nanostructures. This approach has been already reported for enhanced SHG in nanoantennas (*44*) and metasurfaces (*158*), due to the spatial overlap between the fundamental and second-harmonic modes. Thus, the spatial overlap between the pump and signal modes with the SFG mode can further enhance the SFG conversion efficiency.

Finally, in view of the possible applications of GaAs metasurfaces to perform infrared imaging, it is desirable to design GaAs metasurfaces whose interference of nonlinear modes induces strong forward directionality or zero-backward intensity (also known as ‘first Kerker’ condition) of the SFG. In the linear regime, forward directionality in GaAs-based metasurfaces has been already demonstrated (*159*).

6.6 Conclusions

In this chapter enhanced SHG and SFG were demonstrated in GaAs metasurfaces, through the excitation of electric and magnetic modes at the pump and signal wavelengths. More interestingly, up-conversion of an infrared image to visible wavelengths was demonstrated, via SFG, using resonant GaAs metasurfaces and the aid of an intense pump beam. The experiments performed in this chapter show the potential applications of GaAs metasurfaces for night-vision, infrared bioimaging and sensor devices. The up-conversion of infrared images to green wavelengths, shown here, is especially beneficial for night-vision applications, since the maximum response of the eye is centred around the green wavelengths. However, further improvements are necessary for the applicability of GaAs metasurfaces, including improvements in the nonlinear conversion efficiencies. Several approaches to increase the SFG conversion efficiencies were discussed here, while many others remain to be explored.

CHAPTER 7

Conclusion and Outlook

The study of nonlinear processes in nanoantennas has been mainly focused in plasmonic and dielectric centrosymmetric materials. GaAs is a non-centrosymmetric material that had been previously used to investigate SHG in several structures including waveguides, microdisks, microrings and photonic crystals. Only recently, the favourable optical properties of GaAs have been recognised for the design of nonlinear nanoantennas. Some of these properties includes its strong quadratic nonlinearity, high refractive index and wide transparency window in the near-infrared. This thesis presents the study and control of nonlinear emissions generated by GaAs nanoantennas. To control the properties of the nonlinear emission several strategies were employed throughout this thesis, including the excitation of electric and magnetic resonances by performing geometric tuning. While this technique has been widely explored in plasmonic and other dielectric nanoantennas, in this thesis I present a unique strategy to control the properties of the nonlinear emissions: the design and employment of nanoantennas grown along different crystallographic orientations.

I demonstrated a new nonlinear microscopy technique based on SHG and THG microscopy of (100)-AlGaAs nanoantennas using CVBs. The SHG scanning maps obtained displayed four-lobe intensity patterns, where the intensity minima are aligned with the crystalline axes of the nanoantenna. The non-destructive technique was therefore, able to determine the crystalline orientation of individual AlGaAs nanoantennas. Also THG scanning maps were obtained, showing uniform doughnut-shaped intensity patterns. In nanostructures, polarisation-dependent measurements are traditionally performed with linearly polarised excitation beams, where the polarisation angle of the excitation beam is rotated in every measurement. As shown in this thesis, CVBs contain all the polarisation states of a linearly

polarised beam in a single beam, thus facilitating polarisation-dependent measurements. The introduced nonlinear microscopy technique is only limited by the homogeneity and fine alignment of the incident CVBs. Additionally, the study of SHG and THG intensity as a function of the nanoantenna size proved the generation of resonantly enhanced harmonic processes, driven by the presence of electric- and magnetic-anapole assisted states which are excited by the offset CVB illumination. The resonant behaviour of the harmonic processes was preserved despite the absorption regime of the GaAs at the harmonic frequencies.

I studied the SHG radiation patterns and polarisation states of (100)-AlGaAs nanoantennas and showed that nonlinear conversion efficiencies of the order of 10^{-4} can be achieved in these nanoantennas, such high efficiencies are promising for applications of nonlinear devices at the nanoscale. In particular, nonlinear nanoscale light sources emitting vector beams with designed polarisation states, *e.g.*, radial polarisation were demonstrated. In addition, I showed nonlinear optical magnetism in the AlGaAs nanoantennas and demonstrated continuous control in the transition between electric and magnetic nonlinear emissions by tuning the polarisation angle of the excitation beam. The electric and magnetic nonlinear emissions exhibited orthogonal polarisation patterns. This orthogonality allowed us to experimentally differentiate the induced character of the nonlinear emission, from electric to magnetic one.

The influence of GaAs nanoantennas grown along different crystallographic orientations in their nonlinear response was investigated. First, I presented the SHG of (111)-GaAs nanoantennas and demonstrated SHG emitted around the normal direction. While the SHG radiation patterns from these nanoantennas are dependent on the polarisation angle of the incident beam, the SHG conversion efficiencies are independent on the polarisation angle. Then, I presented the forward and backward SHG of (110)-GaAs nanoantennas, demonstrating control over the SHG directionality by changing the size of the nanoantennas or the polarisation angle of the incident beam. Most importantly, I presented unidirectional normal SHG in (110)-GaAs nanoantennas. The switching between all-forward and all-backward SHG was achieved all-optically, *i.e.* without introducing any physical change to the system. Finally, a comparison among the SHG from GaAs nanoantennas grown along different crystallographic

orientations was performed. This comparison showed the unique capabilities of (110)-GaAs nanoantennas to control the properties of the SHG.

I demonstrated enhanced SHG and SFG in (110)-GaAs metasurfaces, through the excitation of electric and magnetic modes at the pump and signal wavelengths. More interestingly, the conversion of an infrared invisible image to the visible spectrum was demonstrated via SFG, using GaAs metasurfaces and assisted illumination of a pump beam. The results obtained open up new opportunities for the applications of GaAs metasurfaces in night-vision goggles, infrared bioimaging and sensor devices. The obtained conversion of infrared images to green visible wavelengths is especially beneficial for night-vision applications, since the maximum response of the eye is centred around green wavelengths. However, further improvements are necessary for the applicability of GaAs metasurfaces, including the enhancement of the nonlinear conversion efficiency. Several approaches to increase the SFG conversion efficiencies were already discussed here, while many others remain to be explored.

Indeed, the conversion efficiency of nonlinear processes is a decisive factor for the application of nanoantennas in optical devices. During the research presented in this thesis, I observed several factors influencing the conversion efficiencies of second-order nonlinear processes in GaAs-based naonantennas. As presented in the introduction chapter, a common approach to increase the conversion efficiency of nonlinear processes is to produce field enhancement at the fundamental and nonlinear frequencies, driven by the excitation of Mie resonances. This approach was used in chapter 4, where a high SHG conversion efficiency was observed in nanoantennas presenting a double-resonant behaviour, at the fundamental and second-harmonic frequencies (see Figures 4.2 and 4.5). On the other hand, the excitation of specific states such as the anapole state have previously showed increased conversion efficiency of nonlinear processes (*52*). In chapter 3, I demonstrated enhancement of SHG and THG in AlGaAs nanoantennas by the presence of assisted-anapole states (see Figures 3.12 and 3.13) excited by offset CVB illumination. Meanwhile in chapter 5, the enhanced SHG is explained by the presence of anapole states (see Figures 5.3 and Figure 5.4) excited by linearly polarised beams. High conversion efficiencies are usually translated to high collection efficiencies. However, when the nonlinear emissions are generated at broad angles (see Figures 3.14 and

4.7), the collection efficiencies can significantly decrease compared to the total efficiencies. In this thesis, this limitation is solved by the use of (111)-GaAs nanoantennas (see Figure 5.5) and (110)-GaAs nanoantennas (see Figure 5.9), emitting SHG around the normal direction and therefore facilitating its collection. On the other hand, in chapter 6 I discussed the role of the spatial-overlap, between the excitation and nonlinear field, in the conversion efficiency of SFG (see Figure 6.2). Thus, in this thesis I presented several strategies to enhance the conversion efficiency of nonlinear processes, showing GaAs-based nanoantennas are promising platforms for multiple nanoscale applications requiring the manipulation and efficient generation of new frequencies.

7.1 Outlook

The study of nonlinear generation in GaAs nanoantennas by the excitation of Mie resonances is still in its infancy, and many strategies remain to be explored to achieve functional GaAs nanoantennas. For example, the generation of new frequencies has been mainly explored in individual nanoantennnas (*106*, *109*) and metasurfaces (*110*, *112*) having a simple and symmetric nanoantenna geometry - disk. Meanwhile, the design of broken symmetry nanoantennas in GaAs metasurfaces has been only recently reported (*113*). The broken symmetry design produced a sharp resonance at the fundamental frequency, thus increasing the SHG efficiency in the metasurface. However, the use of more complicated and not symmetric nanoantenna's geometries such as ellipses, triangles and many others have remained unexplored. The employment of such geometries would allow major control in the excitation and interference of Mie resonances and consequently would increase the possibilities to engineer the nonlinear response of GaAs nanoantennas. The use of designed geometries, combined with non-conventional excitation beams can further increase the control over the properties of the nonlinear emission such as its polarisation, phase and directionality. Another approach that allows to break the symmetry of disk nanoantennas is to tune the incidence angle of the fundamental beam. These studies have been previously performed in (100)-AlGaAs nanoantennas (*150*), where high polarisation and angular sensitivity of the nonlinear emission was obtained. Similar studies in GaAs-based nanoantennas having different crystallographic

orientations have remain unexplored. On the other hand, the transparency window of AlGaAs alloys can be modified by properly tuning the band gap of the material. The band gap of AlGaAs alloys increases with the Al composition, allowing a transparent behaviour of the material towards the visible spectrum. While a wider band gap enables to shift the transparency window of AlGaAs alloys, other important properties of the material including its refractive index and nonlinear susceptibilities are simultaneously affected by the presence of Al in the alloy. To understand the potential applications of GaAs-based nanoantennas at visible wavelengths, it would be important to analyse the generation of nonlinear emissions in AlGaAs alloys having different Al composition.

Fundamental studies in the nonlinear response of GaAs nanoantennas will continue to grow in the coming years, many of them driven by the quest of new applications. Therefore, I expect to see an increased number of scientific groups employing GaAs nanoantennas to achieve functional metasurfaces with efficient frequency conversions. Indeed, several studies in GaAs-based metasurfaces have been focused in the enhancement of SHG conversion efficiencies (*110*, *113*, *157*); while the potential applications of GaAs metasurfaces have just begin to be explored, demonstrating ultrathin frequency mixers (*114*), ultrafast all-optical band gap tuning (*160*), and directional lasing (*161*). Although these applications can be further investigated, I envisage many other potential applications of GaAs metasurfaces such as the realisation of ultrathin nonlinear mirrors, where the fundamental beam and the harmonic emission propagate in opposite directions. GaAs metasurfaces could also be employed in devices used to measure the spectral phase of ultrashort laser pulses, substituting the bulky optical components of such devices including lenses, prisms and nonlinear crystals. GaAs metasurfaces could be used to perform infrared imaging, as it has been shown in this thesis. By increasing the efficiency of the up-conversion process in GaAs metasurfaces, infrared imaging could be performed using continuous wave laser diodes, thus substituting many of the bulky electrical components required in current night-vision goggles for ultrathin optical metasurfaces. While all these applications rely in classic nonlinear optics, the potential applications of GaAs metasurfaces can be extended to quantum nonlinear optics. For example, GaAs metasurfaces can be employed as quantum photon sources, enabling compact and

practical platforms for the development of quantum information processing and quantum communications.

As previously mentioned, GaAs has been widely used to study bulk second-order nonlinear effects in several structures, particularly in the transparency window of the material (from around 900 nm to 16 μm) where the absorption of the excitation beams and the nonlinear emissions can be avoided. GaAs together with other III-V semiconductors materials have very high second-order nonlinearities, however applications of these materials in the nonlinear regime have been hindered due to their limited conversion efficiencies. The conversion efficiencies of III-V semiconductors have been restricted due to the challenges to achieve the phase-matching condition, explained by the lack of birefringence of these materials. In metasurfaces, the nonlinear conversion efficiencies are not limited by the phase-matching condition, thus making III-V semiconductor metasurfaces an ideal and attractive platform for nonlinear applications. In particular, the use of III-V semiconductor materials with a wide band gap offers new avenues for applications in the visible and ultraviolet spectrum, where the use of GaAs is limited by its absorption. For example, GaN and GaP are III-V semiconductors with a wide band gap, thus their use in metasurfaces could allow the realisation of light sources in the visible and ultraviolet spectrum.

Bibliography

(*1*) Mie, G. (1908). Beiträge zur Optik trüber Medien, speziell kolloidaler Metallösungen. *Annalen der Physik 330*, 377–445.

(*2*) Kasperczyk, M., Person, S., Ananias, D., Carlos, L. D. and Novotny, L. (2015). Excitation of Magnetic Dipole Transitions at Optical Frequencies. *Phys. Rev. Lett. 114*, 163903.

(*3*) Koirtyohann, S. R. and Pickett, E. E. (1966). Light Scattering by Particles in Atomic Absorption Spectrometry. *Analytical Chemistry 38*, 1087–1088.

(*4*) Turzhitsky, V., Qiu, L., Itzkan, I., Novikov, A. A., Kotelev, M. S., Getmanskiy, M., Vinokurov, V. A., Muradov, A. V. and Perelman, L. T. (2014). Spectroscopy of Scattered Light for the Characterization of Micro and Nanoscale Objects in Biology and Medicine. *Applied Spectroscopy 68*, PMID: 24480270, 133–154.

(*5*) Xiaodong, Z., Georges R., F. and Deric J., G. (2017). Interpretation of scattering by oceanic particles around 120 degrees and its implication in ocean color studies. *Opt. Express 25*, A191–A199.

(*6*) Buenzli, E. and Schmid, H. M. (2009). A grid of polarization models for Rayleigh scattering planetary atmospheres. *A&A 504*, 259–276.

(*7*) Mishchenko, M. I., Travis, L. D. and Lacis, A. A., *Scattering, Absorption, and Emission of Light by Small Particles*; Cambridge University Press: Cambridge, 2002, pp 3–5.

(*8*) Kostylev, V. I. In *Bistatic Radar*; John Wiley Sons, Ltd: 2007; Chapter 10, pp 193–223.

(*9*) Bohren, C. F. and Huffman, D. R. In *Absorption and Scattering of Light by Small Particles*; John Wiley Sons, Ltd: 2007; Chapter 4, pp 82–129.

(*10*) Kuznetsov, A. I., Miroshnichenko, A. E., Brongersma, M. L., Kivshar, Y. S. and Luk'yanchuk, B. (2016). Optically resonant dielectric nanostructures. *Science 354*.

(*11*) Radescu, E. E. and Vaman, G. (2002). Exact calculation of the angular momentum loss, recoil force, and radiation intensity for an arbitrary source in terms of electric, magnetic, and toroid multipoles. *Phys. Rev. E 65*, 046609.

(*12*) Zel'dovich, I. B. (1958). Electromagnetic interaction with parity violation. *Soviet Phys. JETP 6*, 1184–1186.

(*13*) Afanasiev, G. N. and Stepanovsky, Y. P. (1995). The electromagnetic field of elementary time-dependent toroidal sources. *Journal of Physics A: Mathematical and General 28*, 4565–4580.

(*14*) Kaelberer, T., Fedotov, V. A., Papasimakis, N., Tsai, D. P. and Zheludev, N. I. (2010). Toroidal Dipolar Response in a Metamaterial. *Science 330*, 1510–1512.

(*15*) Miroshnichenko, A. E., Evlyukhin, A. B., Yu, Y. F., Bakker, R. M., Chipouline, A., Kuznetsov, A. I., Luk'yanchuk, B., Chichkov, B. N. and Kivshar, Y. S. (2015). Nonradiating anapole modes in dielectric nanoparticles. *Nature Communications 6*, 8069.

(*16*) Lee, K.-S. and El-Sayed, M. A. (2005). Dependence of the Enhanced Optical Scattering Efficiency Relative to That of Absorption for Gold Metal Nanorods on Aspect Ratio, Size, End-Cap Shape, and Medium Refractive Index. *The Journal of Physical Chemistry B 109*, 20331–20338.

(*17*) Wiley, B. J., Chen, Y., McLellan, J. M., Xiong, Y., Li, Z.-Y., Ginger, D. and Xia, Y. (2007). Synthesis and Optical Properties of Silver Nanobars and Nanorice. *Nano Letters 7*, 1032–1036.

(*18*) Vercruysse, D., Zheng, X., Sonnefraud, Y., Verellen, N., Di Martino, G., Lagae, L., Vandenbosch, G. A. E., Moshchalkov, V. V., Maier, S. A. and Van Dorpe, P. (2014). Directional Fluorescence Emission by Individual V-Antennas Explained by Mode Expansion. *ACS Nano 8*, 8232–8241.

(*19*) Kosako, T., Kadoya, Y. and Hofmann, H. F. (2010). Directional control of light by a nano-optical Yagi–Uda antenna. *Nature Photonics 4*, 312–315.

(*20*) Alaee, R., Filter, R., Lehr, D., Lederer, F. and Rockstuhl, C. (2015). A generalized Kerker condition for highly directive nanoantennas. *Opt. Lett. 40*, 2645–2648.

(*21*) Kinkhabwala, A., Yu, Z., Fan, S., Avlasevich, Y., Müllen, K. and Moerner, W. E. (2009). Large single-molecule fluorescence enhancements produced by a bowtie. *Nature Photonics 3*, 654–657.

(*22*) Li, J. F., Huang, Y. F., Ding, Y., Yang, Z. L., Li, S. B., Zhou, X. S., Fan, F. R., Zhang, W., Zhou, Z. Y., Wu, D. Y., Ren, B., Wang, Z. L. and Tian, Z. Q. (2010). Shell-isolated nanoparticle-enhanced Raman spectroscopy. *Nature 464*, 392–395.

(*23*) Pillai, S., Catchpole, K. R., Trupke, T. and Green, M. A. (2007). Surface plasmon enhanced silicon solar cells. *Journal of Applied Physics 101*, 093105.

(*24*) Lee, S., Cha, E.-J., Park, K., Lee, S.-Y., Hong, J.-K., Sun, I.-C., Kim, S. Y., Choi, K., Kwon, I. C., Kim, K. and Ahn, C.-H. (2008). A Near-Infrared-Fluorescence-Quenched Gold-Nanoparticle Imaging Probe for In Vivo Drug Screening and Protease Activity Determination. *Angewandte Chemie 47*, 2846–2849.

(*25*) Boisselier, E. and Astruc, D. (2009). Gold nanoparticles in nanomedicine: preparations, imaging, diagnostics, therapies and toxicity. *Chem. Soc. Rev. 38*, 1759–1782.

(*26*) Debouttière, P.-J., Roux, S., Vocanson, F., Billotey, C., Beuf, O., Favre-Réguillon, A., Lin, Y., Pellet-Rostaing, S., Lamartine, R., Perriat, P. and Tillement, O. (2006). Design of Gold Nanoparticles for Magnetic Resonance Imaging. *Advanced Functional Materials 16*, 2330–2339.

(*27*) Zhou, J., Koschny, T. and Soukoulis, C. M. (2007). Magnetic and electric excitations in split ring resonators. *Opt. Express 15*, 17881–17890.

(*28*) Richtmyer, R. D. (1939). Dielectric Resonators. *Journal of Applied Physics 10*, 391–398.

(*29*) Evlyukhin, A. B., Novikov, S. M., Zywietz, U., Eriksen, R. L., Reinhardt, C., Bozhevolnyi, S. I. and Chichkov, B. N. (2012). Demonstration of Magnetic Dipole Resonances of Dielectric Nanospheres in the Visible Region. *Nano Letters 12*, 3749–3755.

(*30*) Kuznetsov, A. I., Miroshnichenko, A. E., Fu, Y. H., Zhang, J. and Lukyanchuk, B. (2012). Magnetic light. *Scientific Reports 2*, 492.

(*31*) Krasnok, A. E., Miroshnichenko, A. E., Belov, P. A. and Kivshar, Y. S. (2012). All-dielectric optical nanoantennas. *Opt. Express 20*, 20599–20604.

(*32*) Staude, I., Miroshnichenko, A. E., Decker, M., Fofang, N. T., Liu, S., Gonzales, E., Dominguez, J., Luk, T. S., Neshev, D. N., Brener, I. and Kivshar, Y. (2013). Tailoring Directional Scattering through Magnetic and Electric Resonances in Subwavelength Silicon Nanodisks. *ACS Nano 7*, 7824–7832.

(*33*) Fu, Y. H., Kuznetsov, A. I., Miroshnichenko, A. E., Yu, Y. F. and Lukyanchuk, B. (2013). Directional visible light scattering by silicon nanoparticles. *Nature Communications 4*, 1–6.

(*34*) Gomez-Medina, R., Garcia-Camara, B., Suarez-Lacalle, I., González, F., Moreno, F., Nieto-Vesperinas, M. and Jose Saenz, J. (2011). Electric and magnetic dipolar response of germanium nanospheres: interference effects, scattering anisotropy, and optical forces. *Journal of Nanophotonics 5*, 053512.

(*35*) Person, S., Jain, M., Lapin, Z., Sáenz, J. J., Wicks, G. and Novotny, L. (2013). Demonstration of Zero Optical Backscattering from Single Nanoparticles. *Nano Letters 13*, 1806–1809.

(*36*) Klein, M. W., Wegener, M., Feth, N. and Linden, S. (2007). Experiments on second and third harmonic generation from magnetic metamaterials. *Opt. Express 15*, 5238–5247.

(*37*) Nappa, J., Russier-Antoine, I., Benichou, E., Jonin, C. and Brevet, P. F. (2006). Second harmonic generation from small gold metallic particles: From the dipolar to the quadrupolar response. *The Journal of Chemical Physics 125*, 184712.

(*38*) Butet, J., Russier-Antoine, I., Jonin, C., Lascoux, N., Benichou, E. and Brevet, P.-F. (2013). Effect of the Dielectric Core and Embedding Medium on the Second Harmonic Generation from Plasmonic Nanoshells: Tunability and Sensing. *The Journal of Physical Chemistry C 117*, 1172–1177.

(*39*) Metzger, B., Hentschel, M., Lippitz, M. and Giessen, H. (2012). Third-harmonic spectroscopy and modeling of the nonlinear response of plasmonic nanoantennas. *Opt. Lett. 37*, 4741–4743.

(*40*) Hentschel, M., Utikal, T., Giessen, H. and Lippitz, M. (2012). Quantitative Modeling of the Third Harmonic Emission Spectrum of Plasmonic Nanoantennas. *Nano Letters 12*, 3778–3782.

(*41*) Palomba, S., Danckwerts, M. and Lukas, N. (2009). Nonlinear plasmonics with gold nanoparticle antennas. *Journal of Optics A: Pure and Applied Optics 11*, 114030.

(*42*) Harutyunyan, H., Volpe, G., Quidant, R. and Novotny, L. (2012). Enhancing the Nonlinear Optical Response Using Multifrequency Gold-Nanowire Antennas. *Phys. Rev. Lett. 108*, 217403.

(*43*) Aouani, H., Navarro-Cia, M., Rahmani, M., Sidiropoulos, T. P. H., Hong, M., Oulton, R. F. and Maier, S. A. (2012). Multiresonant Broadband Optical Antennas As Efficient Tunable Nanosources of Second Harmonic Light. *Nano Letters 12*, 4997–5002.

(*44*) Celebrano, M., Wu, X., Baselli, M., Grossmann, S., Biagioni, P., Locatelli, A., De Angelis, C., Cerullo, G., Osellame, R., Hecht, B., Duó, L., Ciccacci, F. and Finazzi, M. (2015). Mode matching in multiresonant plasmonic nanoantennas for enhanced second harmonic generation. *Nat. Nanotechn. 10*, 412–417.

(*45*) Zhang, Y., Grady, N. K., Ayala-Orozco, C. and Halas, N. J. (2011). Three-Dimensional Nanostructures as Highly Efficient Generators of Second Harmonic Light. *Nano Letters 11*, 5519–5523.

(*46*) Grinblat, G., Rahmani, M., Cortés, E., Caldarola, M., Comedi, D., Maier, S. A. and Bragas, A. V. (2014). High-efficiency second harmonic generation from a single hybrid ZnO nanowire/au plasmonic nano-oligomer. *Nano Letters 14*, 6660–6665.

(*47*) Shcherbakov, M. R., Neshev, D. N., Hopkins, B., Shorokhov, A. S., Staude, I., Melik-Gaykazyan, E. V., Decker, M., Ezhov, A. A., Miroshnichenko, A. E., Brener, I., Fedyanin, A. A. and Kivshar, Y. S. (2014). Enhanced Third-Harmonic Generation in Silicon Nanoparticles Driven by Magnetic Response. *Nano Letters 14*, 6488–6492.

(*48*) Melik-Gaykazyan, E. V., Shcherbakov, M. R., Shorokhov, A. S., Staude, I., Brener, I., Neshev, D. N., Kivshar, Y. S. and Fedyanin, A. A. (2017). Third-harmonic generation from Mie-type resonances of isolated all-dielectric nanoparticles. *Philosophical Transactions of the Royal Society A: Mathematical, Physical and Engineering Sciences 375*, 20160281.

(*49*) Shcherbakov, M. R., Shorokhov, A. S., Neshev, D. N., Hopkins, B., Staude, I., Melik-Gaykazyan, E. V., Ezhov, A. A., Miroshnichenko, A. E., Brener, I., Fedyanin, A. A. and Kivshar, Y. S. (2015). Nonlinear Interference and Tailorable Third-Harmonic Generation from Dielectric Oligomers. *ACS Photonics 2*, 578–582.

(*50*) Smirnova, D. A., Khanikaev, A. B., Smirnov, L. A. and Kivshar, Y. S. (2016). Multipolar Third-Harmonic Generation Driven by Optically Induced Magnetic Resonances. *ACS Photonics 3*, 1468–1476.

(*51*) Colom, R., Xu, L., Marini, L., Bedu, F., Ozerov, I., Begou, T., Lumeau, J., Miroshnishenko, A. E., Neshev, D., Kuhlmey, B. T., Palomba, S. and Bonod, N. (2019). Enhanced Four-Wave Mixing in Doubly Resonant Si Nanoresonators. *ACS Photonics 6*, 1295–1301.

(*52*) Grinblat, G., Li, Y., Nielsen, M. P., Oulton, R. F. and Maier, S. A. (2016). Enhanced third harmonic generation in single germanium nanodisks excited at the anapole mode. *Nano Letters 16*, 4635–4640.

(*53*) Grinblat, G., Li, Y., Nielsen, M. P., Oulton, R. F. and Maier, S. A. (2017). Efficient Third Harmonic Generation and Nonlinear Subwavelength Imaging at a Higher-Order Anapole Mode in a Single Germanium Nanodisk. *ACS Nano 11*, 953–960.

(*54*) Grinblat, G., Li, Y., Nielsen, M. P., Oulton, R. F. and Maier, S. A. (2017). Degenerate Four-Wave Mixing in a Multiresonant Germanium Nanodisk. *ACS Photonics 4*, 2144–2149.

(*55*) Ni, X., Ishii, S., Kildishev, A. V. and Shalaev, V. M. (2013). Ultra-thin, planar, Babinet-inverted plasmonic metalenses. *Light: Science & Applications 2*, e72–e72.

(*56*) Pors, A., Nielsen, M. G., Eriksen, R. L. and Bozhevolnyi, S. I. (2013). Broadband Focusing Flat Mirrors Based on Plasmonic Gradient Metasurfaces. *Nano Letters 13*, 829–834.

(*57*) Lin, L., Goh, X. M., McGuinness, L. P. and Roberts, A. (2010). Plasmonic Lenses Formed by Two-Dimensional Nanometric Cross-Shaped Aperture Arrays for Fresnel-Region Focusing. *Nano Letters 10*, 1936–1940.

(*58*) Aieta, F., Genevet, P., Kats, M. A., Yu, N., Blanchard, R., Gaburro, Z. and Capasso, F. (2012). Aberration-Free Ultrathin Flat Lenses and Axicons at Telecom Wavelengths Based on Plasmonic Metasurfaces. *Nano Letters 12*, 4932–4936.

(*59*) Eisenbach, O., Avayu, O., Ditcovski, R. and Ellenbogen, T. (2015). Metasurfaces based dual wavelength diffractive lenses. *Opt. Express 23*, 3928–3936.

(*60*) Hu, J., Liu, C.-H., Ren, X., Lauhon, L. J. and Odom, T. W. (2016). Plasmonic Lattice Lenses for Multiwavelength Achromatic Focusing. *ACS Nano 10*, 10275–10282.

(*61*) Avayu, O., Eisenbach, O., Ditcovski, R. and Ellenbogen, T. (2014). Optical metasurfaces for polarization-controlled beam shaping. *Opt. Lett. 39*, 3892–3895.

(*62*) Yu, N., Genevet, P., Kats, M. A., Aieta, F., Tetienne, J.-P., Capasso, F. and Gaburro, Z. (2011). Light Propagation with Phase Discontinuities: Generalized Laws of Reflection and Refraction. *Science 334*, 333–337.

(*63*) Genevet, P., Yu, N., Aieta, F., Lin, J., Kats, M. A., Blanchard, R., Scully, M. O., Gaburro, Z. and Capasso, F. (2012). Ultra-thin plasmonic optical vortex plate based on phase discontinuities. *Applied Physics Letters 100*, 013101.

(*64*) Karimi, E., Schulz, S. A., De Leon, I., Qassim, H., Upham, J. and Boyd, R. W. (2014). Generating optical orbital angular momentum at visible wavelengths using a plasmonic metasurface. *Light: Science & Applications*, e167–e167.

(*65*) Wang, F., Chakrabarty, A., Minkowski, F., Sun, K. and Wei, Q.-H. (2012). Polarization conversion with elliptical patch nanoantennas. *Applied Physics Letters 101*, 023101.

(*66*) Earl, S. K., James, T. D., Gómez, D. E., Marvel, R. E., Haglund, R. F. and Roberts, A. (2017). Switchable polarization rotation of visible light using a plasmonic metasurface. *APL Photonics 2*, 016103.

(*67*) Pors, A., Nielsen, M. G. and Bozhevolnyi, S. I. (2013). Broadband plasmonic half-wave plates in reflection. *Opt. Lett. 38*, 513–515.

(*68*) Zhao, Y. and Alù, A. (2011). Manipulating light polarization with ultrathin plasmonic metasurfaces. *Phys. Rev. B 84*, 205428.

(*69*) Panchenko, E., Cadusch, J. J., James, T. D. and Roberts, A. (2016). Plasmonic Metasurface-Enabled Differential Photodetectors for Broadband Optical Polarization Characterization. *ACS Photonics 3*, 1833–1839.

(*70*) Decker, M., Staude, I., Falkner, M., Dominguez, J., Neshev, D. N., Brener, I., Pertsch, T. and Kivshar, Y. S. (2015). High-Efficiency Dielectric Huygens' Surfaces. *Advanced Optical Materials 3*, 813–820.

(*71*) Yu, Y. F., Zhu, A. Y., Paniagua-Domínguez, R., Fu, Y. H., Luk'yanchuk, B. and Kuznetsov, A. I. (2015). High-transmission dielectric metasurface with 2π phase control at visible wavelengths. *Laser & Photonics Reviews 9*, 412–418.

(*72*) Khorasaninejad, M., Aieta, F., Kanhaiya, P., Kats, M. A., Genevet, P., Rousso, D. and Capasso, F. (2015). Achromatic Metasurface Lens at Telecommunication Wavelengths. *Nano Letters 15*, 5358–5362.

(*73*) Yang, Y., Wang, W., Moitra, P., Kravchenko, I. I., Briggs, D. P. and Valentine, J. (2014). Dielectric Meta-Reflectarray for Broadband Linear Polarization Conversion and Optical Vortex Generation. *Nano Letters 14*, 1394–1399.

(*74*) Howes, A., Wang, W., Kravchenko, I. and Valentine, J. (2018). Dynamic transmission control based on all-dielectric Huygens metasurfaces. *Optica 5*, 787–792.

(*75*) Shalaev, M. I., Sun, J., Tsukernik, A., Pandey, A., Nikolskiy, K. and Litchinitser, N. M. (2015). High-Efficiency All-Dielectric Metasurfaces for Ultracompact Beam Manipulation in Transmission Mode. *Nano Letters 15*, 6261–6266.

(*76*) Chong, K. E., Staude, I., James, A., Dominguez, J., Liu, S., Campione, S., Subramania, G. S., Luk, T. S., Decker, M., Neshev, D. N., Brener, I. and Kivshar, Y. S. (2015). Polarization-Independent Silicon Metadevices for Efficient Optical Wavefront Control. *Nano Letters 15*, 5369–5374.

(*77*) Canfield, B. K., Kujala, S., Jefimovs, K., Turunen, J. and Kauranen, M. (2004). Linear and nonlinear optical responses influenced by broken symmetry in an array of gold nanoparticles. *Opt. Express 12*, 5418–5423.

(*78*) Huttunen, M. J., Reshef, O., Stolt, T., Dolgaleva, K., Boyd, R. W. and Kauranen, M. (2019). Efficient nonlinear metasurfaces by using multiresonant high-Q plasmonic arrays. *J. Opt. Soc. Am. B 36*, E30–E35.

(*79*) Klein, M. W., Enkrich, C., Wegener, M. and Linden, S. (2006). Second-Harmonic Generation from Magnetic Metamaterials. *Science 313*, 502–504.

(*80*) Valev, V. K., Smisdom, N., Silhanek, A. V., De Clercq, B., Gillijns, W., Ameloot, M., Moshchalkov, V. V. and Verbiest, T. (2009). Plasmonic Ratchet Wheels: Switching Circular Dichroism by Arranging Chiral Nanostructures. *Nano Letters 9*, 3945–3948.

(*81*) Czaplicki, R., Kiviniemi, A., Huttunen, M. J., Zang, X., Stolt, T., Vartiainen, I., Butet, J., Kuittinen, M., Martin, O. J. F. and Kauranen, M. (2018). Less Is More: Enhancement of Second-Harmonic Generation from Metasurfaces by Reduced Nanoparticle Density. *Nano Letters 18*, 7709–7714.

(*82*) Chen, S., Reineke, B., Li, G., Zentgraf, T. and Zhang, S. (2019). Strong Nonlinear Optical Activity Induced by Lattice Surface Modes on Plasmonic Metasurface. *Nano Letters 19*, 6278–6283.

(*83*) Keren-Zur, S., Avayu, O., Michaeli, L. and Ellenbogen, T. (2016). Nonlinear Beam Shaping with Plasmonic Metasurfaces. *ACS Photonics 3*, 117–123.

(*84*) Walter, F., Li, G., Meier, C., Zhang, S. and Zentgraf, T. (2017). Ultrathin Nonlinear Metasurface for Optical Image Encoding. *Nano Letters 17*, 3171–3175.

(*85*) Li, G., Chen, S., Pholchai, N., Reineke, B., Wong, P. W. H., Pun, E. Y. B., Cheah, K. W., Zentgraf, T. and Zhang, S. (2015). Continuous control of the nonlinearity phase for harmonic generations. *Nature Materials 14*, 607–612.

(*86*) Doron, O., Michaeli, L. and Ellenbogen, T. (2019). Direct and cascaded collective third-harmonic generation in metasurfaces. *J. Opt. Soc. Am. B 36*, E71–E77.

(*87*) Sartorello, G., Olivier, N., Zhang, J., Yue, W., Gosztola, D. J., Wiederrecht, G. P., Wurtz, G. and Zayats, A. V. (2016). Ultrafast Optical Modulation of Second- and Third-Harmonic Generation from Cut-Disk-Based Metasurfaces. *ACS Photonics 3*, 1517–1522.

(*88*) Yang, Y., Wang, W., Boulesbaa, A., Kravchenko, I. I., Briggs, D. P., Puretzky, A., Geohegan, D. and Valentine, J. (2015). Nonlinear Fano-Resonant Dielectric Metasurfaces. *Nano Letters 15*, 7388–7393.

(*89*) Tong, W., Gong, C., Liu, X., Yuan, S., Huang, Q., Xia, J. and Wang, Y. (2016). Enhanced third harmonic generation in a silicon metasurface using trapped mode. *Opt. Express 24*, 19661–19670.

(*90*) Deka, J., Jha, K. K., Menon, S., Krishna, A. S. L., Biswas, R. and Raghunathan, V. (2018). Microscopic study of resonant third-harmonic generation from amorphous silicon nanodisk arrays. *Opt. Lett. 43*, 5242–5245.

(*91*) Wang, L., Kruk, S., Koshelev, K., Kravchenko, I., Luther-Davies, B. and Kivshar, Y. (2018). Nonlinear Wavefront Control with All-Dielectric Metasurfaces. *Nano Letters 18*, 3978–3984.

(*92*) Reineke, B., Sain, B., Zhao, R., Carletti, L., Liu, B., Huang, L., De Angelis, C. and Zentgraf, T. (2019). Silicon Metasurfaces for Third Harmonic Geometric Phase Manipulation and Multiplexed Holography. *Nano Letters 19*, 6585–6591.

(*93*) Bar-David, J. and Levy, U. (2019). Nonlinear Diffraction in Asymmetric Dielectric Metasurfaces. *Nano Letters 19*, 1044–1051.

(*94*) Yuan, Q., Fang, L., Fang, H., Li, J., Wang, T., Jie, W., Zhao, J. and Gan, X. (2019). Second Harmonic and Sum-Frequency Generations from a Silicon Metasurface Integrated with a Two-Dimensional Material. *ACS Photonics 6*, 2252–2259.

(*95*) Welker, H. (1952). Über neue halbleitende Verbindungen. *Zeitschrift für Naturforschung A 7*, 744–749.

(*96*) Madelung, O., *Physics of III-V compounds*; J. Wiley: New York, 1964.

(*97*) Akinlami, J. O. and Ashamu, A. O. (2013). Optical properties of GaAs. *Journal of Semiconductors 34*, 032002.

(*98*) Aspnes, D. E., Kelso, S. M., Logan, R. A. and Bhat, R. (1986). Optical properties of $Al_xGa_{1-x}As$. *Journal of Applied Physics 60*, 754–767.

(*99*) Deri, R. J. and Emanuel, M. A. (1995). Consistent formula for the refractive index of $Al_xGa_{1-x}As$ below the band edge. *Journal of Applied Physics 77*, 4667–4672.

(*100*) Blakemore, J. S. (1982). Semiconducting and other major properties of gallium arsenide. *Journal of Applied Physics 53*, R123–R181.

(*101*) Schlereth, K.-H. (1996). III–V semiconductor lasers: application in telecommunication systems - suitability for spectroscopy. *Infrared Physics & Technology 37*, 129–142.

(*102*) Yin, Z. and Tang, X. (2007). A review of energy bandgap engineering in III–V semiconductor alloys for mid-infrared laser applications. *Solid-State Electronics 51*, 6–15.

(*103*) Boyd, R., *Nonlinear Optics*, Third Edition; Boyd, R. W., Ed.; Academic Press: Burlington, 2008.

(*104*) Xu, L., Rahmani, M., Smirnova, D., Zangeneh Kamali, K., Zhang, G., Neshev, D. and Miroshnichenko, A. E. (2020). Forward and Backward Switching of Nonlinear Zero-Order Emission from GaAs Nanoantennas. *ACS Nano 14*, 1379–1389.

(*105*) Sautter, J. D. et al. (2019). Tailoring Second-Harmonic Emission from (111)-GaAs Nanoantennas. *Nano Letters 19*, 3905–3911.

(*106*) Carletti, L., Locatelli, A., Stepanenko, O., Leo, G. and Angelis, C. D. (2015). Enhanced second-harmonic generation from magnetic resonance in AlGaAs nanoantennas. *Opt. Express 23*, 26544–26550.

(*107*) Carletti, L., Locatelli, A., Neshev, D. and De Angelis, C. (2016). Shaping the Radiation Pattern of Second-Harmonic Generation from AlGaAs Dielectric Nanoantennas. *ACS Photonics 3*, 1500–1507.

(*108*) Gili, V. F., Carletti, L., Locatelli, A., Rocco, D., Finazzi, M., Ghirardini, L., Favero, I., Gomez, C., Lemaître, A., Celebrano, M., Angelis, C. D. and Leo, G. (2016). Monolithic AlGaAs second-harmonic nanoantennas. *Opt. Express 24*, 15965–15971.

(*109*) Ghirardini, L., Carletti, L., Gili, V., Pellegrini, G., Duò, L., Finazzi, M., Rocco, D., Locatelli, A., Angelis, C. D., Favero, I., Ravaro, M., Leo, G., Lemaître, A. and Celebrano, M. (2017). Polarization properties of second-harmonic generation in AlGaAs optical nanoantennas. *Opt. Lett. 42*, 559–562.

(*110*) Liu, S., Sinclair, M. B., Saravi, S., Keeler, G. A., Yang, Y., Reno, J., Peake, G. M., Setzpfandt, F., Staude, I., Pertsch, T. and Brener, I. (2016). Resonantly enhanced second-harmonic generation using III-V semiconductor all-dielectric metasurfaces. *Nano Letters*, 5426–5432.

(*111*) Löchner, F. J. F., Fedotova, A. N., Liu, S., Keeler, G. A., Peake, G. M., Saravi, S., Shcherbakov, M. R., Burger, S., Fedyanin, A. A., Brener, I., Pertsch, T., Setzpfandt, F. and Staude, I. (2018). Polarization-Dependent Second Harmonic Diffraction from Resonant GaAs Metasurfaces. *ACS Photonics 5*, 1786–1793.

(*112*) Marino, G., Gigli, C., Rocco, D., Lemaître, A., Favero, I., De Angelis, C. and Leo, G. (2019). Zero-Order Second Harmonic Generation from AlGaAs-on-Insulator Metasurfaces. *ACS Photonics 6*, 1226–1231.

(*113*) Vabishchevich, P. P., Liu, S., Sinclair, M. B., Keeler, G. A., Peake, G. M. and Brener, I. (2018). Enhanced Second-Harmonic Generation Using Broken Symmetry III–V Semiconductor Fano Metasurfaces. *ACS Photonics 5*, 1685–1690.

(*114*) Liu, S., Vabishchevich, P. P., Vaskin, A., Reno, J. L., Keeler, G. A., Sinclair, M. B., Staude, I. and Brener, I. (2018). An all-dielectric metasurface as a broadband optical frequency mixer. *Nature Communications 9*, 1–6.

(*115*) Hu, H., Wang, K., Long, H., Liu, W., Wang, B. and Lu, P. (2015). Precise Determination of the Crystallographic Orientations in Single ZnS Nanowires by Second-Harmonic Generation Microscopy. *Nano Letters 15*, 3351–3357.

(*116*) Pimenta, A. C. S., Teles Ferreira, D. C., Roa, D. B., Moreira, M. V. B., de Oliveira, A. G., González, J. C., De Giorgi, M., Sanvitto, D. and Matinaga, F. M. (2016). Linear and Nonlinear Optical Properties of Single GaAs Nanowires with Polytypism. *The Journal of Physical Chemistry C 120*, 17046–17051.

(*117*) Timofeeva, M., Bouravleuv, A., Cirlin, G., Shtrom, I., Soshnikov, I., Reig Escalé, M., Sergeyev, A. and Grange, R. (2016). Polar Second-Harmonic Imaging to Resolve Pure and Mixed Crystal Phases along GaAs Nanowires. *Nano Letters 16*, 6290–6297.

(*118*) Ren, M.-L., Agarwal, R., Liu, W. and Agarwal, R. (2015). Crystallographic Characterization of II–VI Semiconducting Nanostructures via Optical Second Harmonic Generation. *Nano Letters 15*, 7341–7346.

(*119*) Wei, Y.-M., Yu, Y., Wang, J., Liu, L., Ni, H.-Q., Niu, Z.-C., Li, J.-T., Wang, X.-H. and Yu, S.-Y. (2017). Structural discontinuity induced surface second harmonic generation in single, thin zinc-blende GaAs nanowires. *Nanoscale 9*, 16066–16072.

(*120*) Woźniak, P., Banzer, P. and Leuchs, G. (2015). Selective switching of individual multipole resonances in single dielectric nanoparticles. *Laser & Photonics Reviews 9*, 231–240.

(*121*) Neugebauer, M., Woźniak, P., Bag, A., Leuchs, G. and Banzer, P. (2016). Polarization-controlled directional scattering for nanoscopic position sensing. *Nature Communications 7*, 1–6.

(*122*) Bautista, G., Mäkitalo, J., Chen, Y., Dhaka, V., Grasso, M., Karvonen, L., Jiang, H., Huttunen, M. J., Huhtio, T., Lipsanen, H. and Kauranen, M. (2015). Second-Harmonic Generation Imaging of Semiconductor Nanowires with Focused Vector Beams. *Nano Letters 15*, 1564–1569.

(*123*) Camacho-Morales, R., Bautista, G., Zang, X., Xu, L., Turquet, L., Miroshnichenko, A., Tan, H. H., Lamprianidis, A., Rahmani, M., Jagadish, C., Neshev, D. N. and Kauranen, M. (2019). Resonant harmonic generation in AlGaAs nanoantennas probed by cylindrical vector beams. *Nanoscale 11*, 1745–1753.

(*124*) Harrington, R. F. (1967). Matrix methods for field problems. *Proceedings of the IEEE 55*, 136–149.

(*125*) Jin, J.-M., *Theory and Computation of Electromagnetic Fields*, Second Edition; Sons, J. W., Ed., New Jersey, 2015.

(*126*) Mäkitalo, J., Suuriniemi, S. and Kauranen, M. (2011). Boundary element method for surface nonlinear optics of nanoparticles. *Opt. Express 19*, 23386–23399.

(*127*) Novotny, L. and Hecht, B., *Principles of Nano-Optics*; Cambridge University Press: 2006.

(*128*) Long, J. P., Simpkins, B. S., Rowenhorst, D. J. and Pehrsson, P. E. (2007). Far-field Imaging of Optical Second-Harmonic Generation in Single GaN Nanowires. *Nano Letters 7*, 831–836.

(*129*) Bautista, G., Pfisterer, S. G., Huttunen, M. J., Ranjan, S., Kanerva, K., Ikonen, E. and Kauranen, M. (2014). Polarized THG Microscopy Identifies Compositionally Different Lipid Droplets in Mammalian Cells. *Biophysical Journal 107*, 2230–2236.

(*130*) Morizet, J., Ducourthial, G., Supatto, W., Boutillon, A., Legouis, R., Schanne-Klein, M.-C., Stringari, C. and Beaurepaire, E. (2019). High-speed polarization-resolved third-harmonic microscopy. *Optica 6*, 385–388.

(*131*) Jordan, R. H. and Hall, D. G. (1994). Free-space azimuthal paraxial wave equation: the azimuthal Bessel–Gauss beam solution. *Opt. Lett. 19*, 427–429.

(*132*) Youngworth, K. S. and Brown, T. G. In *Three-Dimensional and Multidimensional Microscopy: Image Acquisition Processing VII*, 2000; Vol. 3919, pp 75–86.

(*133*) Youngworth, K. S. and Brown, T. G. (2000). Focusing of high numerical aperture cylindrical-vector beams. *Opt. Express 7*, 77–87.

(*134*) Savinov, V., Fedotov, V. A. and Zheludev, N. I. (2014). Toroidal dipolar excitation and macroscopic electromagnetic properties of metamaterials. *Physical Review B 89*, 205112.

(*135*) Luk'yanchuk, B., Paniagua-Domınguez, R., Kuznetsov, A. I., Miroshnichenko, A. E. and Kivshar, Y. S. (2017). Hybrid anapole modes of high-index dielectric nanoparticles. *Physical Review A 95*, 063820.

(*136*) Evlyukhin, A. B., Fischer, T., Reinhardt, C. and Chichkov, B. N. (2016). Optical theorem and multipole scattering of light by arbitrarily shaped nanoparticles. *Physical Review B 94*, 205434.

(*137*) Paniagua-Domınguez, R., Yu, Y. F., Miroshnichenko, A. E., Krivitsky, L. A., Fu, Y. H., Valuckas, V., Gonzaga, L., Toh, Y. T., Kay, A. Y. S., Luk'yanchuk, B. et al. (2016). Generalized Brewster effect in dielectric metasurfaces. *Nature Communications 7*, 10362.

(*138*) Fernandez-Corbaton, I., Nanz, S., Alaee, R. and Rockstuhl, C. (2015). Exact dipolar moments of a localized electric current distribution. *Opt. Express 23*, 33044–33064.

(*139*) Shibanuma, T., Grinblat, G., Albella, P. and Maier, S. A. (2017). Efficient third harmonic generation from metal-dielectric hybrid nanoantennas. *Nano Letters 17*, 2647–2651.

(*140*) Timofeeva, M., Lang, L., Timpu, F., Renaut, C., Bouravleuv, A., Shtrom, I., Cirlin, G. and Grange, R. (2018). Anapoles in Free-Standing III–V Nanodisks Enhancing Second-Harmonic Generation. *Nano Letters 18*, 3695–3702.

(*141*) Rocco, D., Gili, V. F., Ghirardini, L., Carletti, L., Favero, I., Locatelli, A., Marino, G., Neshev, D. N., Celebrano, M., Finazzi, M., Leo, G. and Angelis, C. D. (2018). Tuning the second-harmonic generation in AlGaAs nanodimers via non-radiative state optimization. *Photonics Research 6*, B6–B12.

(*142*) Xu, L., Rahmani, M., Zangeneh Kamali, K., Lamprianidis, A., Ghirardini, L., Sautter, J., Camacho-Morales, R., Chen, H., Parry, M., Staude, I., Zhang, G., Neshev, D. and Miroshnichenko, A. E. (2018). Boosting third-harmonic generation by a mirror-enhanced anapole resonator. *Light: Science & Applications 7*, 1–8.

(*143*) Lamprianidis, A. G. and Miroshnichenko, A. E. (2018). Excitation of nonradiating magnetic anapole states with azimuthally polarized vector beams. *Beilstein Journal of Nanotechnology 9*, 1478–1490.

(*144*) Camacho-Morales, R. et al. (2016). Nonlinear Generation of Vector Beams From AlGaAs Nanoantennas. *Nano Letters 16*, 7191–7197.

(*145*) Kruk, S. S., Camacho-Morales, R., Xu, L., Rahmani, M., Smirnova, D. A., Wang, L., Tan, H. H., Jagadish, C., Neshev, D. N. and Kivshar, Y. S. (2017). Nonlinear Optical Magnetism Revealed by Second-Harmonic Generation in Nanoantennas. *Nano Letters 17*, 3914–3918.

(*146*) Hugonin, J. P. and Lalanne, P., Reticolo software for grating analysis, Institut d'Optique, Orsay, France, 2005.

(*147*) Kerker, M., Wang, D.-S. and Giles, C. L. (1983). Electromagnetic scattering by magnetic spheres. *J. Opt. Soc. Am. 73*, 765–767.

(*148*) Grahn, P., Shevchenko, A. and Kaivola, M. (2012). Electromagnetic multipole theory for optical nanomaterials. *New Journal of Physics 14*, 093033.

(*149*) Ghirardini, L., Marino, G., Gili, V. F., Favero, I., Rocco, D., Carletti, L., Locatelli, A., De Angelis, C., Finazzi, M., Celebrano, M., Neshev, D. N. and Leo, G. (2018). Shaping the Nonlinear Emission Pattern of a Dielectric Nanoantenna by Integrated Holographic Gratings. *Nano Letters 18*, 6750–6755.

(*150*) Carletti, L., Marino, G., Ghirardini, L., Gili, V. F., Rocco, D., Favero, I., Locatelli, A., Zayats, A. V., Celebrano, M., Finazzi, M., Leo, G., De Angelis, C. and Neshev, D. N. (2018). Nonlinear Goniometry by Second-Harmonic Generation in AlGaAs Nanoantennas. *ACS Photonics 5*, 4386–4392.

(*151*) Xu, L., Rahmani, M., Smirnova, D., Zangeneh Kamali, K., Zhang, G., Neshev, D. and Miroshnichenko, A. E. (2018). Highly-Efficient Longitudinal Second-Harmonic Generation from Doubly-Resonant AlGaAs Nanoantennas. *Photonics 5*, 29.

(*152*) Sautter, J., Staude, I., Decker, M., Rusak, E., Neshev, D. N., Brener, I. and Kivshar, Y. S. (2015). Active Tuning of All-Dielectric Metasurfaces. *ACS Nano 9*, 4308–4315.

(*153*) Woolf, D. A., Sobiesierski, Z., Westwood, D. I. and Williams, R. H. (1992). The molecular beam epitaxial growth of GaAs/GaAs(111)B: doping and growth temperature studies. *Journal of Applied Physics 71*, 4908–4915.

(*154*) Reep, D. and Ghandhi, S. (1983). Morphology of organometallic CVD grown GaAs epitaxial layers. *Journal of Crystal Growth 61*, 449–457.

(*155*) Fuek, S., Umemura, M., Yamada, N., Kuwahara, K. and Imai, T. (1990). Morphology of GaAs homoepitaxial layer grown on (111) A substrate planes by organometallic vapor phase deposition. *Journal of Applied Physics 68*, 97–100.

(*156*) Algorri, J. F., Zografopoulos, D. C., Ferraro, A., García-Cámara, B., Vergaz, R., Beccherelli, R. and Sánchez-Pena, J. M. (2018). Anapole Modes in Hollow Nanocuboid Dielectric Metasurfaces for Refractometric Sensing. *Nanomaterials 9*, 30.

(*157*) Koshelev, K., Kruk, S., Melik-Gaykazyan, E., Choi, J.-H., Bogdanov, A., Park, H.-G. and Kivshar, Y. (2020). Subwavelength dielectric resonators for nonlinear nanophotonics. *Science 367*, 288–292.

(*158*) Blechman, Y., Almeida, E., Sain, B. and Prior, Y. (2019). Optimizing the Nonlinear Optical Response of Plasmonic Metasurfaces. *Nano Letters 19*, 261–268.

(*159*) Liu, S., Vaskin, A., Campione, S., Wolf, O., Sinclair, M. B., Reno, J., Keeler, G. A., Staude, I. and Brener, I. (2017). Huygens' Metasurfaces Enabled by Magnetic Dipole Resonance Tuning in Split Dielectric Nanoresonators. *Nano Letters 17*, 4297–4303.

(*160*) Shcherbakov, M. R., Liu, S., Zubyuk, V. V., Vaskin, A., Vabishchevich, P. P., Keeler, G., Pertsch, T., Dolgova, T. V., Staude, I., Brener, I. and Fedyanin, A. A. (2017). Ultrafast all-optical tuning of direct-gap semiconductor metasurfaces. *Nature Communications 8*, 1–6.

(*161*) Ha, S. T., Fu, Y. H., Emani, N. K., Pan, Z., Bakker, R. M., Paniagua-Domínguez, R. and Kuznetsov, A. I. (2018). Directional lasing in resonant semiconductor nanoantenna arrays. *Nature Nanotechnology 13*, 1042–1047.

(*162*) Saleh, B. E. A. and Carl Teich, M. In *Fundamentals of Photonics*; John Wiley Sons, Ltd: 2001; Chapter 4, pp 108–156.

APPENDIX A

A1 Focal fields.

Typically, the back-aperture of a microscope objective is a couple of millimeters in diameter. In order to make use of the full NA of the objective lens, the incident field $\boldsymbol{E}_{inc}$ has to fill or overfill the back-aperture. Thus, because of the large diameter of the incident beam it is reasonable to treat it in the paraxial approximation. Under this approximation and considering that the objective lens have a good antireflection coating, so we can neglect the Fresnel transmission coefficients, the *apodization function* and several integrals are defined to express the focal fields of the radially and azimuthally polarised beams in a contracted manner.

The *apodization function* can be viewed as a pupil filter and it is expressed as:

$$f_w(\theta) = e^{\frac{1}{f_0^2}\frac{sin^2\theta}{sin^2\theta_{max}}}. \tag{A.1}$$

While the integrals are defined as:

$$I_{10} = \int_0^{\theta_{max}} f_w(cos\theta)^{1/2} sin^3\theta J_0(k\rho sin\theta) e^{ikzcos\theta} d\theta \tag{A.2}$$

$$I_{11} = \int_0^{\theta_{max}} f_w(cos\theta)^{1/2} sin^2\theta(1+3cos\theta) J_1(k\rho sin\theta) e^{ikzcos\theta} d\theta \tag{A.3}$$

$$I_{12} = \int_0^{\theta_{max}} f_w(cos\theta)^{1/2} sin^2\theta(1-cos\theta) J_1(k\rho sin\theta) e^{ikzcos\theta} d\theta \tag{A.4}$$

Notice, that these integrals are functions of the coordinates (ρ,z), *i.e.* I_{ij}=I_{ij}(ρ,z). Thus, for each field point we have to numerically evaluate these integrals (*127*).

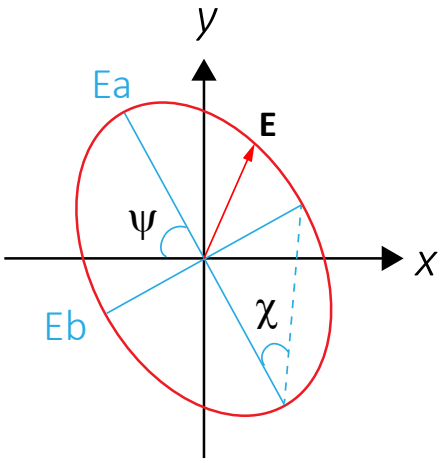

FIGURE A.1: Illustration of the polarisation ellipse with its polarisation parameters: ellipticity angle χ and polarisation-inclination angle ψ. E_a and E_b are the main polarisation ellipse axes (solid blue lines), x and y define the laboratory coordinate system and $\boldsymbol{E}$ is the oscillating electric field vector of the optical signal.

A2 Stokes Polarimetry

The Stokes parameters provide a full description of the polarisation state of an optical signal in terms of its total intensity I_{tot}, degree of polarisation ρ, polarisation inclination angle ψ, and ellipticity angle χ. The polarisation inclination angle ψ and the ellipticity angle χ are visualised in the polarisation ellipse, illustrated in Figure A.1. The shape of the polarisation ellipse is governed by the magnitude of the horizontal and vertical components of the electric field vector $\boldsymbol{E}$ and the relative phase between them. The polarisation inclination angle ψ is the angle between the main polarisation axis E_a and the x-axis of the laboratory coordinate system, while $tan(\chi)$ is defined as the ratio between the two axes of the polarisation ellipse, E_a and E_b.

Experimentally, the Stokes parameters can be obtained by measuring the optical signal being transmitted through polarisation-sensitive optical devices. These optical devices, usually a quarter wave plate and a linear polariser, separate the optical signal in its different polarisation components: right-hand (R) and left-hand (L) circular polarisations, horizontal (H) and vertical (V) linear polarisations, and two diagonal (D_a and D_b) linear polarisations, that are orthogonal to each other. The six polarisation states provide the components of the Stokes

vector *S*, defined as:

$$S = \begin{bmatrix} I \\ Q \\ U \\ V \end{bmatrix}, \tag{A.5}$$

where

$$\begin{aligned} I = H + V = D_a + D_b = L + R, \\ Q = H - V, \\ U = D_a - D_b, \\ V = L - R. \end{aligned} \tag{A.6}$$

I refers to the total intensity, Q is the difference in intensity between light with linear polarisation in the direction ψ= 0° and light with linear polarisation in the direction ψ= 90°. U has an analogous interpretation with the difference in intensity for linearly polarised light with ψ =45,° compared to that for ψ= 135°. V is the difference in intensity of light with right-handed circular polarisation, over the light with left-handed circular polarisation.

The polarisation degree ρ, polarisation inclination angle ψ, and ellipticity angle χ of the optical signal can be calculated through the components of the Stokes vector, according to:

$$\begin{aligned} \rho = \frac{\sqrt{Q^2 + U^2 + V^2}}{I}, \\ \psi = \frac{1}{2} arctan\big(Q + iU\big), \\ \chi = \frac{1}{2} arctan\left(\frac{V}{\sqrt{U^2 + V^2}}\right). \end{aligned} \tag{A.7}$$

A3 Fourier imaging

Fourier imaging or back focal plane (BFP) imaging is based on the ability of a lens to create a Fourier transform of the incident field at the BFP of the lens. This property allows us to measure the far-field emission or radiation pattern of scattering particles. The angular

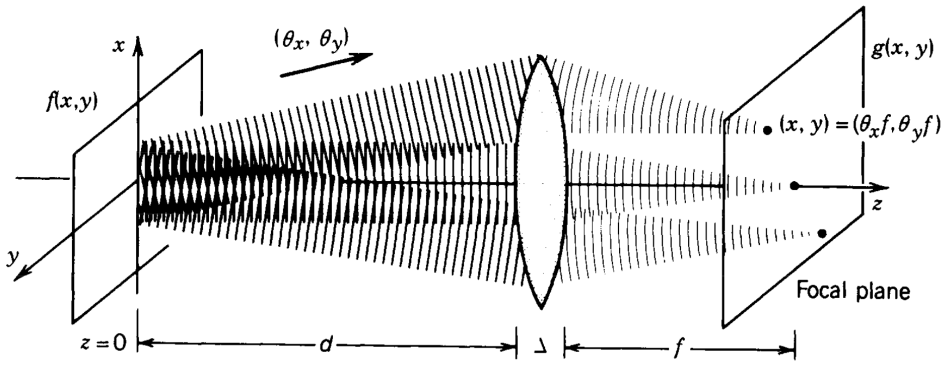

FIGURE A.2: Focusing of the plane waves associated with the harmonic Fourier components of the input function *f (x,y)* into points in the focal plane. The amplitude of the plane wave with direction (θ_x, θ_y)=$(\lambda\nu_x, \lambda\nu_y)$ is proportional to the Fourier transform $F(\nu_x, \nu_y)$ and it is focused in the point *(x,y)*=$(\theta_x f, \theta_y f)$=$(\lambda f\nu_x, \lambda f\nu_y)$ (*162*).

radiation pattern is an important characteristic of a resonant particle, since specific resonant modes are often characterised by distinct radiation patterns.

A thin spherical lens transforms a plane wave into a paraboloidal wave, and focuses it to a point at the lens BFP. This is a general property of a lens: when a plane wave arrives at small angles θ_x=λ/ν_x, and θ_y=λ/ν_y, the resulting paraboloidal wave is focused at the BFP of the lens to a point $(\theta_x f, \theta_y f)$, where f is the focal length of the lens. In this way, every plane wave component of an optical field travelling at an angle (θ_x, θ_y) will be mapped to a single point $(\theta_x f, \theta_y f)$, after being transmitted through a lens. In other words, considering *f (x,y)* as the complex amplitude of an incident optical field in the *z=0* plane, every component of the incident field is focused by the lens to a point *(x, y)*, where *x*=$\theta_x f$=λ/ν_x and *y*=$\theta_y f$=λ/ν_y, as illustrated in Figure A.2. At the output (back) focal plane, the complex amplitude of *f (x,y)* is proportional to its Fourier transform $F(\nu_x, \nu_y)$, evaluated at ν_x=*x*/λf and ν_y=*y*/λf, such that (*162*):

$$g(x, y) \propto \left(\frac{x}{\lambda f}, \frac{y}{\lambda f}\right). \tag{A.8}$$

Thus, the field distribution at the BFP of the lens is proportional to the 2D Fourier transform of the incident field, corresponding to the Fraunhofer diffraction pattern or far-field radiation pattern. Traditionally, the BFP imaging technique employs an objective lens with a high NA

to collect the emission of the scattering object and increase the information obtained from the k-space. The NA of the objective lens is given by $NA=nsin\theta$, n being the refractive index of the surrounding medium and θ being the maximum half-angle of the light cone collected by the objective lens. Therefore, the use of high NA objective lenses is desirable since it allows to increase the collection angle of the light and consequently the information retrieved from the k-space.